One-Dimensionality on Thermoelectric Properties of Carbon Nanotubes

カーボンナノチューブの熱電物性における一次元性

Yota Ichinose

一ノ瀬 遥太

Department of Physics, Graduate School of Science,
Tokyo Metropolitan University

2022

CONTENTS

Chapter 1

Introduction

1.1 Overview and background

Demands for thermoelectrics in our society

Currently, a massive amount of fossil fuels are consumed worldwide. A society dependent on fossil fuels will cause environmental problems, including global warming, and will threaten the realization of a sustainable society. Thus, we are responsible for shifting to various alternative energy resources. One option is to use waste heat. For example, the conversion efficiency of fossil fuels is only about 30-40% at best [1,2], throwing away the non-used energy as waste heat. Therefore, we are required to utilize a large amount of the excess waste heat as a new energy source.

Thermoelectric conversion, which can convert heat into electricity, was first reported by T. J. Seebeck in 1822 [3]. When a temperature difference is applied to both ends of an electric conductor, generating a potential difference proportional to the temperature difference, we can extract electric power externally [see **Figure 1.1**]. The advantages of thermoelectric conversion are manifold. Since heat can be directly converted into electricity, there is no CO_2 emission and no mechanical moving parts. Furthermore, thermoelectric devices have the advantage of generating power on a small scale because of no scale effects. Therefore, we expect thermoelectric devices that are clean, quiet, maintenance-free, and scalable. Most waste heat is relatively low-temperature heat, less than 200°C, and from any location. Therefore, the strategy of laying out a large number of small-scale thermoelectric conversion devices will be possible to recover a large amount of heat, i.e., energy harvesting technologies.

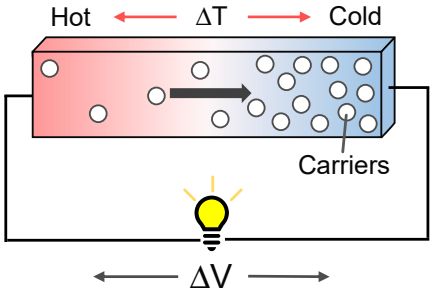

Figure 1.1. Schematic diagram of the Seebeck effect. The details are given in Section 2.1.

In addition to the above properties, flexible and lightweight materials will expand the options of usable environments, leading to an explosion of applications [4,5]. For example, by forming thermoelectric devices to fit the curved surface of the human body, self-powered wearable devices can be driven by body heat [6]. Furthermore, we expect to enter an era of one trillion sensors shortly with the promotion of the IoT society [7]. Conventional chemical batteries need to be replaced with a life cycle, but it is not realistic to replace the huge number of batteries. Thermoelectric devices installed in any environment could be one strategy since they do not require battery replacement. Therefore, thermoelectric conversion can solve energy problems and contribute significantly to the advancement of technology.

Conventional guidelines for the design of thermoelectric materials

The initial mainstream of thermoelectric material developments was in inorganic bulk materials. **Figure 1.2** summarizes the maximum value of the dimensionless figure of merit $ZT = (S^2\sigma T)/\kappa$ and the reported year, where S is the Seebeck coefficient, σ is the electrical conductivity, κ is the thermal conductivity, and T is the absolute temperature. First, let us look at the left area of the figure, which is in the early days of thermoelectrics. Research to explore materials with high thermoelectric conversion efficiency has been vigorously conducted for more than 50 years. For example, the discovery of Bi_2Te_3-based thermoelectric materials by Goldsmid in the 1950s triggered a flurry of research on thermoelectric conversion [8,9]. Similar inorganic bulk semiconductors such as PbTe [10] and SiGe [11-13] were reported, and their performance was optimized $ZT \sim 1$ around the 1970s.

The thermoelectric performance seemed to improve by the 1970s; however, these conventional inorganic thermoelectric materials faced the limit of conversion efficiency. As shown in **Figure 1.2**, no significant improvement in conversion performance was reported for some decades after 1970 due to the trade-off relationship between thermoelectric parameters [14]. For example, to improve ZT, the strategy is to reduce the denominator κ or increase the numerator $P \equiv S^2\sigma$, called the power factor. However, these physical properties are closely related to each other, and there is a trade-off relationship. When the carrier density increases, we expect the increase of σ and κ, while

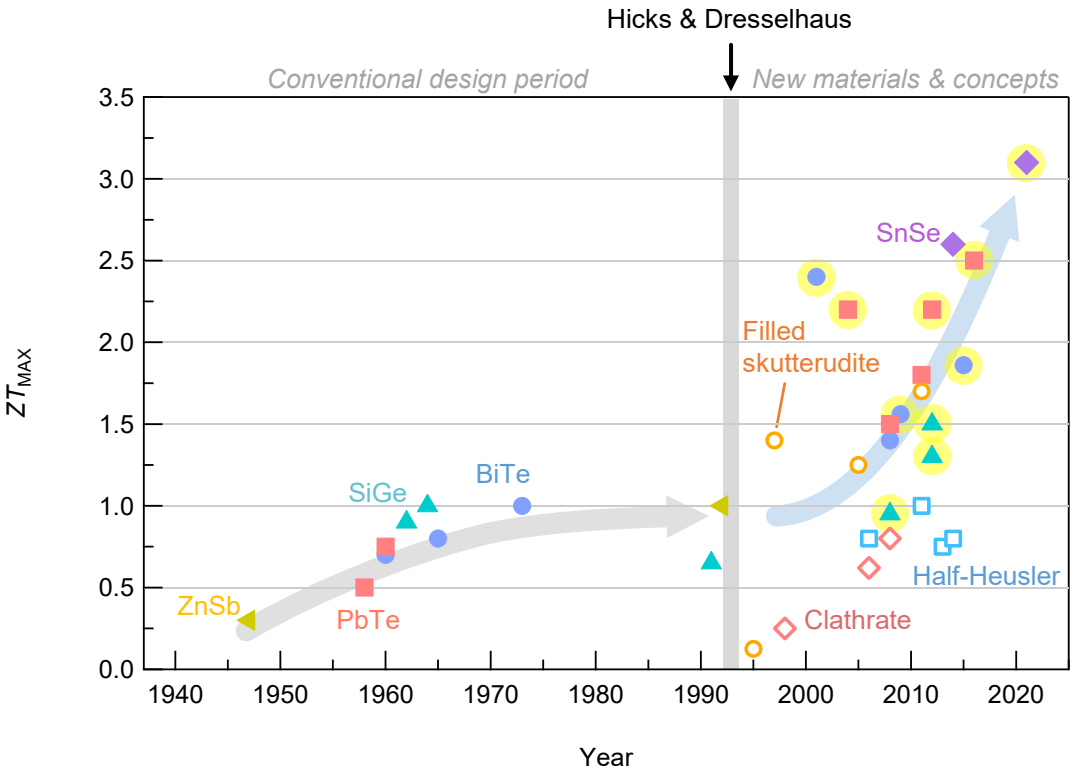

Figure 1.2. The transition of thermoelectric conversion performance over year. The straight gray line indicates the year when the low-dimensional strategy was proposed by Hicks & Dresselhaus. Before the proposal, thermoelectric materials were mainly studied in inorganics. After the proposal, many new materials were reported. The points highlighted in the light-yellow circles are data for materials that utilize nanostructures.

the decrease of S [15]. A series of studies revealed the approximate optimum carrier density, meaning the limit of performance improvement. Hence, thermoelectric research had been converging by establishing this design guideline. We required a new concept to break the trade-off problem to develop thermoelectric materials.

In addition, the inorganic materials above have not solved the safety and cost issues [2,16]. Inorganic thermoelectric materials include toxic lead and tellurium as constituent elements, which raises safety concerns. Moreover, the fabrication cost is high due to the use of minor metals; thus, the cost performance is poor. For these reasons, thermoelectrics has not been widely used in society due to its limited applications, despite the potential promise. Therefore, safety and low cost are also essential factors in developing thermoelectric materials [17].

New phase for developing thermoelectric materials

In 1993, Hicks and Dresselhaus theoretically provided an innovative guideline for developing thermoelectric materials [18,19]. They proposed that introducing nanostructures into thermoelectric materials could dramatically enhance the performance by overcoming the traditional trade-offs. Following this series of proposals, research in the thermoelectric field was resurgent and entered a new era after the 1990s. Let us look at the right side of **Figure 1.2**, i.e., after the proposal by Hicks & Dresselhaus. In fact, ZT began to improve again by processing inorganic materials such as Bi_2Te_3 [20-23], PbTe [24-27], and SiGe [28-30] into superlattice structures and nanowires [31-33]. Moreover, not limited to nanostructures, many new concepts (band engineering [27,34-36], phonon glasses [37], energy filters [38], etc.) and new thermoelectric materials (filled skutterudites [39-42], clathrate compounds [43-45], half-heusler [46-49], oxide materials [50,51], etc. [52,53]) have been proposed, and ZT has improved significantly [54]. For most of these materials, the approaches focus on reducing κ while maintaining P as high as possible.

Advantages of low-dimensional materials

The unique feature of low-dimensional materials with nanostructures is that the P value can be significantly increased [18,19]. Dresselhaus et al. originally showed that the following two factors could improve thermoelectric performance by lowering the dimensionality of materials; reduction of κ and enhancement of P. The reduction in κ is attributed to the interfacial scattering of phonons. The improvement of ZT in Bi_2Te_3 nanowires and other nanostructured materials mentioned above is mainly due to the effect of κ [28,31,33]. However, research to improve ZT by reducing κ had been conducted before their proposals [55,56]; thus, the approach was not a special case for nanomaterials. On the other hand, few approaches can enhance P. Therefore, the lowering dimensionality was a unique milestone proposal, which provides the reduction of κ and the enhancement of P simultaneously. Note that increasing P not only leads to higher ZT but also higher output power density. For example, when an unlimited supply of thermal energy is available, such as factory waste heat, P rather than ZT may be a more

meaningful indicator [57-59]. Therefore, increasing the value of P is as essential as increasing ZT.

According to their theory, the increase in P is due to the quantum confinement effect in low-dimensional materials. Low-dimensional materials have electronic structures with an abrupt change in the density of states (DOS) as a function of energy dependence, unlike the typical 3D bulk materials [see **Figure 1.3**]. P is expected to increase dramatically when the chemical potential is near the abrupt change [19]. Recent studies reported the significant enhancement in P due to quantum confinement effects on 2D materials such as SrTiO3 superlattices [60,61], FeSe superconductor [62], and graphene [63,64]. These results verified that lowering the dimensionality of materials is promising for improving P.

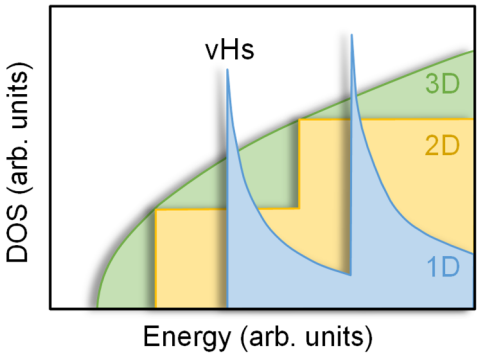

Figure 1.3. Conceptual diagram of the density of states. Low-dimensional (2D & 1D) materials have a steep DOS change.

As an extension of this line of discussions, we expect the ultimate thermoelectric material to be one-dimensional (1D) materials [19]. In their electronic structure, 1D materials have a divergent peak structure in DOS, called van Hove singularity (vHs), see **Figure 1.3** [65]. Here, this unique electronic structure of 1D materials is referred to as the 1D electronic structure. The DOS changes most rapidly in 1D systems, thus, the highest thermoelectric performance was predicted [19]. Mahan and Sofo also supported this idea [66]. Later, some research tried a top-down approach to making materials a 1D system [67-69]; however, no report showed that the 1D electronic structure clearly enhances P. Experimental verification on the relationship between 1D electronic structures and the thermoelectric properties has not been performed yet due to the difficulty in handling truly 1D metallic materials and their low practicality as thermoelectric devices. In order to realize the innovative proposal by Dresselhaus to maximize thermoelectric performance by 1D electronic structures, we had to wait for the emergence of an ideal 1D material system with a diameter of ~1 nm.

Single-walled carbon nanotubes

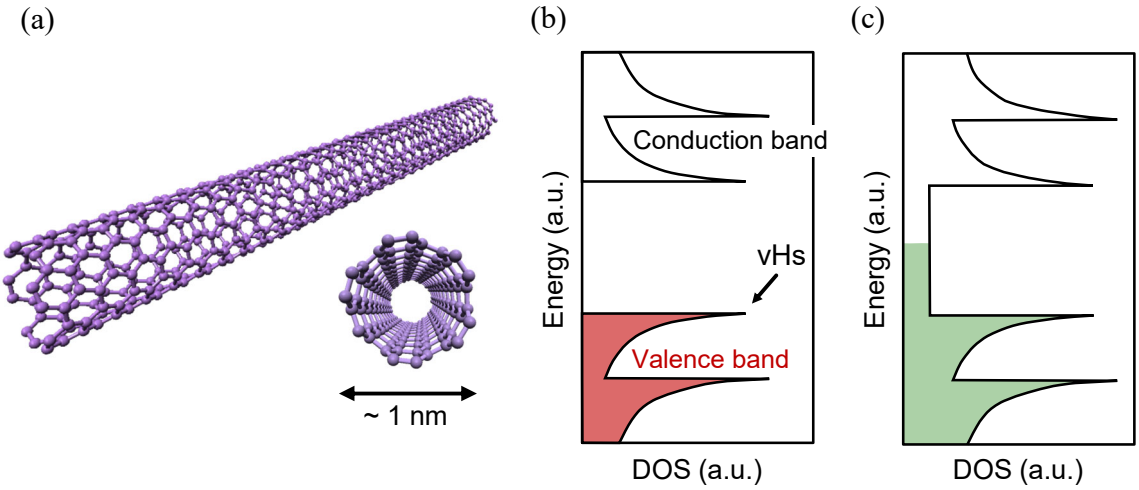

Figure 1.4. Single-walled carbon nanotubes (SWCNTs). (a) Graphic image of SWCNTs. Electronic structure of (b) semiconducting SWCNTs and (c) metallic SWCNTs. The density of states have sharp divergence points, van Hove singularity (vHs).

In 1993, slightly before Dresselhaus published the theoretical papers, Iijima experimentally discovered single-walled carbon nanotubes (SWCNTs) [70]. It is noteworthy that Iijima's paper significantly influenced the motivation of Dresslhaus's theoretical paper. The new material has a 1D structure with an extremely high aspect ratio, consisting of graphene sheets rolled into a cylinder with a diameter of about 1 nm; see **Figure 1.4** [71,72]. SWCNTs have sharp vHs in their electronic structure, reflecting their 1D nature. In addition, the existence of a wide variety of structural isomers is the characteristic property [73,74]. The structural isomers, called "chirality," are distinguished by the chiral index (*n,m*), which determines how the graphene sheet is rolled. Every chirality has a different electronic structure, such as wide- or narrow-bandgap semiconducting types and metallic types. Another notable property of SWCNTs is their stability. Due to their closed-shell structure without dangling bonds, SWCNTs are physically and chemically very stable despite being nanoscale materials. Therefore, SWCNTs are an ideal and unique material to investigate the relationship between the 1D electronic structure and thermoelectric properties.

We should mention that SWCNTs are highly suitable thermoelectric materials also for applications. The constituent elements are only carbon, and minor metals are entirely free. Thus, safety and resource scarcity concerns are minimal. SWCNTs are lightweight yet have incredibly high mechanical durability, making them adaptable to various environments. Moreover, SWCNTs can be fabricated into various shapes, such as thin films and fibers. Used in flexible forms, SWCNTs can be envisioned for use in wearable devices for the human body and curved surfaces of factory pipes. Thus, SWCNTs possess all the requirements mentioned in the previous paragraphs. The experimental investigation of whether SWCNTs significantly improve P by the 1D electronic structure has not only scientific value but also the value of extending the possibilities for applications.

Thermoelectric research on SWCNTs

SWCNTs, an attractive thermoelectric material, quickly became the scope of thermoelectric research in the 1990s. In this section, we will introduce recent studies on thermoelectric properties of SWCNTs.

Initially, most of the research was related to a single rope of SWCNTs alone [75-77] or to transport phenomena of mat samples [78-82]. Then, with the development of separation technologies of chirality in the 2000s [83], SWCNTs with different electronic structures, i.e., metallic and semiconducting SWCNTs, can be separated [84-89]. As a result, since the 2010s, research on the thermoelectric properties of SWCNTs has become more active, taking advantage of the diversity of their electronic structures [90,91]. In particular, semiconducting SWCNTs attracted much attention because their maximum value of S was predicted to show relatively large values about 1000-2000 μVK^{-1} [92-94], compared to the typical thermoelectric materials, such as Bi_2Te_3. Recently, Nakai et al. succeeded in enhancing the value of S (~170 μVK^{-1}) using purified semiconducting SWCNTs (>95%), exceeding the values (~60 μVK^{-1}) of unseparated SWCNTs [95]. Later studies also observed larger S of semiconducting SWCNTs than mixed or metallic SWCNTs [96,97].

Approaches to control the thermoelectric properties of SWCNTs have also been conducted. For example, the sign of S reverses depending on whether the dominant carrier inside the thermoelectric material is electrons (*n*-type) or holes (*p*-type). In general, *n*-

type and *p*-type thermoelectric materials are arranged in series and alternately to fabricate thermoelectric devices with high efficiency [10]. Many research experimentally verified that SWCNT samples could be freely changed into *n*-type and *p*-type thermoelectric materials by doping with carriers [94,98-103], which is expected to be used for applications. Recently, structural control of CNT samples has been reported to improve their thermoelectric performance. CNTs have a large aspect ratio and a large σ parallel to the axis. The technology to orient the nanotube axis in one direction to form them into thin films and fibers has been established [104,105]. As a result, increase in σ in the oriented samples showed enhanced P (a maximum value ~3 $mWm^{-1}K^{-2}$) [106-109] close to that of Bi_2Te_3 (~4 $mWm^{-1}K^{-2}$ [20]). Composites with other materials also yield the increase of P, reported recently [110,111].

Lack of research on one-dimensionality

Research on thermoelectric properties of SWCNTs seems to be making steady progress. However, in all of the achievements, there was no clear identification regarding the performance improvement due to the 1D electronic structures expected by Hicks & Dresselhaus. In other words, there is no knowledge of how the vHs, which are characteristic of 1D electronic structures, affect thermoelectric properties and whether they actually improve thermoelectric performance significantly. Therefore, experimentally verifying the prediction of Dresselhaus et al., which is a guideline to improve thermoelectric properties from the approach of condensed matter physics, is an important issue that will strongly promote the development of thermoelectric materials and solve various social problems. In particular, the relationship between 1D electronic structure and thermoelectric properties, which is expected to have the most excellent performance, is the most important problem to be solved.

Even for SWCNTs, which are ideal materials for experimentally verifying this problem, the previous research has not solved it despite many thermoelectric studies. This is because the electronic structure of the SWCNT samples and the position of the chemical potential has not been precisely controlled in previous studies. Essentially, to experimentally observe the effect of the vHs on thermoelectric properties, we need to tune the chemical potential to the sharp vHs of the SWCNT samples. However, previous studies could

not establish such conditions and discussed the relationship between 1D electronic structure and thermoelectric properties in detail. The background of these issues is presented below, with examples regarding previous studies.

Problem (1): Unprecise control of electronic structure

The electronic structure of each chirality of SWCNTs is unique and can be roughly classified as metallic or semiconducting electronic structures. Thus, in a sample with a mixture of them, it would not be possible to discuss the physical properties of the individual electronic structure because the physical properties of each SWCNTs would be observed mixed together. For instance, Hayashi et al. theoretically calculated the effect on thermoelectric properties when a metallic type is mixed into a single chirality of the semiconductor type [112]. Their results showed that the presence of only 1% of the metallic type significantly reduced S of the semiconducting type from a few mV/K to tens of μV/K due to the presence of conducting path by the metallic SWCNTs. Therefore, chirality purity is a crucial factor in investigating the thermoelectric properties of SWCNTs with an accurate evaluation. However, the purity of the single chirality obtained by the conventional separation technique was about 98% at best [113]. In this situation, it was impossible to clearly observe the effect of the unique electronic structure of SWCNTs, i.e., vHs, on their thermoelectric properties.

Problem (2): Unprecise control of chemical potential

Since thermoelectric phenomena are caused by the transport of electrons and holes, the electronic structure around the chemical potential significantly influences thermoelectric properties. Therefore, to clarify the relationship between vHs and thermoelectric properties, we need to measure the properties when the chemical potential is located in the vicinity of their vHs. In the study of thermoelectric properties, the chemical potential is generally shifted by chemical molecular doping methods [94,101-103] and backgating methods [69,75,76,114,115]. However, in the former method, it is difficult to precisely control chemical potentials and to measure the thermoelectric properties near vHs. The latter method can continuously change the carrier doping amount; however, the limit of the charge injection amount prevented us from investigating the thermoelectric properties near the vHs. In this situation, it was impossible to observe the effect

of the vHs on thermoelectric properties clearly. However, there were only a few such systematically chemical-potential-modulated studies in 2016 when we started this study [98-100]. These studies also had the purity problem described in (1).

Then, after solving the above two experimental problems, we can enter the stage of investigating the relationship between 1D electronic structure and thermoelectric properties. However, we have another problem: there was little knowledge of which thermoelectric parameters could be used to observe the effect of vHs on thermoelectric properties.

Problem (3): Relationship between one-dimensional electronic structure and thermoelectric parameters

In the study of thermoelectric properties, we generally evaluate the thermoelectric parameters of S and P. To clarify the effect of the vHs on thermoelectric properties, we should know whether these thermoelectric parameters show behaviors that reflect the shape of the electronic structure. For metallic materials, we can use Mott's equation to correspond the relationship between S and the shape of the electronic structure, which has been discussed in many previous studies [61,62,94,98,116-118]. Therefore, in metallic SWCNTs, we should demonstrate whether the behavior of S depends on the 1D electronic structure. In semiconductors, however, S and P do not show qualitative behavior that reflect the shape of the electronic structure. For example, it has been theoretically shown that S in semiconductors has a maximum value near the center of the bandgap and decreases monotonically as the chemical potential moves toward the band edge, see **Figure 1.5** [92,119]. This behavior is not limited to 1D semiconductors with vHs but also applies to 2D and 3D semiconductors. Moreover, the maximum P is obtained near the band edge [112,119], which is also independent of the dimension of the material. Therefore, in semiconducting SWCNTs, it is difficult to clarify the effect of vHs on thermoelectric properties with conventional thermoelectric parameters S and P.

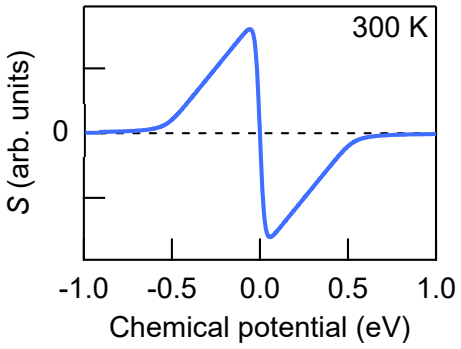

Figure 1.5. Typical behavior of Seebeck coefficient for 1D, 2D, and 3D semiconductors as a function of chemical potential. The band edge is set to ±0.5 eV.

1.2 Purpose of this thesis

On the basis of these backgrounds, the purpose of this thesis is to experimentally elucidate the relationship between 1D electronic structure of SWCNTs and thermoelectric properties. In other words, we aim to clarify how 1D electronic structures, i.e., the vHs, of SWCNTs effects on the thermoelectric properties and whether the improvement in thermoelectric performance can be embodied experimentally.

To achieve this goal, we solve the experimental problems in the conventional study of thermoelectric properties of SWCNTs. Specifically, we established a separation technique for high-purity single-chirality SWCNTs to precisely control the electronic structure. The thermoelectric properties of the obtained high-purity samples is measured under precise chemical potential control using the electrical double layer carrier injection method. Thus, our unique experimental method, which combines the precise control of the electronic structure and the chemical potential, enables us to discuss the thermoelectric properties by experimentally relating vHs to the chemical potential position. Taking advantage of the unique electronic structure of SWCNTs, we systematically investigate the metallic and semiconducting electronic structures, respectively, to comprehensively clarify the relationship between the 1D electronic structure and thermoelectric properties.

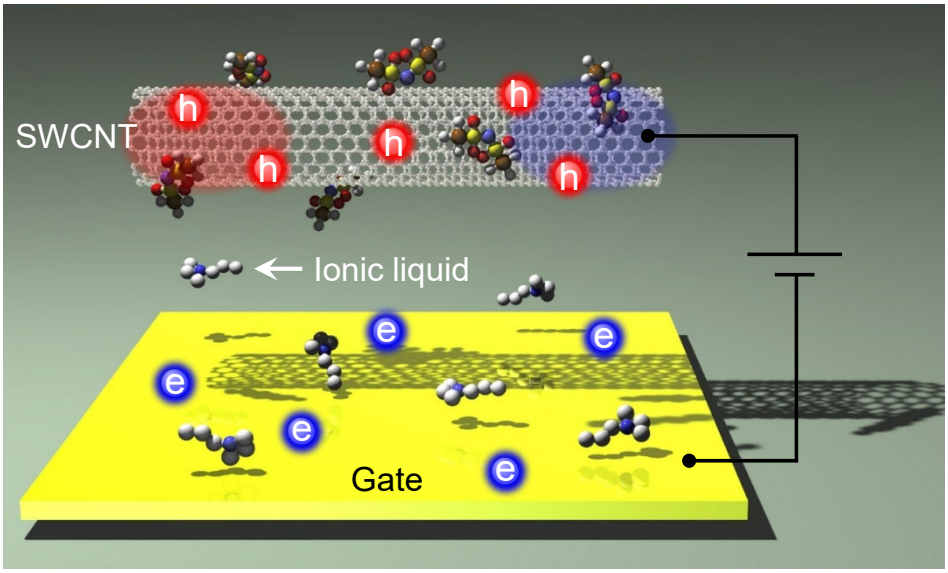

Figure 1.6. Schematic image of the thermoelectric measurement using electric double layer carrier injection method with ionic liquid.

1.3 Outline

The research on the above subjects is described in detail starting from Chapter 2. Then, we solve the problem (1) in Chapter 3, and the problems (2) and (3) in Chapters 4 and 5. The details of each chapter are shown below.

Chapter 2 describes the basic information necessary to investigate the thermoelectric properties of SWCNTs. First, the basic properties of the thermoelectric effect and the theoretical background of the uniqueness in 1D materials were explained. Secondly, we briefly described the separation and purification methods to prepare high-purity SWCNTs. Next, we explained the details of the measurement methods that can control the chemical potential of SWCNT films, and measure in-situ thermoelectric properties based on the ionic liquid electric double layer carrier injection method.

Chapter 3 describes the development of a new separation technique for single-chirality SWCNTs. The sample purity of SWCNTs is crucial to observe the one-dimensionality. However, conventional separation techniques using surfactants could not altogether remove the residual few percent of metallic SWCNTs in semiconducting single-chirality SWCNT separation. Here, we developed a new technique to obtain high-purity (>99%) single-chirality SWCNTs by improving a reported gel chromatography separation to precisely control the acidity, or pH, as an additional parameter. The pH-controlled method succeeded in completely removing the residual metallic SWCNTs because metallic and semiconducting types have different sensitivities in responding to changes in pH. The high-purity sample obtained in this chapter is used for thermoelectric measurements in the next chapter and later.

Chapter 4 systematically demonstrates the thermoelectric properties of high-purity semiconducting and metallic SWCNTs, and their mixtures. We observed the enhancement of thermoelectric performance due to the 1D electronic structure by adjusting the chemical potential of metallic SWCNTs at the vicinity of vHs. The enhancement was manifested in a simultaneous increase in σ and S. In conventional materials, there is a trade-off relationship between σ and S, which means that the increase of σ induces a decrease of S. However, the metallic SWCNTs violated the trade-off, demonstrating that the 1D

electronic structure can enhance the thermoelectric performance due to the quantum confinement effect. Furthermore, we experimentally showed the increase of σ without decreasing S by preparing macroscopically aligned metallic SWCNT thin films, indicating that the morphology control of SWCNT samples can lead to further performance improvement.

Chapter 5 identifies the traces of thermoelectric properties due to the 1D electronic structure in semiconducting SWCNTs. Using a simple model based on the Boltzmann transport equation, we showed that it is difficult to identify the 1D traces in S and P, the typical thermoelectric parameters. However, the L_{12} term, thermoelectrical conductivity term, was expected to reflect the dimensionality of the materials. In particular, the 1D electronic structure was expected to have a peak structure in L_{12} at the vHs as a function of the chemical potential. Here, we observed the peak structure in L_{12} on high-purity semiconducting SWCNTs thin films, consistent with the theoretical prediction. The linear response theory analysis and the experimental results of 2D semiconductors supported that the peak is a 1D trace originating from the electronic structure of SWCNTs. In the 1D system, the L_{12} term shows the peak structure in the low electrical conductivity region. We could understand the advantage of 1D materials as high thermoelectric performance materials from such behavior.

In Chapter 6, we summarized the conclusions obtained in this thesis.

Chapter 2

Thermoelectrics and Metrology

2.1 Thermoelectrics

2.1.1 Thermoelectric parameters

The Seebeck effect is one of the thermoelectric phenomena. Here, we consider a conducting sample with the length L along the x-axis and a temperature difference $\Delta T = T_{\mathrm{H}} - T_{\mathrm{C}}$ between the two ends, where T_{H} and T_{C} are the temperature at the hot end and the cold end, respectively. Due to the difference of the chemical potential between the ends, the electrons have a gradient distribution in the sample. In a steady state, where no net electric current flows, the gradient in the electron distribution produces a potential difference ΔV along the x-axis direction. This phenomenon is called the Seebeck effect. The Seebeck coefficient S, the ratio of the temperature difference ΔT to the potential difference ΔV, is defined by the relation

$$S \equiv -\frac{\Delta V}{\Delta T}. \tag{2.1}$$

The minus sign is assigned to match the type of charge; if the dominant carriers are holes, S is positive; if electrons, S is negative. According to the definition, the larger the absolute value of S, the larger the voltage obtained from the temperature difference. The value of S varies depending on the material. Therefore, materials with large S are generally valuable as thermoelectric materials, and we need to search for such materials.

S can be relatively easily measured in a macroscopic sample. However, predicting the properties is not straightforward. Thermoelectrics are transport phenomena of electrons or phonons. Moreover, since we deal with the scale of Avogadro's numbers, it is necessary to consider the statistical mechanical motion of these transport carriers. In this section, we will describe the thermoelectric properties based on the linear response theory. Here, we consider a system in which the electric field $\mathcal{E}$ and the temperature gradient dT/dx exist along the x-axis direction. The current density J is generally given by the

linear response theory as follows [119];

$$J = L_{11}\mathcal{E} - \frac{L_{12}}{T}\frac{dT}{dx}. \tag{2.2}$$

The response functions L_{11} and L_{12} are referred to as electrical conductivity and thermoelectric conductivity, respectively. The first term represents the current density produced by the electric field, and the second represents the current density produced by the temperature gradient. When the net current density J is zero ($J = 0$), S can be written by L_{11} and L_{12} as

$$S = \frac{1}{T}\frac{L_{12}}{L_{11}}, \tag{2.3}$$

where we used the relationship $\mathcal{E} = \Delta V/L$ and $dT/dx = \Delta T/L$. Furthermore, the power factor P, which is one of the indicators of thermoelectric performance, can be expressed as

$$P \equiv S^2\sigma = \frac{1}{T^2}\frac{L_{12}^2}{L_{11}}. \tag{2.4}$$

Therefore, we can see that the physical quantities S and P, often crucial in thermoelectric properties, are constituted by L_{11} and L_{12}.

Next, we consider L_{11} and L_{12} in more detail. According to Sommerfeld and Bethe in 1933 [119-123], L_{11} and L_{12} are described as

$$L_{11} = \int_{-\infty}^{\infty} dE \left(-\frac{\partial f(E-\mu)}{\partial E}\right) \alpha(E), \tag{2.5}$$

$$L_{12} = \frac{1}{q}\int_{-\infty}^{\infty} dE \left(-\frac{\partial f(E-\mu)}{\partial E}\right) (E-\mu)\alpha(E), \tag{2.6}$$

where q is the charge of a carrier, E is the energy, μ is the chemical potential, $\alpha(E)$ is the spectral conductivity, and $f(E-\mu)$ is the Fermi-Dirac distribution function expressed by

$$f(E-\mu) = \frac{1}{\exp\left(\frac{E-\mu}{k_{\mathrm{B}}T}\right) + 1}. \tag{2.7}$$

In this thesis, we call the equations (2.5) and (2.6) as the Sommerfeld-Bethe relation. The above equations will be used as the fundamental equations throughout this study.

2.1.2 Boltzmann expression

According to the Sommerfeld-Bethe equation, to calculate L_{11} and L_{12}, which determine the behavior of thermoelectric properties, we only need to calculate a universal spectral conductivity $\alpha(E)$. However, since it is not easy to obtain the exact spectral conductivity analytically, we use some approximations. Here, we use the Boltzmann transport equation for electrons to show the standard expression for thermoelectric properties. Although the Boltzmann equation is semiclassical, it is very effective in describing the transport phenomena of electrons by adding some quantum mechanical corrections.

To describe the conduction of electrons, we introduce a nonequilibrium distribution function f, where f means the probability that an electron of a certain wavenumber k exists at position x at time t. For simplicity, we consider the one-dimensional case below. Using $f = f(x, k, t)$, the current density J per unit volume can be expressed as

$$J = -e \sum_k f(x, k, t) v(k) \,. \tag{2.8}$$

Here e is the elementary charge, and v is the velocity of the electron, where $v = \hbar k/m$. Note that $\hbar$ is the Dirac constant, and m is the mass of the electron. Hence, we can obtain an expression for the electric current by determining f in the presence of electric field $\mathcal{E}$ and temperature gradient ∇T in the system. Here, we use the Boltzmann equation;

$$\frac{\partial f}{\partial t} + \frac{\partial x}{\partial t}\frac{\partial f}{\partial x} + \frac{\partial k}{\partial t}\frac{\partial f}{\partial k} = \left(\frac{\partial f}{\partial t}\right)_{\text{coll}} \tag{2.9}$$

to obtain the solution for f. Often, the left-hand side is called the drift term, and the right-hand side is called the collision term.

Under a weak external field, the deviation g of the distribution function from the equilibrium state is regarded as small, and thus we linearize the Boltzmann equation (2.9). In other words, the nonequilibrium distribution function f can be expressed as

$$f = f^0 + g \tag{2.10}$$

with g deviation from the equilibrium distribution function f^0, which is given by the Fermi-Dirac distribution function. Specifically, under the assumption of local equilibrium, since we can introduce the temperature $T(x)$ and the chemical potential $\mu(x)$ that

depend on the position x, the Fermi-Dirac distribution function can be written as

$$f^0(x,k) = \frac{1}{\exp\left(\frac{E(k)-\mu(x)}{k_{\mathrm{B}}T(x)}\right)+1}. \tag{2.11}$$

Substituting f in Eq. (2.10) into the Boltzmann equation, we get

$$\frac{\partial g}{\partial t} + \left(-\frac{\partial f^0}{\partial E}\right) v \cdot \left(e\mathcal{E} + \nabla\mu + \frac{E-\mu}{T}\nabla T\right) = \left(\frac{\partial f}{\partial t}\right)_{\mathrm{coll}}. \tag{2.12}$$

For simplicity, we do not consider the magnetic field here. We omit the detailed derivation of (2.12). Note in the derivation process, the relations $\hbar\dot{k} = -e\mathcal{E}$ and $E = \hbar^2k^2/2m$ have been used.

Within the relaxation-time approximation, the collision term on the right-hand side of Eq. (2.12) can be rewritten as

$$\left(\frac{\partial f}{\partial t}\right)_{\mathrm{coll}} = -\frac{g}{\tau_k}. \tag{2.13}$$

Since $\partial g/\partial t = 0$ in the steady state, solving the Boltzmann equation for g yields

$$g = \left(-\frac{\partial f^0}{\partial E}\right)\tau_k v \cdot \left(-e\mathcal{E} - \frac{E-\mu}{T}\nabla T\right), \tag{2.14}$$

where $\nabla\mu$ is included in the term of electric field $\mathcal{E}$.

Substituting the obtained nonequilibrium distribution function f into the current density (Eq. (2.8)), and taking into account the spin, we obtain

$$\begin{aligned} J &= -2e\sum_k f(x,k)v(k) \\ &= -2e\sum_k \tau_k v^2 \left(-\frac{\partial f^0}{\partial E}\right)\left(-e\mathcal{E} - \frac{E-\mu}{T}\nabla T\right). \end{aligned} \tag{2.15}$$

Here, we have applied the relation

$$-2e\sum_k f^0(x,k)v(k) = 0, \tag{2.16}$$

which means the net current is zero in the equilibrium state. By comparing (2.15) with the expression for current density obtained in the linear response theory (Eq. (2.2)), we obtain

$$J = L_{11}\mathcal{E} - \frac{L_{12}}{T}\nabla T, \tag{2.17}$$

where L_{11} and L_{12} are

$$L_{11} = 2e^2 \sum_k \tau_k v^2 \left(-\frac{\partial f^0}{\partial E}\right), \tag{2.18}$$

$$L_{12} = -2e \sum_k \tau_k v^2 \left(-\frac{\partial f^0}{\partial E}\right)(E-\mu), \tag{2.19}$$

respectively. Under the free electron approximation, we modify the summation of the wavenumber to the form of an energy integral, which can be rewritten as

$$L_{11} = e^2 \int dE \left(-\frac{\partial f^0}{\partial E}\right) \rho(E)\tau(E)v^2(E), \tag{2.20}$$

$$L_{12} = -e \int dE \left(-\frac{\partial f^0}{\partial E}\right) \rho(E)\tau(E)v^2(E)(E-\mu), \tag{2.21}$$

where $\rho(E)$ is the density of states. These are L_{11} and L_{12} in Boltzmann expression. The spectral conductivity can be written as

$$\alpha(E) = e^2\rho(E)\tau(E)v^2(E). \tag{2.22}$$

Therefore, we could relate the material characteristics such as the electronic structure and the electron conductions to thermoelectric properties.

2.1.3 Mott formula

In this section, we use the spectral conductivity to calculate the Seebeck coefficient. Consider systems where the chemical potential is in the middle of the band, as in metals and degenerate semiconductors. In this situation, room temperature can be regarded as sufficiently low temperature $\mu \gg k_{\mathrm{B}}T$. Using the Sommerfeld expansion

$$\int dE\, G(E) \left(-\frac{\partial f^0}{\partial E}\right) = G(\mu) + \frac{\pi^2}{6}(k_{\mathrm{B}}T)^2 G''(\mu) + \cdots, \tag{2.23}$$

L_{11} and L_{12} can be written as

$$L_{11} = \alpha(\mu), \tag{2.24}$$

$$L_{12} = -\frac{\pi^2}{3e}(k_{\mathrm{B}}T)^2\alpha'(\mu). \tag{2.25}$$

Therefore, substituting L_{11} and L_{12} into Eq. (2.3) results in

$$S = -\frac{\pi^2 k_{\mathrm{B}}^2 T}{3e} \frac{\alpha'(\mu)}{\alpha(\mu)} \tag{2.26}$$

or

$$S = -\frac{\pi^2 k_{\mathrm{B}}^2 T}{3e} \frac{\partial \ln \alpha(E)}{\partial E}\Big|_{E=\mu}. \tag{2.27}$$

These equations are called the Mott formula and represent the Seebeck coefficient in the degenerate region [116,124].

Mott's formula is proportional to the energy derivative of the spectral conductivity. For many metals, the energy dependence of $\alpha(E)$ is almost constant at the Fermi energy. Therefore, we can understand the observed fact that the Seebeck coefficient of metals is tiny.

Furthermore, this formula indicates that S decreases as α in the denominator increases, that is, as the electrical conductivity increases. In fact, in many thermoelectric materials, it is known that there is a trade-off relationship in which the absolute value of S decreases when the electrical conductivity increases [14]. Thus, in conventional inorganic thermoelectric materials, a moderate amount of doping is required to maximize the power factor P ($= S^2\sigma$), and the performance has been limited [15]. Therefore, a new thermoelectric material design concept is needed to overcome this situation. In particular, simultaneous increase of σ and S is generally desirable in order to enhance P.

One option is to make the derivative term of α as large as possible in Mott's formula. To better understand the behavior of S, we substitute the α obtained from the Boltzmann equation into Mott's formula (2.27) and transform [61,94] it into

$$S = -\frac{\pi^2 k_{\mathrm{B}}^2 T}{3e} \left[\frac{\partial \ln \rho(E)}{\partial E} + \frac{\partial \ln D(E)}{\partial E}\right]_{E=\mu}. \tag{2.28}$$

Note that $D(E)$ is the diffusion coefficient and is summarized as a term representing the conduction of electrons. Here, we focus on the first term, which contains the derivative of the density of states. Hence, if the electronic structure has an abrupt change in the energy dependence of the density of states, we can expect a significant value of S. **Figure 2.1** shows the simple density of states of a d-dimensional ($d = 1,2,3$) material [65]. The lower-dimensional materials have a point where the density of states changes significantly

due to quantum confinement effects. Therefore, the electronic structure of low-dimensional materials will lead to a large S through an increase in the derivative term of α. Furthermore, in the region where the density of states increases, the electrical conductivity can also increase simultaneously. Thus, it is suggested that the low-dimensional electronic structure can significantly increase P, breaking the trade-off relationship in conventional thermoelectric materials mentioned above.

In particular, one-dimensional materials have a point of divergence in the density of states and the steepest electronic structure. This point is called the van Hove singularity (vHs). Since SWCNTs are one-dimensional materials with distinct vHs, they are expected to have a large thermoelectric performance derived from their one-dimensional electronic structure for the above reasons. With this background, the experimental investigation of the thermoelectric properties of metallic SWCNTs and the actual observation of the trade-off breaking are discussed in Chapter 4 of this thesis.

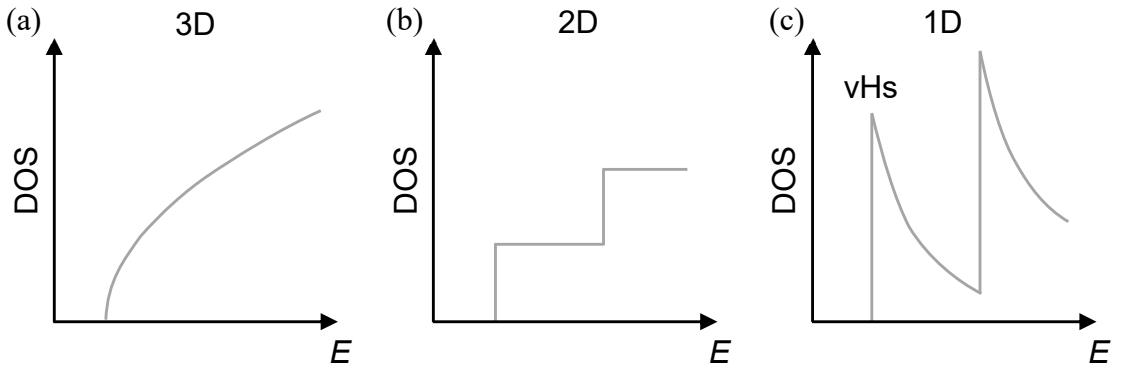

Figure 2.1. Density of states of *d*-dimensional materials. The density of state (DOS) as a function of the energy E of (a) 3D, (b) 2D, and (c) 1D. The lower the dimensionality, the sharper the electronic structures. 1D DOS has some peak structures called van Hove singularity (vHs).

2.1.4 Non-degenerate region of semiconductors

We have reviewed the thermoelectric properties for metals, i.e., degenerate regions. However, the expression of S for the case where the chemical potential is located in the bandgap of the semiconductor, i.e., the non-degenerate region of the semiconductor, is different. It is a good approximation to treat the free electrons in this case as classical

particles following the Boltzmann distribution function

$$f^0 \approx \exp\left(-\frac{E-\mu}{k_{\mathrm{B}}T}\right), \tag{2.29}$$

instead of the Fermi-Dirac distribution function. Hence, S in the non-degenerate region is generally expressed in the form

$$S = -\frac{k_{\mathrm{B}}}{e}\left(\frac{E_{\mathrm{C}}-\mu}{k_{\mathrm{B}}T} + A\right), \tag{2.30}$$

where E_{C} is the energy at band edges of semiconductors and A is a constant term independent of the chemical potential [15,116]. The details of the derivation can be found in Section 5.2.

It is clear from Eq. (2.30) that S in the non-degenerate region does not reflect the information of the electronic structure in the chemical potential dependence. Therefore, unlike metallic SWCNTs, it is not possible to discuss the thermoelectric properties of the one-dimensional electronic structure by looking S in semiconducting SWCNTs. With this background in mind, we clarify the relationship between the one-dimensional electronic structure and thermoelectric properties of semiconducting SWCNTs by focusing on the behavior of L_{12}, which is described in Chapter 5 of this thesis.

2.2 Experimental methods

In order to clarify the relationship between the one-dimensional electronic structure and thermoelectric properties of SWCNTs, there are two experimental requirements. First, the purity of the SWCNTs sample should be high, and second, the chemical potential should locate near vHs. Regarding the first point, the electronic structure must retain the sharp vHs that characterizes the one-dimensionality to observe the one-dimensional thermoelectrics. For example, when we use a sample with low purity, i.e., a mixture of several SWCNTs with different band gaps, the observable properties are averaged, and the sharp one-dimensionality cannot be observed. We recognize that this is a severe problem in conventional research on thermoelectric properties of SWCNTs. Therefore, it is necessary to prepare extremely high purity SWCNTs. This study adopted the gel chromatography separation method to achieve high purity of single chirality SWCNTs. Regarding the second point, precise control of the chemical potential is necessary to observe the one-dimensionality. The thermoelectric properties derived from the one-dimensional electronic structure are expected to emerge when the chemical potential is located near vHs. Therefore, it is required to change the chemical potential of the SWCNTs sample precisely and continuously measure the thermoelectric properties. In this study, we employed the ionic liquid-based electric double layer carrier injection method to measure the thermoelectric properties of SWCNT thin films.

2.2.1 Gel chromatography separation

Various methods have been established to synthesize SWCNTs, such as the Arc discharge method, the CoMoCAT method, and the HiPco method. In all of these methods, the synthesized SWCNTs contain a mixture of multiple chiralities (*n,m*). However, it is difficult to synthesize only one species selectively at present. This section introduces the basics of the separation methods using surfactants and gels to help the reader's understanding of Chapter 3.

SWCNTs form bundles in which SWCNTs are tightly packed together by van der Waals forces and π-π bonds [125]. A bundle consists of more than a few dozen SWCNTs and contains various chiralities. In order to extract and separate a specific chirality, this

bundle must first be disassembled.

Surfactants can isolate and disperse SWCNTs [83]. For example, applying ultrasonics to SWCNTs in a surfactant solution causes the bundles to dissolve on impact. The physical adsorption of the surfactant on the surface of the SWCNTs, which is hydrophobic, results in the isolated dispersion of SWCNTs. Then, after the specific chirality is separated, the surfactant can be easily removed from the surface of SWCNTs with an organic solvent such as methanol. Therefore, SWCNTs samples with high purity can be obtained.

Several types of surfactants are used for the dispersion of SWCNTs. In this study, sodium dodecyl sulfate (SDS), sodium cholate (SC), and sodium deoxycholate (DOC) were used in the separation [126]. The reason for using several types of surfactants is that each surfactant has a different adsorption capacity for different types of SWCNTs [86,127]. For example, SDS tends to adsorb on metallic SWCNTs, SC tends to adsorb on semiconducting SWCNTs, and DOC tends to adsorb on SWCNTs with small diameters. The combination of these surfactants can separate SWCNTs with high purity.

The separation method using agarose gel is called the gel chromatography separation method. This method does not require large-scale equipment such as an ultracentrifuge and can separate a large number of samples at a low cost [87]. In the gel separation, we separate SWCNTs based on the difference in the adsorption force of the surfactant on each chirality. Different amount of surfactant adsorbed on the surface of SWCNTs depending on the chirality creates a difference in the adsorption force between SWCNTs and the gel. As a result, we can separate the chiralities. For example, SDS tends to adsorb on metallic types. Therefore, when an SDS solution containing metallic and semiconducting SWCNTs is poured into a gel, the metallic type, which has more SDS attached, cannot adsorb to the gel and flows out. On the other hand, the semiconducting type adsorbs less SDS than the metallic type and thus adsorbs on the gel. As a result, the metallic and semiconducting SWCNTs can be separated [87].

In 2011, it was reported that 13 kinds of single chirality SWCNTs were successfully separated by gel separation using SDS aqueous solution system [88]. Furthermore, a combination of several surfactants such as SC and DOC instead of SDS alone made it possible

to separate more types of single chirality SWCNTs [113,126].

In the gel separation, we use a step-wise elution process to separate the SWCNTs. This technique was used in the separation of Chapter 3. First, the unseparated SWCNT dispersion is poured into the gel. At this phase, the surfactant concentration is adjusted to allow the SWCNTs to adsorb to the gel so that the SWCNTs remain in the gel. Subsequently, a surfactant solution with a slightly higher concentration is poured into the gel. Then, among the SWCNTs adsorbed on the gel, the chirality with the strongest adsorption force with the surfactant is eluted. The next chirality with the strongest adsorption to the surfactant will be eluted by further increasing the surfactant concentration. Chirality separation can be performed by repeating this process and collecting the eluent separately. In Chapter 3, in addition to the surfactant concentration, the acidity, or pH, of the solution was varied to perform the step-wise elution process.

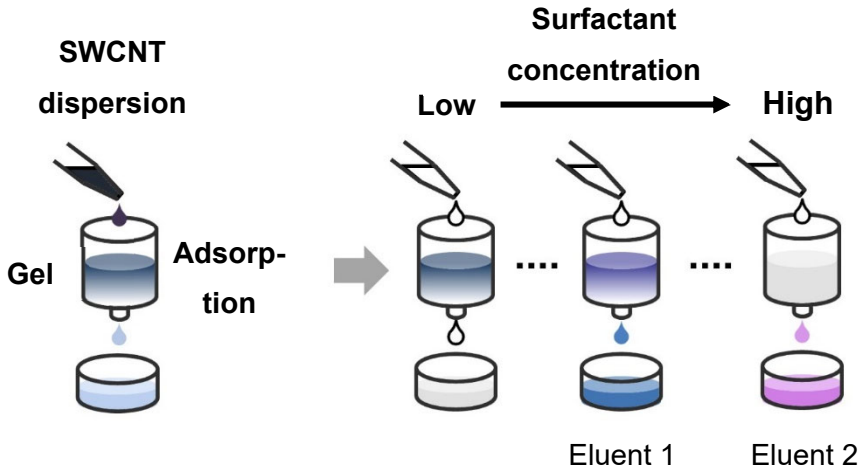

Figure 2.2. Step-wise process of gel chromatography separation. (a) Adsorption process. (b) Step-wise separation process. The surfactant concentration is gradually increased. Collecting the eluent separately; for example, Eluent 1 and Eluent 2 contain different chiralities.

2.2.2 Electric double layer carrier injection

In order to shift the chemical potential of a material, it is necessary to control the carrier concentration. In general, doping by elemental substitution or molecular doping is used to change the carrier concentration of thermoelectric materials. However, these

methods have some problems for thermoelectric property measurement, such as it is not easy to fine-tune the degree of doping or to change the amount of doping in the same sample continuously. Therefore, this section introduces the carrier injection method using the electric field effect and shows the principle of the chemical potential control used in this study.

Field-effect transistors (FETs) that utilize a capacitor structure are noteworthy for their ability to continuously and reversibly change the doping level of the sample by increasing or decreasing the gate voltage. **Figure 2.3** shows a schematic diagram of a back-gate FET. A capacitance structure is formed between the sample and the gate electrode across an insulator (~several hundred nm). In the figure, negative charges are induced on the surface of the sample by applying a positive voltage to the gate electrode. Thus, precise *p*-type and *n*-type doping control is possible by varying the gate voltage finely. Furthermore, since there is no need to add impurities, the effect of impurities on the physical properties can be eliminated. Therefore, the FET structure, in which the amount of doping can be controlled continuously and reversibly, is suitable for many physical property measurements. For example, thermoelectric property measurements using back-gate FETs were vigorously performed on single nanowires, nanotubes, and nanodots [69,75,76,114,115].

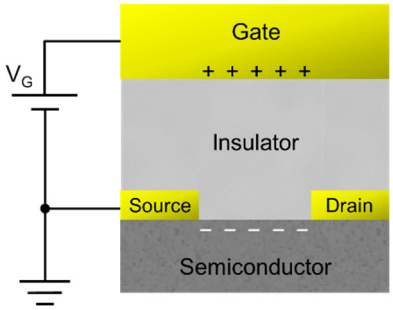

Figure 2.3. Schematic image of the back-gating field-effect transistors.

However, back-gating is not suitable for doping bulk or thin-film materials. As shown in **Figure 2.3**, the charge induced by the capacitance structure is only induced on the very thin surface of the sample (~1 nm). In the region away from the surface, carriers cannot be doped due to the screening effect. This situation is undesirable for the thermoelectric property measurement of SWCNTs, which is the purpose of this study. For example, consider the case where we prepare a high-purity and separated SWCNT thin film. If there is a difference in the doping level between the surface and the internal part of the film, we can expect to have a situation where SWCNTs with different chemical potentials

coexist. Although the SWCNTs sample is separated with high purity, the apparent purity may be reduced when measuring the physical properties. In order to measure the thermo-electric properties derived from the sharp vHs, it is necessary to dope the entire SWCNTs film uniformly.

This study used an ionic liquid electric double layer transistor (EDLT) structure to dope the sample. A schematic of the EDLT is shown in **Figure 2.4**. The basic structure is similar to a back-gate FET, but the EDLT uses an ionic liquid as the gate dielectric. An ionic liquid is a salt consisting of cations and anions, and is a viscous liquid at room temperature [**Figure 2.4**(a)]. When a gate voltage is applied with the sample immersed in the ionic liquid, the ionic liquid is moved by the electric field [**Figure 2.4**(b)], forming two capacitance structures, or electric double layers, on the sample surface and the gate electrode surface [**Figure 2.4**(c)]. The thickness of the electric double layer capacitor is typically a few nanometers, and the extremely large capacitance results in high-density carrier doping. In particular, in contrast to back-gate FETs, for samples with a network structure such as SWCNTs, the ionic liquid can penetrate the interior of the thin film, allowing carrier accumulation throughout the entire thin film. Therefore, the electric double layer carrier injection method using ionic liquids is the most suitable method for

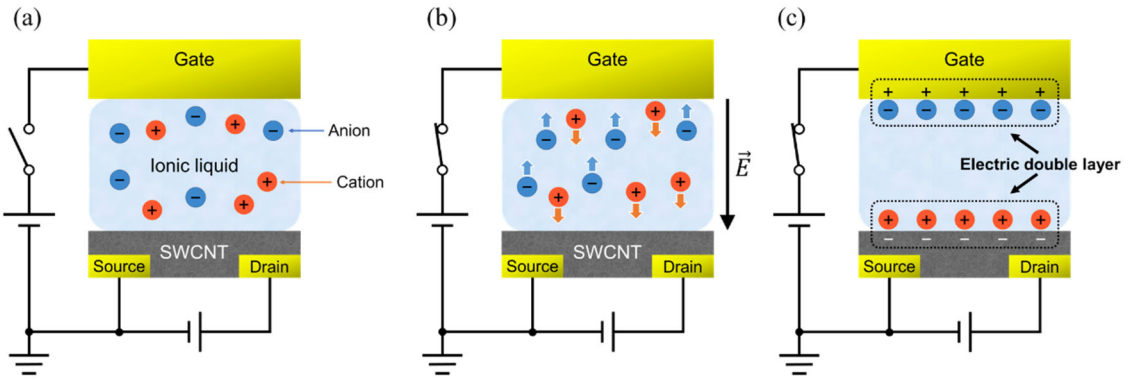

Figure 2.4. Schematic diagram of an electric double layer transistor. (a) Before electric double layer formation. The ionic liquid is not polarized, and the SWCNTs are not doped with carriers. (b) Immediately after the gate voltage is applied. The gate voltage causes the ionic liquid to move. (c) After the formation of the electric double layer. The ionic liquid is polarized, forming an electric double layer on the surface of the gate electrode and the sample, and the carriers flowing from the source accumulate in the sample.

controlling the chemical potential of SWCNTs thin films.

2.2.3 Thermoelectric measurement

We prepared a device to measure thermoelectric properties while controlling the chemical potential by the electric double layer carrier injection method described in the previous section. The measured properties are the electrical conductivity and Seebeck coefficient of SWCNTs. A detailed description of the fabrication process of the device is given in Appendix. **Figure 2.5**(a) shows the overall view of the device, where S is the source electrode, D is the drain electrode, and R is the reference electrode.

All measurements were performed in a vacuum to prevent the oxygen and moisture in the air from affecting the measurements and eliminate thermal diffusion from the device into the air. Therefore, a vacuum cryogenic prober (Grail 10-Helips-4-R, Nagase Engineering) was used in this study. A photograph of the prober is shown in **Figure 2.5**(b). After the device was placed in the prober, a vacuum pump (HiCube 80 Classic, Pfeiffer Vacuum) was used to create a vacuum (~10^{-4} Pa) in the prober.

First, we performed a transport measurement to check that the EDLTs were adequately driven. **Figure 2.6** shows a simplified schematic of the relationship between the device and the measurement instruments. The measurement instruments used were a two-

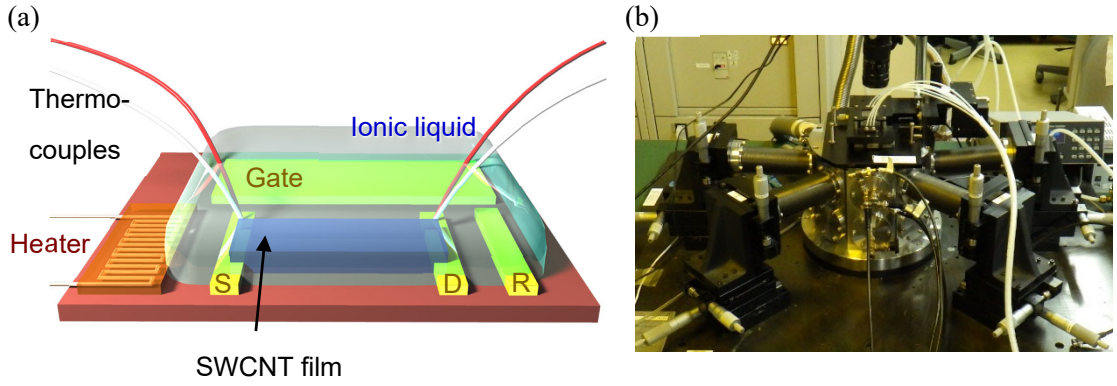

Figure 2.5. Measurement setup for the thermoelectric properties. (a) Device structure for combining the Seebeck measurements and electric double layer carrier injection method. (b) Picture of a vacuum cryogenic prober.

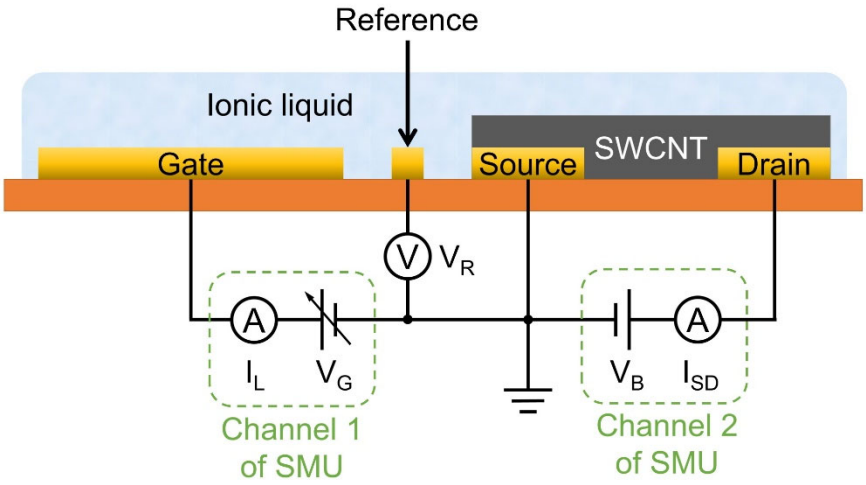

Figure 2.6. Schematic diagram of the transport measurement. Channel 1 of the source meter unit (SMU) was connected to the gate and source electrodes, applying the gate voltage V_{G} and measuring the leak current I_{L}. Channel 2 of SMU was connected to the drain and source electrodes, applying the bias voltage V_{B} and measuring the drain current I_{SD}. The source electrode was connected to the ground.

channel model source meter unit (SMU, 2636A, Keithley Instruments) and a digital multimeter (DMM, 2000, Keithley Instruments). Channel 1 of the SMU was connected to the gate and source electrodes. The gate voltage V_{G} was applied, and the current flowing here was measured as the leak current I_{L}. The source electrode was connected to the ground. Then, the reference voltage V_{R}, which was effectively applied to the sample by the electric double layer capacitor, was measured with a DMM. Next, channel 2 of the SMU was connected to the source and drain electrodes using a two-terminal method, and the drain current I_{SD} was measured when a constant bias voltage V_{B} was applied.

In the transport measurement, the gate voltage V_{G} varied in the range of approximately +3.2V to −2.8V, while the bias V_{B} was fixed. This voltage range of V_{G} corresponds to the potential window of the ionic liquid TMPA-TFSI used in this study. Applying positive V_{G} leads to the injection of electrons into the sample, and applying negative V_{G} leads to the injection of holes. The drain current I_{SD} changes with the carrier injection, and the ON/OFF ratio depends on the type of sample (e.g., semiconductor type or metal type).

The electrical conductivity can be obtained from the measured I_{SD} and the shape

of the film. The thickness d of the film was measured by the Atomic Force Microscope (AFM). Assuming that the length of the channel is L and the width of the channel is w, the electrical conductivity is obtained as

$$\sigma(V_{\mathrm{G}}) = \frac{1}{\rho} = \frac{L}{dw}\frac{I_{\mathrm{SD}}(V_{\mathrm{G}})}{V_{\mathrm{B}}}.$$

After confirming the successful operation of the EDLT, we measured the Seebeck coefficient. A simplified schematic of the relationship between the device and the measurement instruments is shown in **Figure 2.7**. The measurement instruments used were one 2-channel model source meter unit (SMU, 2636A, Keithley Instruments), three digital multimeters (DMM, 2000, Keithley Instruments), and one nanovoltmeter (2182A, Keithley Instruments). Channel 1 of the SMU was connected to the gate and source electrodes. The gate voltage V_{G} was applied, and the current flowing here was measured as the leak current I_{L}. The source electrode was connected to the ground. Then, the reference voltage V_{R}, which was effectively applied to the sample by the electric double layer capacitor, was measured with a DMM. Then, one side of the sample was heated by

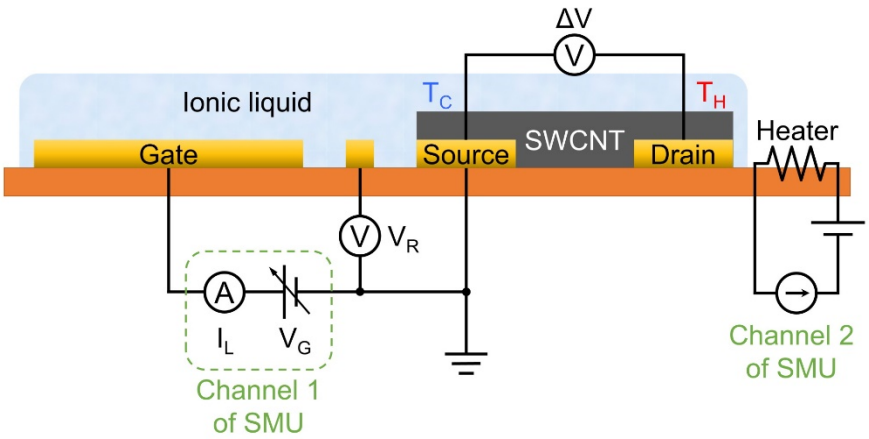

Figure 2.7. Schematic diagram of the Seebeck measurement. Channel 1 of the source meter unit (SMU) was connected to the gate and source electrodes, applying the gate voltage V_{G} and measuring the leak current I_{L}. Channel 2 of SMU was connected to the heater. The source electrode was connected to the ground. The temperature T_{H} and T_{C} of the hot and cold parts, respectively, was measured by two digital multimeters. The thermoelectric voltage ΔV between the both ends of the sample was measured by the nanovoltmeter.

connecting channel 2 of the SMU to a heater and applying current to it. Two other DMM were used to measure the voltage of the K-type thermocouple and read the temperature T_{H} and T_{C} of the hot and cold parts, respectively. Finally, the thermoelectric voltage ΔV generated through the Seebeck effect of the sample was measured by connecting a nanovoltmeter between the Alumel wires of the thermocouples at both ends of the thin film.

In the Seebeck coefficient measurement, the chemical potential dependence of the Seebeck coefficient was measured by varying V_{G} in the range from +3.2V to −2.8V as in the transport measurement. Immediately after applying V_{G}, the ΔV between thermocouples is not stable due to the movement of ionic liquid, so the measurement of the Seebeck coefficient was carried out after waiting with V_{G} applied for about 30 min.

Here, the potential difference ΔV is measured between the Alumel wires of the thermocouples attached at both ends of the sample, which means that we measure the integrated voltage both due to the Seebeck effect of the SWCNT thin film and the Seebeck effect of the Alumel wires. Hence, we removed the contribution of the Seebeck effect of the Alumel wires as follows. The schematic circuit for the sample and thermocouples is shown in **Figure 2.8**. Assuming that the reference temperatures T_0 of the two sets of thermocouples are equal, the potential difference measured in one circuit cycle is expressed by

$$\begin{aligned}\Delta V_{\mathrm{ALL}} &= -\int_{T_{\mathrm{H}}}^{T_0} S_{\mathrm{Alumel}} dT - \int_{T_{\mathrm{C}}}^{T_{\mathrm{H}}} S_{\mathrm{Sample}} dT - \int_{T_0}^{T_{\mathrm{C}}} S_{\mathrm{Alumel}} dT \\ &= -\int_{T_{\mathrm{C}}}^{T_{\mathrm{H}}} (S_{\mathrm{Sample}} - S_{\mathrm{Alumel}}) dT \\ &= -\left(S_{\mathrm{Sample}} - S_{\mathrm{Alumel}}\right) \cdot (T_{\mathrm{H}} - T_{\mathrm{C}})\end{aligned}$$

using the Seebeck coefficient of the sample S_{Sample} and the Alumel wires S_{Alumel} (~ −16.8 μVK^{-1}). Therefore, S_{Sample} is calculated by

$$S_{\mathrm{Sample}} = -\frac{\Delta V_{\mathrm{ALL}}}{T_{\mathrm{H}} - T_{\mathrm{C}}} + S_{\mathrm{Alumel}}.$$

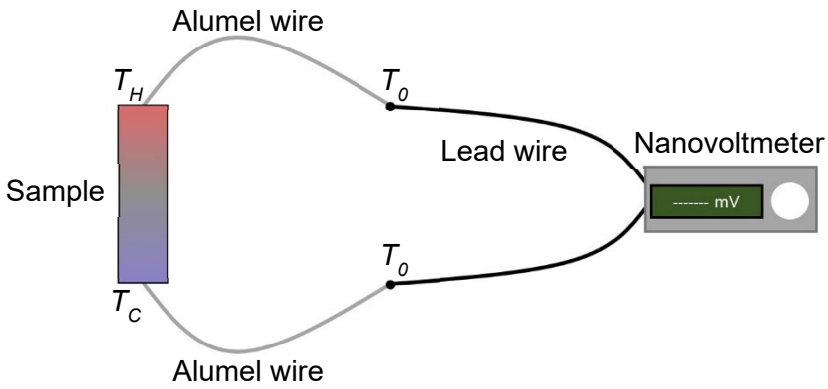

Figure 2.8. Connection diagram of the nanovoltmeter. The reference temperature at the connection between the lead wire and the Alumel wire is constant at T_0. The temperatures at both ends of the sample are T_{H} and T_{C}. The Seebeck coefficient of the sample is S_{Sample} and the Alumel wire is S_{Alumel}.

Chapter 3

Extraction of High-Purity Single-Chirality SWCNTs through Precise pH Control

The preparation of single-chirality single-walled carbon nanotubes (SWCNTs) is of great importance to comprehensively understand their physical properties and for applications. The high-purity separation of single-chirality SWCNTs has been reported using gel chromatography with a mixed surfactant system, but further improvements are necessary to enhance the purity of the resulting single-chirality SWCNTs. In this study, we focused on using pH as a parameter to improve the separation purity and investigated its influence on mixed surfactant-based purification. The pH of the mixed surfactant solution was precisely controlled with carbon dioxide bubbling with an accuracy of approximately ±0.1. Using this eluent with a series of different pH values, we achieved diameter-selective separation of the SWCNTs. Moreover, we found that the residual metallic SWCNTs could be completely removed under the proper pH condition. Finally, on the basis of these findings, we produced single-chirality SWCNTs with a purity of more than 99% without residual metallic SWCNTs.

3.1 Introduction

Developing techniques for preparing single-chirality single-walled carbon nanotubes (SWCNTs) is very important for comprehensively understanding the physical properties of SWCNTs in thin films and their transistor and biomedical applications [126,128,129]. To date, various types of purification techniques for single-chirality SWCNTs have been reported, such as DNA-based separation [130-132], density gradient ultra-centrifugation (DGU) [128,133-135], aqueous two-phase extraction (ATP) [136-138], and gel chromatography [88,113,126,139,140]. Most of the methods have employed several different surfactants, such as sodium dodecyl sulfate (SDS), sodium cholate (SC), and sodium deoxycholate (DOC), to produce monodispersions of SWCNTs and extract

SWCNTs with a specific electronic structure. In the case of the gel chromatography method, it was recently revealed that using a mixed surfactant system, containing SC, DOC, and SDS, is crucial for high-purity separations of single-chirality SWCNTs [126]. In this method, precisely controlling the parameters (e.g., the composition of the mixed surfactants) is crucial for achieving high-purity separation. However, in the extracted solutions with the single-chirality, other types of chirality have still been present (3−7%), and thus finding other controllable parameters is important for improving the purity of separated single-chirality SWCNTs.

In 2011, Hirano et al. reported that pH was the important parameter in gel chromatography using a single surfactant system of SDS, which influenced the metallic/semiconducting separation of SWCNTs [141]. They reported that a decrease in the pH led to oxidation of the SWCNTs and an increase in their SDS coverage, which changed the interactions between the SDS-wrapped SWCNTs and the gel. According to their results, semiconducting SWCNTs became nonadsorbed to the gel at pH values less than 7. It is known that the pH of an SDS solution can reach ~5.7 due to atmospheric carbon dioxide (CO_2) [142]; thus, such separation processes can be sensitive to the atmosphere, and their proposed pH control is important for stable separations. In contrast, in mixed surfactant systems, it is necessary to use not only SDS but also SC and DOC, and it has been reported that SC- and DOC-wrapped SWCNTs become unsusceptible to oxidation, i.e., pH [143]. Therefore, the effect of pH may be different from that in usual SDS systems. However, studies regarding the influence of pH on mixed surfactant-based purification processes for single-chirality SWCNTs have not been conducted.

This study systematically investigated the effects of pH on gel chromatography using a mixed surfactant system and demonstrated further purification of single-chirality SWCNTs by precise pH control. The pH was controlled using CO_2, which is known to decrease the pH of SDS systems. The pH was easily changed by CO_2 bubbling, and hence, we prepared a series of solutions with different pH values. Chirality separation was conducted using these eluents with a series of different pH values. We observed diameter selective desorption of the SWCNTs from the gel, in which the larger diameter species

were more easily eluted as the pH decreased. This diameter selectivity was similar to that found in usual SDS systems, but the pH required for elution of the SWCNTs was different. Moreover, we found that the residual metallic SWCNTs could be completely removed under the proper pH condition. Finally, we demonstrated that further purification of high-purity single-chirality SWCNTs is possible based on these findings.

3.2 Method

We investigated the effect of pH on chirality separation using a pH-controlled aqueous solution containing mixed surfactants. **Figure 3.1** shows a schematic diagram of the method for preparing the pH-treated solution. First, we prepared two bottles of aqueous solution (pH ~8.8) containing 0.5% SDS (Sigma-Aldrich) and 0.5% SC (Sigma-Aldrich), and conducted bubbling CO_2 gas into one of the bottles (**Figure 3.1**(a)). As a result, the pH of the CO_2-treated solution decreased to ~6. Then, by mixing these two solutions precisely, we prepared a solution that varied in 0.1 decrements from pH 8.4 to 7.6 [**Figure**

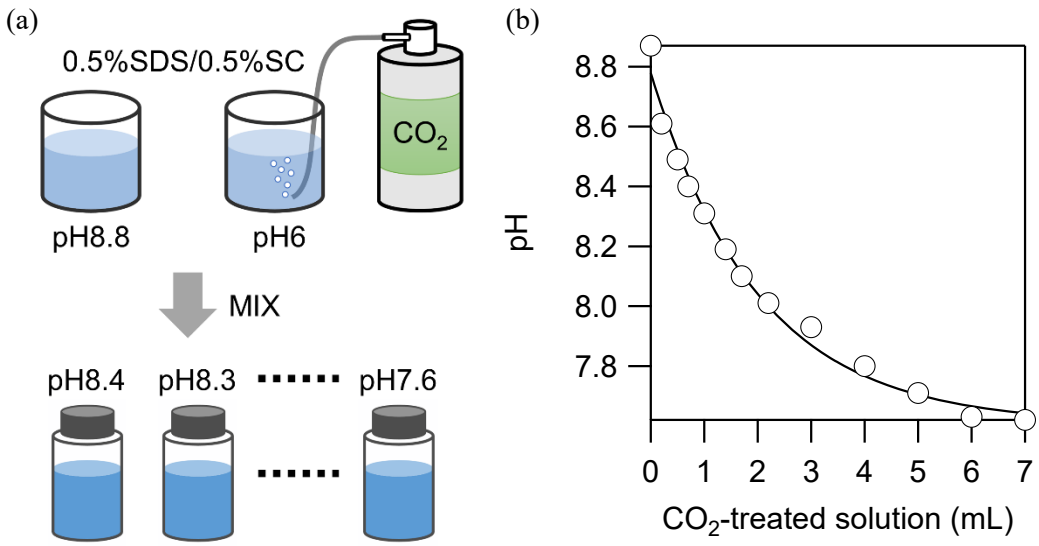

Figure 3.1. Preparation of pH-treated solutions. (a) Illustration of bubbling CO_2. (b) Changes in pH of mixed surfactant solution as a function of the added amount of CO_2 treated solutions. The change was investigated by pouring the selected amount of CO_2-treated solution of SDS and SC (pH: 6.55) into bottles filled with 20 mL of an untreated solution of SDS and SC (pH: 8.87). The solid black line is a fitted curve using an exponential function. Reprinted with permission from Y. Ichinose et al., J. Phys. Chem. C 121, 13391 (2017). Copyright 2017 American Chemical Society.

3.1(b)]. Finally, after measuring the pH using a pH meter (±0.02 pH accuracy, S2K922, IFSETCOM Co., Ltd.), the bottle was refilled with nitrogen to avoid subsequent pH changes during the experiment.

For separation, CoMoCAT (0.8 nm in diameter, Sigma-Aldrich) and HiPco SWCNTs (1.0 ± 0.3 nm in diameter, Unidym) were dispersed in an aqueous solution containing 0.5% SDS and 0.5% SC, using sonication followed by ultracentrifugation. **Figure 3.2** depicts the gel separation process with the pH-controlled solution. The dispersion was loaded into a column filled with gel beads (Sephacryl S-200 HR, GE Healthcare). After eluting the unbound metallic SWCNTs, the adsorbed semiconducting SWCNTs were eluted and collected after a stepwise decrease in pH from 8.4 to 7.6 in decrements of 0.1.

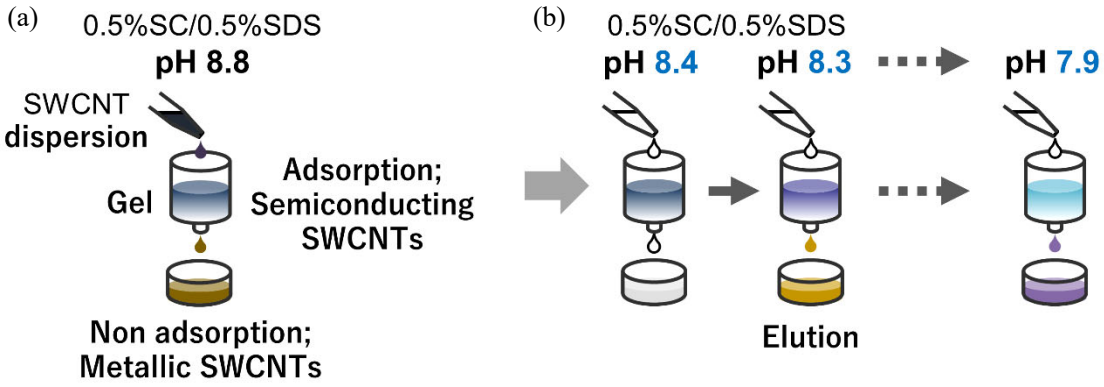

Figure 3.2. Gel chromatography separation with the pH-controlled solution. (a) Adsorption process for separating semiconducting and metallic SWCNTs. Semiconducting SWCNTs adsorb to the gel in the solution containing 0.5% SC and 0.5% SDS at pH 8.8; on the other hand, metallic SWCNTs pass through the gel. (b) Step-wise separation process. Gradually increase the pH of the solution poured into the gel in 0.1 increments and collect the respective eluates.

3.3 Results and Discussion

3.3.1 Diameter-selective separation of SWCNTs by precise pH control

Figure 3.3(a) and (b) show the optical absorption spectra of the eluted SWCNTs at different pH values using the HiPco and CoMoCAT SWCNTs, respectively. The species with the longer absorption wavelengths were eluted first. SWCNTs with larger diameters have longer absorption wavelengths [73]. Thus, both results show that the large-diameter SWCNTs were eluted earlier than the small-diameter ones. This trend was clearly observed in the HiPco SWCNT sample, which contained many (*n,m*) species with a wide

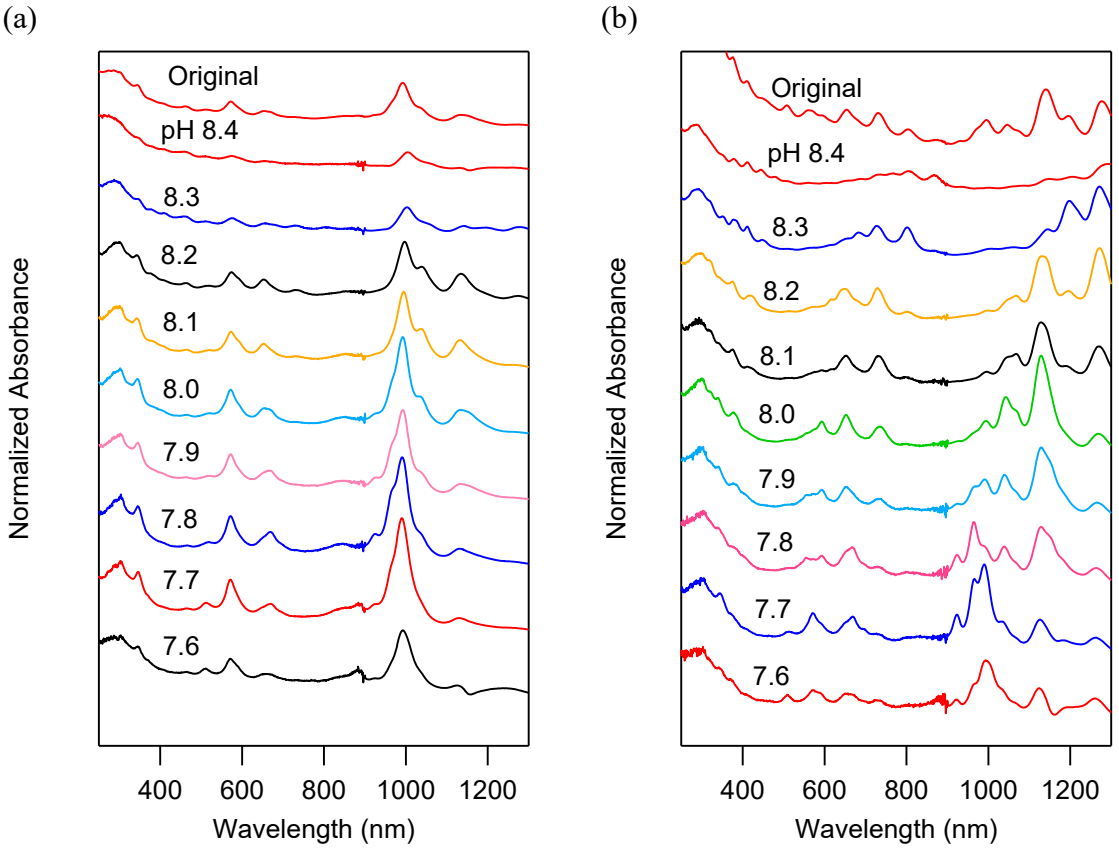

Figure 3.3. Diameter-selective separation of SWCNTs by precise pH control. (a, b) Optical absorption spectra of the eluted SWCNTs at different pH values. CoMoCAT (a) and HiPco SWCNTs (b) were used as the original starting materials, as shown in the respective top columns. These spectra corresponded to a pH range of 8.4 to 7.6 in decrements of 0.1 in order from the top to the bottom. Reprinted with permission from Y. Ichinose et al., J. Phys. Chem. C 121, 13391 (2017). Copyright 2017 American Chemical Society.

range of diameters. This diameter-selective elution was similar to the previous study using a single surfactant system of SDS [144]. In contrast, the pH required for eluting the SWCNTs was higher in the SDS/SC system than in the SDS single system, in which nearly all of the SWCNTs were eluted at a pH of approximately 3−4 [141,144]. This observation indicates that the SC influenced the SWCNTs and/or micelle structure around

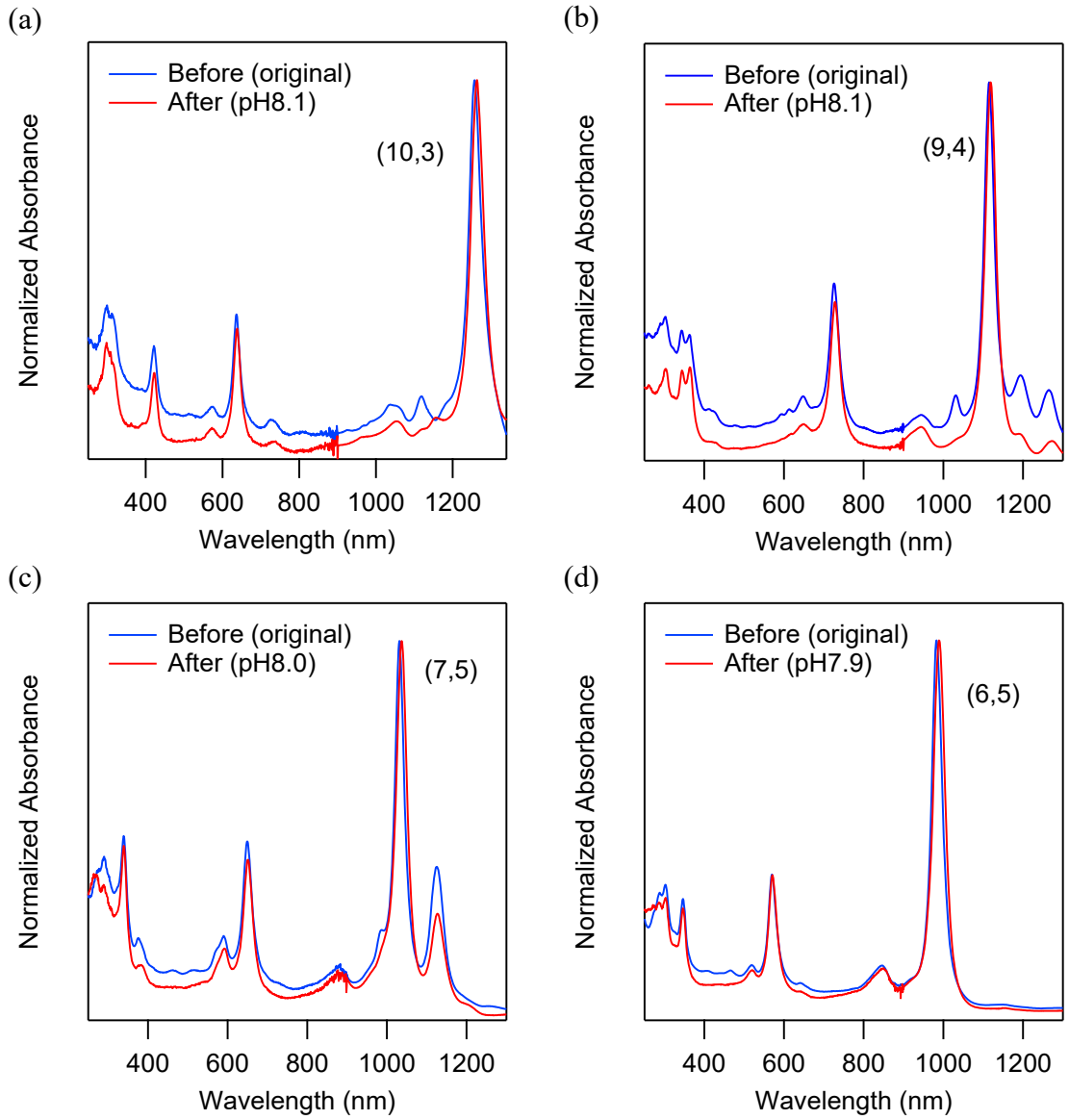

Figure 3.4. Purification of the chirality-enriched SWCNTs by precise pH control. (a−d) Optical absorption spectra of the single-chirality (*n*,*m*) species, including (a) (10,3), (b) (9,4), (c) (7,5), and (d) (6,5), before and after the pH-controlled elution. These spectra were normalized by their S_{11} intensities. Reprinted with permission from Y. Ichinose et al., J. Phys. Chem. C 121, 13391 (2017). Copyright 2017 American Chemical Society.

the SWCNTs, resulting in a change in the sensitivity to pH. The detailed pH dependence of the eluted (*n,m*) species is discussed later.

3.3.2 Purification of chirality-enriched SWCNTs by precise pH control

The pH-controlled diameter-selective elution of SWCNTs enables further purification of chirality-enriched SWCNTs. In this study, we applied this method to purify four (*n,m*) species separated by the method reported previously [126], in which the SWCNTs were eluted with DOC (Kanto-Kagaku Co.). The nearly single-chirality (6,5) and (7,5) samples were obtained from CoMoCAT SWCNTs, while the (9,4) and (10,3) samples were obtained from HiPco SWCNTs. The details of the separation procedures for these chirality-enriched species are shown in Appendix A. To make these original samples adsorb to the gel again, we diluted the DOC concentration of the dispersion to half of the original using a solution containing SDS and SC [126]. After loading the dispersion into a gel, the adsorbed SWCNTs were eluted and collected by decreasing the pH in the same manner as the previous separation. **Figure 3.4** shows the optical absorption spectra of the purified SWCNTs compared to the original SWCNTs. Each spectrum of the purified SWCNTs shows sharp S_{11}, S_{22}, and S_{33} peaks (S_{ii} indicates the *i*th optical transition of the semiconducting type chirality of SWCNTs) due to the disappearance of other absorption peaks around the target (*n,m*) species after purification. This observation indicates that the purities of these (*n,m*) species were highly improved after the pH-controlled purification.

Figure 3.5 shows the detailed elution profiles, revealing that the diameter selection played an important role during purification in this experiment, which was especially noted in the (7,5) and (9,4) samples that originally contained several (*n,m*) species. For instance, the purification of the (7,5) and (9,4) samples exhibited gradual changes in the eluted species from large-diameter species to small-diameter species at pH 8.1−8.0 and pH 8.2−8.1, respectively. In contrast, the (6,5) sample, which was originally high purity, did not exhibit changes in the S_{11} absorption but did exhibit changes in the residual metallic SWCNT adsorption at approximately 400−500 nm [see **Figure 3.4**(d)]. The detailed analysis regarding the residual metallic SWCNTs is discussed later.

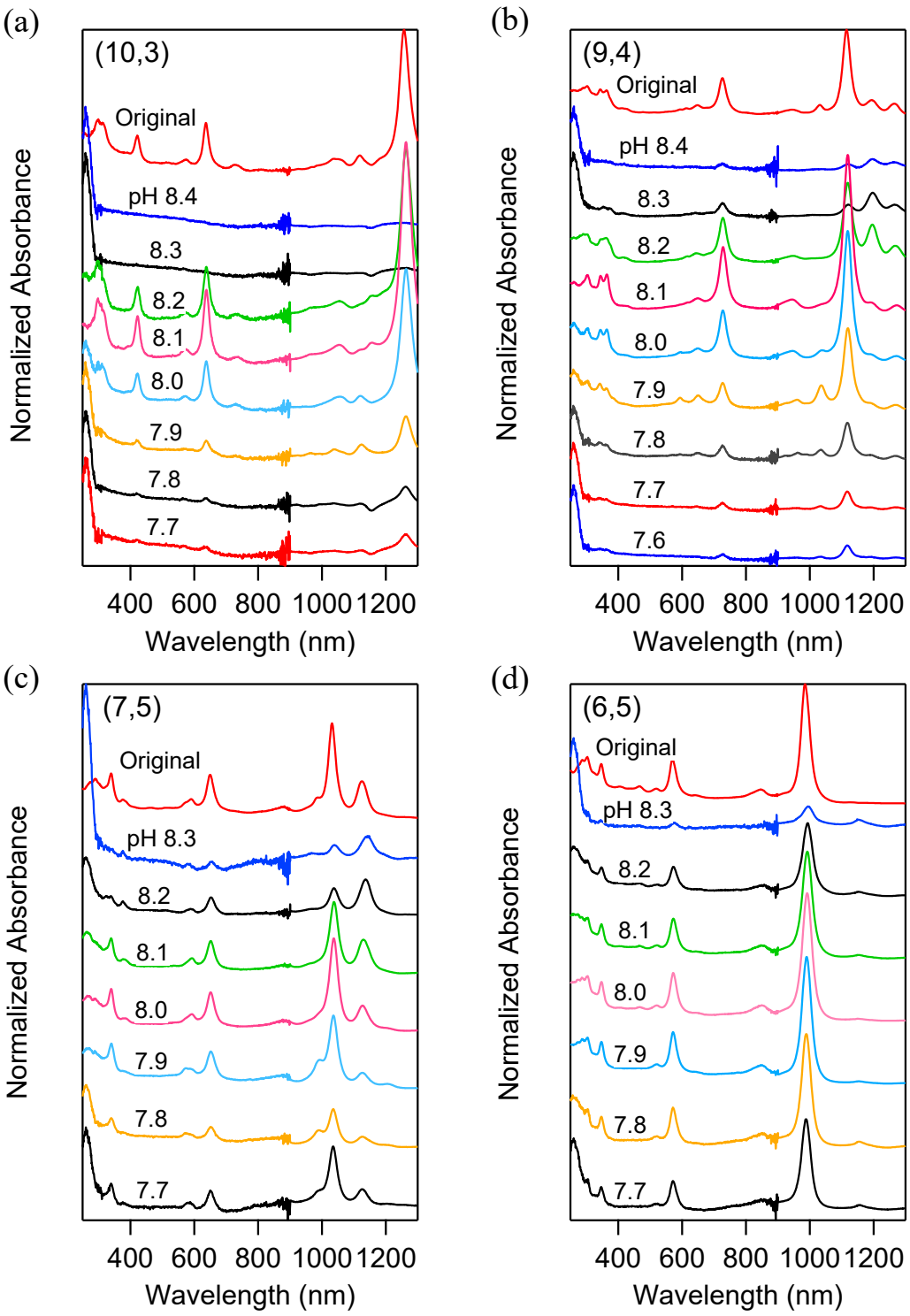

Figure 3.5. Purification process of the four chirality-enriched SWCNTs. Optical absorbance spectra of (a) (10,3), (b) (9,4), (c) (7,5), and (d) (6,5). The top spectra of all graphs show the samples before the pH-treated purification. Adapted with permission from Y. Ichinose et al., J. Phys. Chem. C 121, 13391 (2017). Copyright 2017 American Chemical Society.

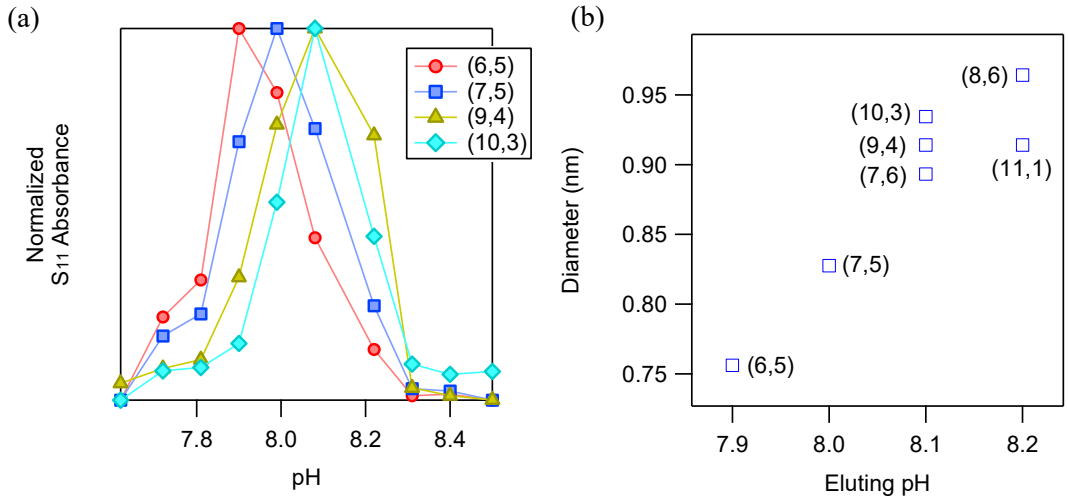

Figure 3.6. Diameter selectivity of pH in the mixed surfactant solution. (a) Relationship between the eluted (n,m) species and the pH of the eluent. The plot shows S_{11} peak intensities of the eluted (6,5) (red), (7,5) (blue), (9,4) (yellow), and (10,3) species (light blue) as a function of the eluent pH. The plots in each chirality are normalized at their maximum intensity. (b) Relationship between the diameters of the respective chiralities and the pH required for their elution. Adapted with permission from Y. Ichinose et al., J. Phys. Chem. C 121, 13391 (2017). Copyright 2017 American Chemical Society.

The diameter dependence affected the target species elution under suitable pH conditions. **Figure 3.6** shows a correlation between the diameter of SWCNTs and the pH at which they elute. According to the S_{11} peak intensity of the target (*n,m*) species plotted as a function of the eluent pH in **Figure 3.6**(a), the different samples were eluted at slightly different pH values: approximately 8.1 for (9,4) and (10,3), 8.0 for (7,5), and 7.9 for (6,5). **Figure 3.6**(b) shows the relation between the diameters of the respective chiralities and the pH required for their elution. Here, we chose only the chiralities that could be identified clearly in their absorption spectra. These results clearly exhibited the linear relation between the diameters of the eluted SWCNTs and pH, which are the same as the results using pristine HiPco and CoMoCAT SWCNTs (**Figure 3.3**).

3.3.3 Removal of residual metallic SWCNTs by precise pH control

To investigate the detailed effects of pH-controlled purification on the removal of residual metallic SWCNTs, we analyzed the absorption spectra at approximately 400−500 nm, which were assigned to M_{11} of the CoMoCAT metallic SWCNTs. **Figure 3.7**(a)

shows the results of the (6,5) sample. The spectra of the original (6,5) sample exhibited an S_{22} peak at 570 nm and the M_{11} peaks of residual metallic SWCNTs. The peaks at 400 and 470 nm were assigned to (5,5) and (7,4), respectively. We found that these residual metallic SWCNTs were completely missing at pH values less than 7.9. **Figure 3.7**(b) shows the S_{11} peak intensity (6,5) and the content rate of the metallic SWCNTs. The content rate was estimated as the ratio of the M_{11} peak intensity (470 nm) to the S_{11} peak intensity of (6,5). The metallic SWCNTs were eluted before elution of (6,5) SWCNTs, and then the ratio of (6,5) increased. As a result, we could obtain high-purity single-chirality (6,5) SWCNTs by collecting the eluted sample at pH values less than 7.8. This pH control was also effective during the adsorption process. We confirmed that the (6,5) SWCNTs could only be adsorbed without adsorption of the residual metallic SWCNTs by applying the pH-controlled sample onto the gel.

It is known that a decrease of pH induces oxidation of nanotubes, making them p-type and the positively charged state of the nanotube affects the adsorption of surfactants surrounding nanotubes [141,145,146]. For example, SDS, an anionic surfactant, is more attracted to positively charged nanotubes. The presence of a large amount of SDS on the surface of nanotubes reduces the adsorption of the nanotubes to the gel. The SWCNTs with a smaller bandgap tend to be more easily oxidized than the nanotubes with a larger bandgap [147,148]. Therefore, metallic SWCNTs tend to be more influenced by pH than semiconducting SWCNTs, and the semiconducting SWCNTs with larger diameters are more influenced than the nanotubes with smaller diameters. In this study, similar behavior is observed. A decrease in pH easily elutes the metallic SWCNTs and the semiconducting SWCNTs with large diameters than the semiconducting SWCNTs with small diameters [see **Figure 3.6**].

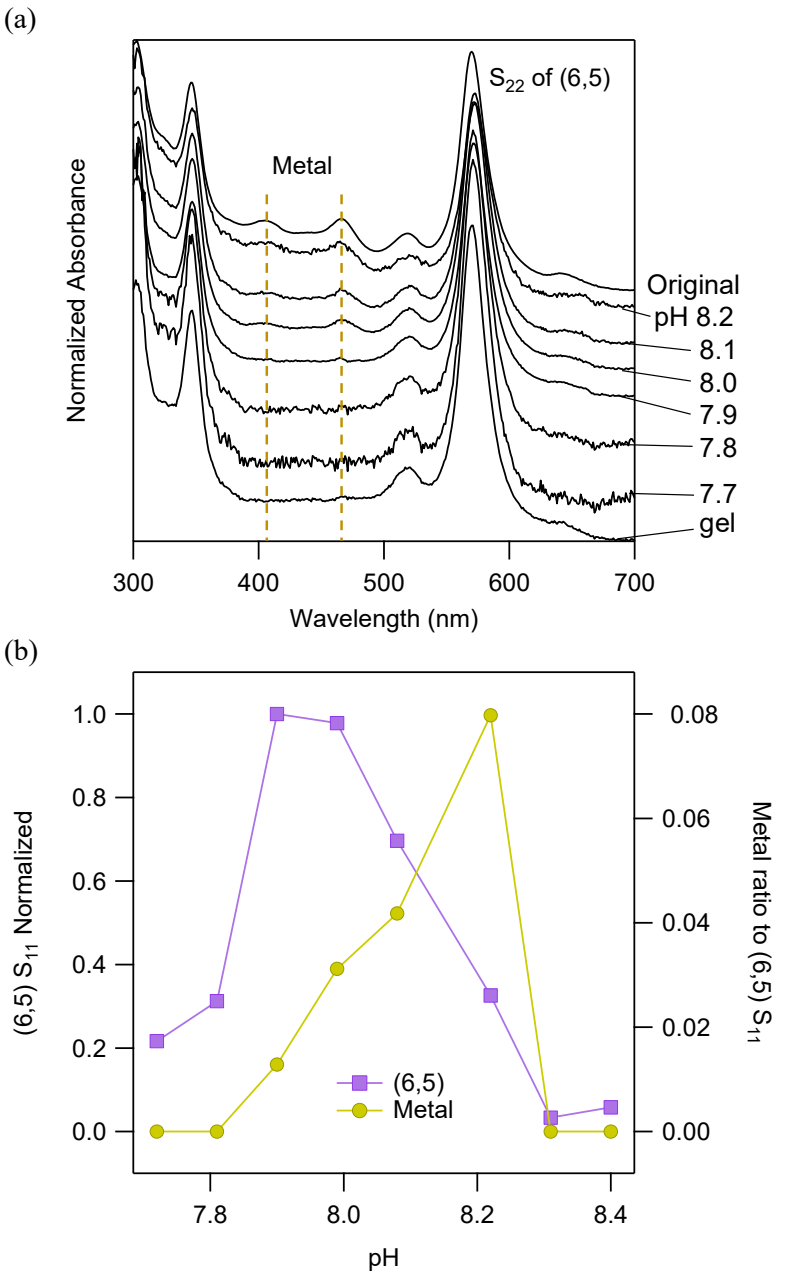

Figure 3.7. Removal of the residual metallic SWCNTs by precise pH control. (a) Optical absorption spectra of the eluted SWCNTs of (6,5) at different pH values in the SDS/SC system. These spectra were normalized at 280 nm, vertically shifted and focused at 300−700 nm for comparison. The top spectrum is the original sample before the purification procedure. From the second top to the second bottom, the elution spectra are at pH 8.2 to 7.7. The bottom spectrum is the component that was adsorbed to the gel after pouring the solution with pH 7.7. (b) Relationship between the S_{11} peak intensity of (6,5) and pH, and the content ratio of the metallic SWCNTs. Adapted with permission from Y. Ichinose et al., J. Phys. Chem. C 121, 13391 (2017). Copyright 2017 American Chemical Society.

3.3.4 Evaluation of the purity of purified (6,5)

Figure 3.8(a) shows the optical absorption spectra of the high-purity (6,5) SWCNTs obtained after pH-controlled purification. Since the M_{11} peaks at 400 and 470 nm completely disappeared after purification, the purity of the semiconducting SWCNTs was thought to be very high. The purity of the single-chirality SWCNTs was evaluated by fitting the absorption spectrum to simulated peaks of the individual (*n,m*) species with linear baseline absorption, and the ratio of the area of the dominant absorption peak to the sum of all peak areas was estimated. **Figure 3.8**(b) shows the results of the peak fitting for the high-purity (6,5) SWCNTs in the range of 800−1100 nm. Since the metallic type has been completely removed, only the semiconducting type needs to be considered in the purity evaluation. Since CoMoCAT, the raw material for (6,5), contains only semiconducting types close to the diameter of (6,5), the absorption peaks of other semiconducting chiralities, if they appear, should be close to those of (6,5). Therefore, the purity evaluation was done in the range of 800−1100 nm. There were two recognizable peaks, except for the (6,5) SWCNTs: a peak corresponding to the phonon sideband of (6,5) at approximately 850 nm and a small peak corresponding to (9,1) at approximately 910 nm. The absorbance data did not allow for a quantitative evaluation of the purity beyond 99%; however, judging from the content of the other species, such as (9,1), being less than 1%, the purity of the single-chirality (6,5) SWCNTs was estimated be more than 99%.

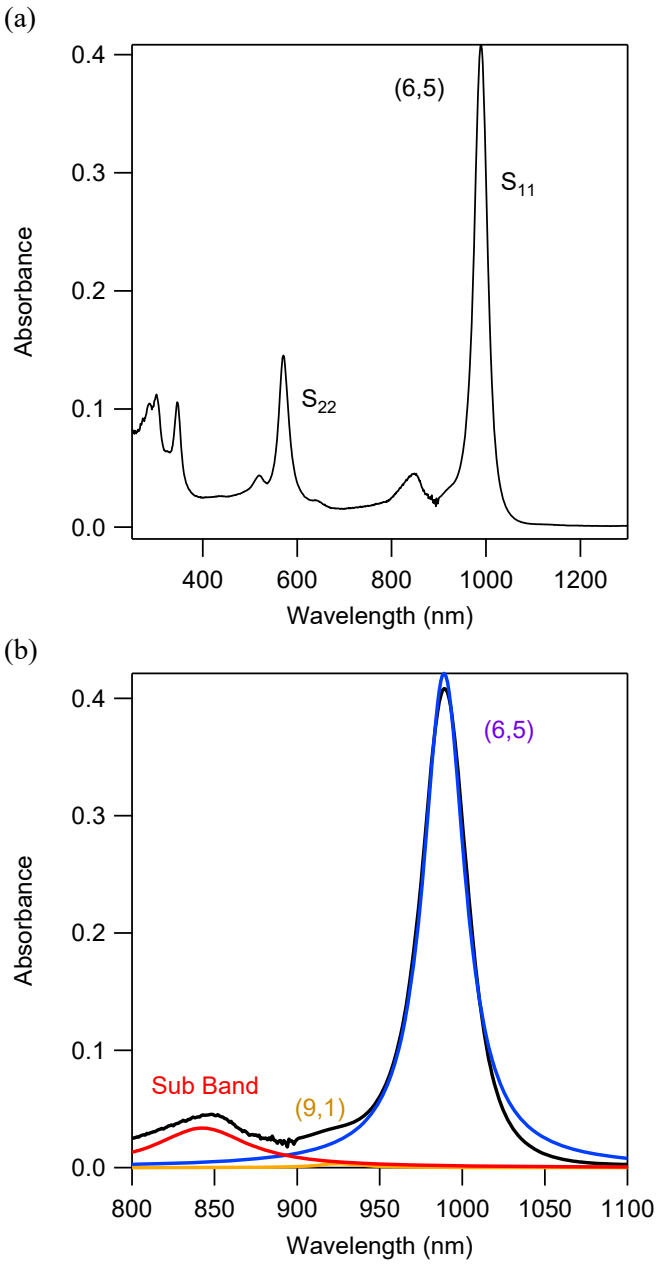

Figure 3.8. Evaluation of the purity of (6,5). (a) Optical absorption spectrum of the (6,5) SWCNTs. (b) Evaluation of the purity of the single-chirality (6,5) SWCNTs by fitting the absorption spectrum. Adapted with permission from Y. Ichinose et al., J. Phys. Chem. C 121, 13391 (2017). Copyright 2017 American Chemical Society.

To ensure a more reliable purity assessment, we also measured the high-purity (6,5) SWCNTs by transmission electron microscope (TEM) (JEM 2010F electron microscope with a CEOS spherical aberration corrector operated at 120 keV). **Figure 3.9**(a) shows the TEM image of SWCNTs. We captured 16 samples of SWCNTs that could be identified on the same TEM grid, and analyzed their diameters. **Figure 3.9**(b) shows the diameters of the captured SWCNTs. Because of the presence of contamination of gel and surfactants, there were relatively large error bars (~10%) in the evaluations. The black horizontal line indicates the theoretically estimated diameter (~0.745 nm) of (6,5) SWCNTs. The diameters of all the 16 nanotubes matched that of the (6,5) nanotubes within the accuracy of the error bars. Moreover, we observed the electron diffraction pattern of a bundle of the purified (6,5) SWCNTs sample using TEM, as shown in **Figure 3.10**(a). **Figure 3.10**(b) demonstrates the analyses results of the diffraction pattern. According to a report by Qin [149], the chiral index (*n,m*) can be determined as follows,

$$\frac{m}{n} = \frac{2D_2 - D_1}{2D_1 - D_2}.$$

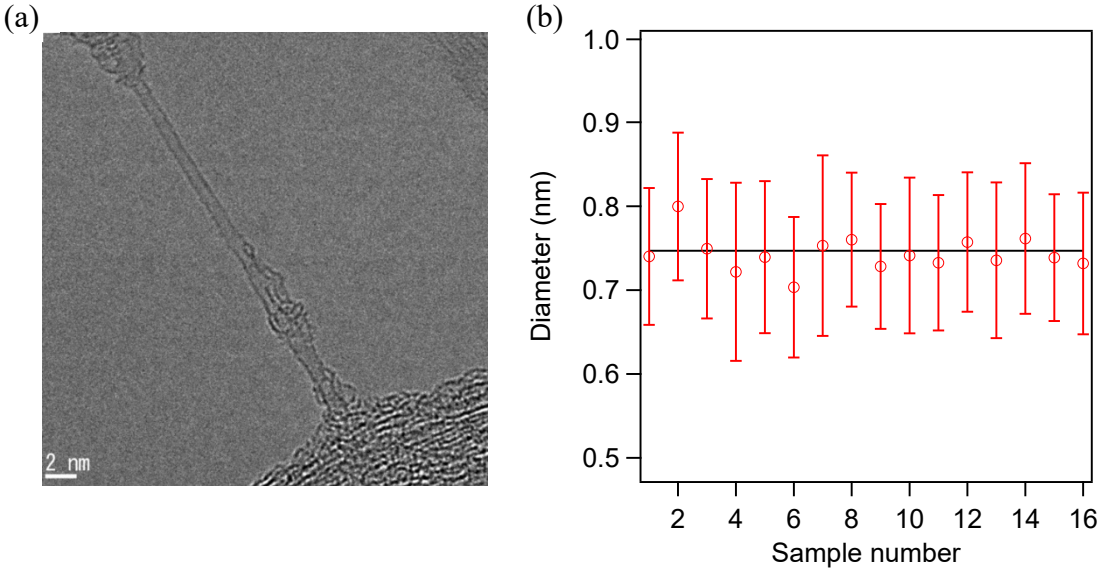

Figure 3.9. TEM observation to confirm the diameters of the purified (6,5) SWCNTs. (a) A typical TEM image of a rope of SWCNT. (b) The diameters of 16 samples purified (6,5) SWCNTs evaluated from the TEM images. Reprinted with permission from Y. Ichinose et al., J. Phys. Chem. C 121, 13391 (2017). Copyright 2017 American Chemical Society.

Therefore, we evaluated the m/n value to be about 0.82 from the observed diffraction pattern. **Figure 3.10**(c-f) show the simulation patterns of electron diffractions in (*n,m*) chiralities. The experimental value was consistent with the simulation pattern of electron diffractions in (6,5) SWCNTs. Although the expected m/n values of (5,4) and (7,6) SWCNTs were also similar to the observed value, the diffraction pattern did not match the experimental pattern in **Figure 3.10**(a-b). On the other hand, (9,1) SWCNTs have almost the same diameter as (6,5) SWCNTs; however, the simulated m/n ratio is

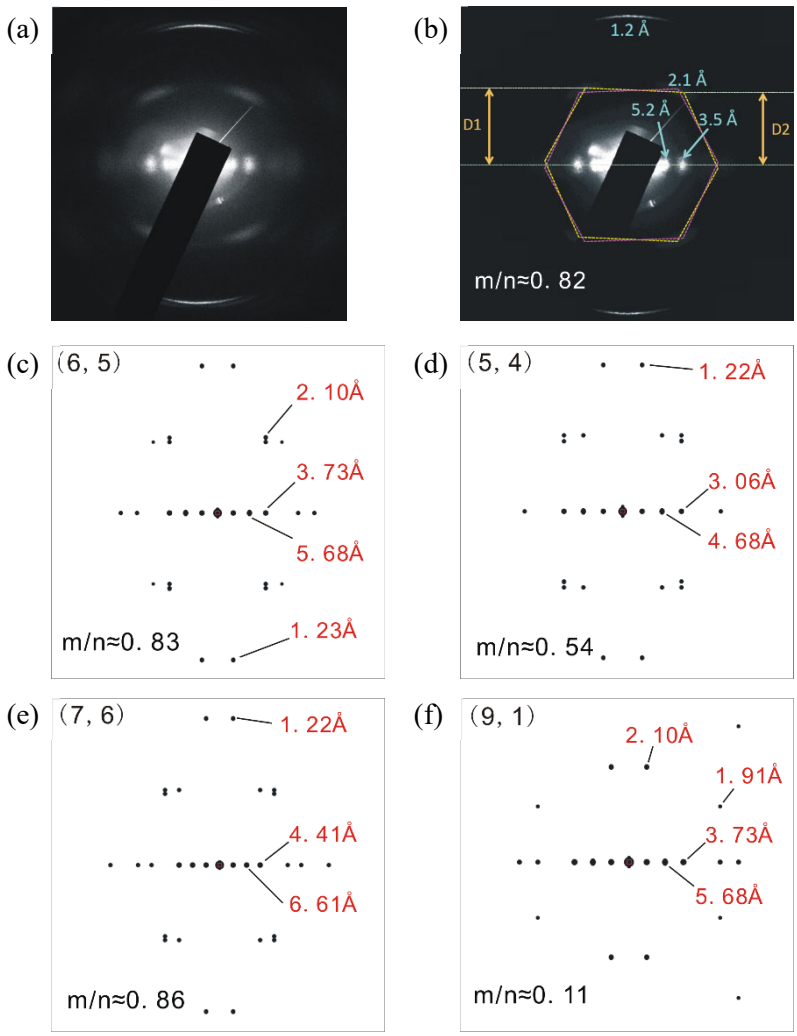

Figure 3.10. The electron diffraction pattern of SWCNTs. (a) The raw image of the diffraction pattern taken from a bundle of the purified (6,5) sample. (b) Analysis result of the diffraction pattern. (c-f) Simulation pattern of (c) (6,5), (d) (5,4), (e) (7,6), and (f) (9,1). Adapted with permission from Y. Ichinose et al., J. Phys. Chem. C 121, 13391 (2017). Copyright 2017 American Chemical Society.

different from 0.82. Therefore, according to the calculated m/n values and diffraction patterns, we concluded that the observed diffraction pattern is (6,5) SWCNTs.

The purity was almost the same as that of (6,5) SWCNTs obtained by the state-of art of DNA purification techniques [132]. Moreover, this purity was estimated for the situation in which the metallic SWCNTs were absent. Therefore, we believe that this sample has better or comparable quality compared to those from other studies [88,113,130,132,133,150].

3.4 Conclusions

We revealed the effect of pH on gel chromatography using mixed surfactant systems and applied the obtained knowledge to further purify single-chirality SWCNTs. The pH of the solution containing SDS and SC was precisely controlled in a range from 8.4 to 7.6 with an accuracy of approximately 0.1 by mixing the solution (pH ~6) treated with CO_2 bubbling with an untreated solution (pH ~9). By applying this eluent with a series of different pH values to the gel with adsorbed SWCNTs, we observed diameter-selective desorption of the SWCNTs from the gel, in which the larger-diameter species were easily eluted as the pH decreased. This diameter selectivity was useful for the subsequent purification of four nearly single-chirality (*n,m*) species, including (6,5), (7,5), (9,4), and (10,3). Moreover, we found the metallic SWCNTs were eluted before elution of the semiconducting SWCNTs, and hence, we could obtain high-purity semiconducting single-chirality (6,5) SWCNTs by collecting the eluted sample at the proper pH. Finally, on the basis of these findings, the purity of the purified single-chirality (6,5) samples reached more than 99% without residual metallic SWCNTs. We believe that these high-purity single-chirality SWCNTs will enable high-performance semiconductor applications, such as in field-effect transistors [151] and thermoelectric devices [98].

Chapter 4

Solving the Thermoelectric Trade-Off Problem with One-Dimensional Electronic Structure of Metallic SWCNTs

Semiconductors are generally considered far superior to metals as thermoelectric materials because of their much larger Seebeck coefficients, S. However, a maximum value of S in a semiconductor is normally accompanied by a minuscule electrical conductivity, σ, and hence, the thermoelectric power factor ($P = S^2\sigma$) remains small. An attempt to increase σ by increasing the chemical potential, μ, on the other hand, decreases S. This trade-off between S and σ is a well-known dilemma in developing high-performance thermoelectric devices based on semiconductors. Here, we show that the use of metallic carbon nanotubes (CNTs) with tunable μ solves this long-standing problem, demonstrating a higher thermoelectric performance than semiconducting CNTs. We studied the μ dependence of S, σ, and P in a series of CNT films with systematically varied metallic CNT contents. In purely metallic CNT films, both S and σ monotonically increased with μ, continuously boosting P while increasing μ. Particularly, in an aligned metallic CNT film, the maximum of P was ~5 times larger than that in the highest-purity (>99%) single-chirality semiconducting CNT film. We attribute these superior thermoelectric properties of metallic CNTs to the simultaneously enhanced S and σ of one-dimensional conduction electrons near the first van Hove singularity.

4.1 Introduction

There is an increasing recognition that efficient conversion of waste heat to electrical power is key to the successful development of wearable electronics and photonics. Much recent attention has been paid to nanostructured semiconductor materials, including semiconducting polymers and carbon nanotubes (CNTs), for the development of wearable

thermoelectric devices because of their flexibility and scalability in addition to their expected superb thermoelectric properties [4]. Semiconductors have always been preferred for thermoelectric device applications, and little attention has been paid to metals because of their typically small Seebeck coefficient, S [152,153].

A maximum S in a semiconductor is achieved when the chemical potential, μ, is shifted from the middle of the band gap, or the charge neutrality point (CNP), by an

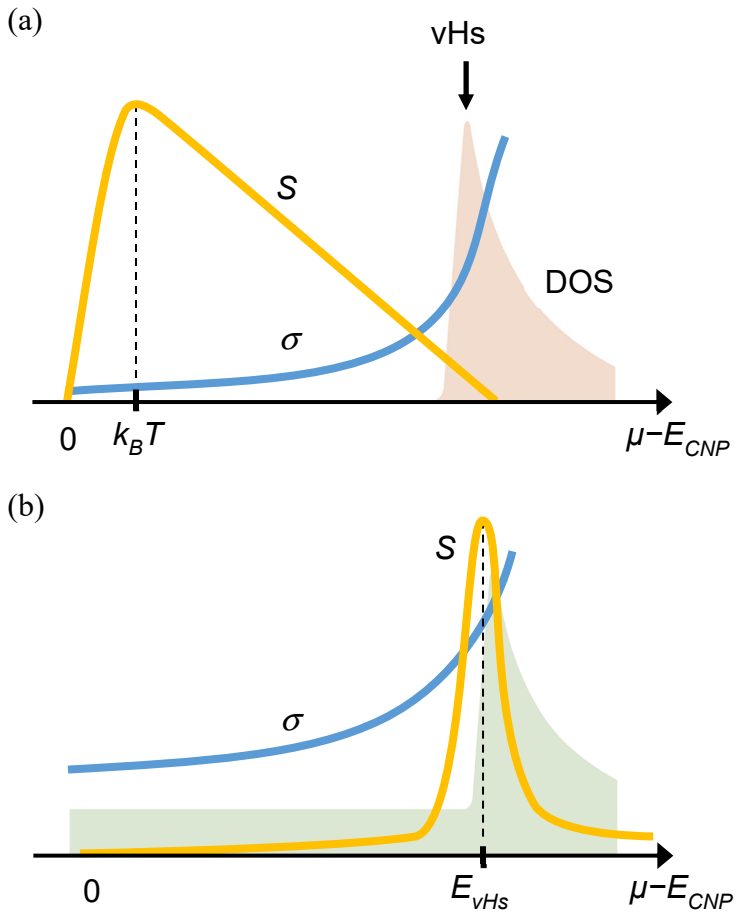

Figure 4.1. Mechanism of how a chemical-potential-tuned metallic carbon nanotube can outperform a semiconducting nanotube as a thermoelectric material. The expected behaviors of the Seebeck coefficient and electrical conductivity of (a) semiconducting and (b) metallic carbon nanotubes as a function of chemical potential measured from the charge neutrality point (E_{CNP}). Note that the thermoelectric power factor is $P = S^2\sigma$, so a high power factor requires simultaneously large the Seebeck coefficient and electrical conductivity, which is possible only in metallic nanotubes. Adapted with permission from Y. Ichinose et al., Nano letters 19, 7370 (2019). Copyright 2019 American Chemical Society.

amount on the order of the thermal energy $k_{\mathrm{B}}T$. However, at this value of μ, the carrier density, and hence electrical conductivity, σ, is very small [see **Figure 4.1**(a)]. When the μ is further moved away from the CNP gradually, increasing the carrier density either on the *p*- or *n*-side, σ tends to increase monotonically, but S tends to decrease monotonically. Therefore, the thermoelectric power factor $P = S^2\sigma$ continuously remains small as one varies the μ. This trade-off between S and σ is a well-known dilemma [14], preventing the development of high-performance thermoelectric devices.

A special case arises in certain 4*f*-electron metals, which have exhibited unusually large P values [34]. This can be explained as a result of the existence of a narrow 4*f*-electron peak in density of states (DOS) in the vicinity of μ, as, in general, the best thermoelectric is expected in materials that have a sharp singularity in DOS very close to μ [66]. CNTs can embody this scenario if μ can be precisely tuned to a one-dimensional (1D) van Hove singularity (vHs), as pointed out by Hicks and Dresselhaus [19]. Previous experiments have examined the thermoelectric properties of various types of single-walled CNT (SWCNT) samples [75,76,94,95,98,100-102,154]. Semiconducting SWCNTs have been shown to possess a large S [92-94,98,119,120,155]. In contrast, metallic SWCNTs have been largely disregarded in thermoelectric studies because of their typically small S under normal circumstances [95], and, in fact, a great deal of effort has been expended to remove small amounts of metallic SWCNTs from semiconductor-enriched SWCNT specimens because they degrade thermoelectric performance [112]. However, since metallic SWCNTs also possess vHs in DOS, one should observe thermoelectric enhancement if μ is moved far away from the CNP and tuned to coincide with a vHs, where the σ is also enhanced [see **Figure 4.1**(b)].

Here, we systematically investigated the μ dependence of S, σ, and P in a variety of films containing high-purity (>99%) single-chirality semiconducting SWCNTs, high-purity metallic SWCNTs, and their mixtures with different content ratios. In all samples, in which metallic nanotubes are present, we observed a nontraditional regime where both S and σ increased with μ. Correspondingly, S increased with σ in this regime. This novel regime was followed by a traditionally seen regime, in which S decreased with σ

in films consisting of both semiconducting and metallic SWCNTs. However, in purely metallic films, S monotonically increased with σ throughout the entire μ range we covered; namely, the thermoelectric trade-off problem has been solved by the use of purely metallic SWCNT films. Notably, the maximum value of P achieved in an aligned metallic SWCNT film, ~300 $\mu Wm^{-1}K^{-2}$, was five times larger than that obtained in the highest-purity single-chirality semiconducting SWCNT film.

4.2 Experiment

4.2.1 SWCNT film preparation

Table 4.1 summarizes the main five SWCNT samples we studied in this work (samples 1−5). We first prepared two highly purified SWCNT ensemble samples: samples 1 and 4 [see **Figure 4.2**(a)]. Sample 1 was enriched in (6,5) semiconducting SWCNTs, synthesized by the CoMoCAT method (SG65, Sigma-Aldrich), using gel chromatography with precise pH control with a chirality purity over 99% [156]. Details of this separation procedure can be found in Chapter 3. Sample 4 was enriched in metallic SWCNTs with an average diameter of 1.4 nm (metallic purity > 99%), synthesized by the arc-discharge method (Arc SO, Meijyo Nano Carbon Co.) and enriched by density gradient ultracentrifugation [86]. The SWCNT concentrations of samples 1 and 4 were adjusted so that the

Table 4.1. Five SWCNT Film Samples with varying Semiconductor−Metal Ratios [a]

Sample	(6,5) content (%)	Metallic content (%)	Synthesis and enrichment	Aligned?
1	>99	<1	CoMoCAT and GC	No
2	90	10	Mixture of 1 and 4	No
3	50	50	Mixture of 1 and 4	No
4	<1	>99	Arc discharge and DGU	No
5	<1	>96	Arc discharge and DGU	yes

[a] Note that (6,5) single-wall carbon nanotubes are semiconducting with a band gap of ~1 eV. Abbreviations: GC = gel chromatography; DGU = density gradient ultracentrifugation.

absorbance at the first vHs becomes the same level. Furthermore, by mixing samples 1 and 4 at certain ratios, we prepared sample 2, in which the (6,5)-to-metal ratio was 9:1, and sample 3, in which the (6,5)-to-metal ratio was 1:1. Absorbance spectra are shown in **Figure 4.2**(b) for samples 1 to 4.

Each sample was poured into the funnel of a vacuum filtration system and filtered through a PTFE membrane (Omnipore 0.2 μm PTFE Membrane, Merck Millipore Ltd.), and surfactants on SWCNTs such as sodium deoxycholate (DOC) or iodixanol were replaced by Triton (polyoxyethylene octylphenyl ether, Wako pure chemical Industries, Ltd.). Subsequently, the SWCNTs in the redispersed solution were filtered through a polycarbonate membrane filter (Whatman Nuclepore Track- Etched membrane 25 mm 0.2 μm) to form a thin film.

4.2.2 Aligned Metallic SWCNT Film (Sample 5) Preparation

We prepared a highly aligned metallic SWCNT film, sample 5, as follow [157,158]. Metallic SWCNTs were separated by density gradient ultracentrifugation in the same manner as sample 4. We then conducted ultrafiltration (Amicon Ultra-15 Centrifugal Filters Ultracel, 100 K, Merck Millipore Ltd.) on the resulting metallically enriched solution to exchange the solvent from DOC/iodixanol to 0.3% DOC. Subsequently, the obtained suspension was sonicated with a tip sonicator (XL-2000 Sonicator, Qsonica, 1/4 in. probe, ~30 W) for 5−10 mins and centrifuged for 15−20 mins at 38,000 rpm (Beckman-Coulter Optima L-80 XP Preparatory Ultracentrifuge (BSI414) using a Beckman SW-41 Ti swing bucket rotor). The upper 80% of the SWCNT suspension in the centrifuge tube was collected and then diluted with pure water to have a surfactant concentration of 0.013% DOC. The suspension was then poured into the funnel of a vacuum filtration system and slowly filtered through a polycarbonate membrane filter (Whatman Nuclepore Track-Etched membrane 25 mm 0.2 μm) under well-controlled conditions to form an aligned SWCNT film [see **Figure 4.2**(c)]. We identified the alignment direction and evaluated the alignment degree using polarized Raman measurements with a laser wavelength of 488 nm. The average $I_{\parallel}/I_{\perp}$, which is the ratio of the *G*-band peak intensity for parallel polarization to that for perpendicular polarization, for the sample was 2.6 ± 0.2, as in **Figure**

4.2(d).

4.2.3 Device preparation

To investigate the thermoelectric properties of these samples as a function of μ, we employed the methods of electrolyte gating described previously [98,99]. The prepared SWCNT thin film was transferred onto a polyimide/parylene substrate with predeposited gold electrodes (thickness ~100 nm). Residual polymers such as polycarbonate or poly-vinylpyrrolidone were dissolved and washed by chloroform and acetone. The length, width, and thickness of the film were respectively ~600 μm, ~1 mm, and ~80 nm. To

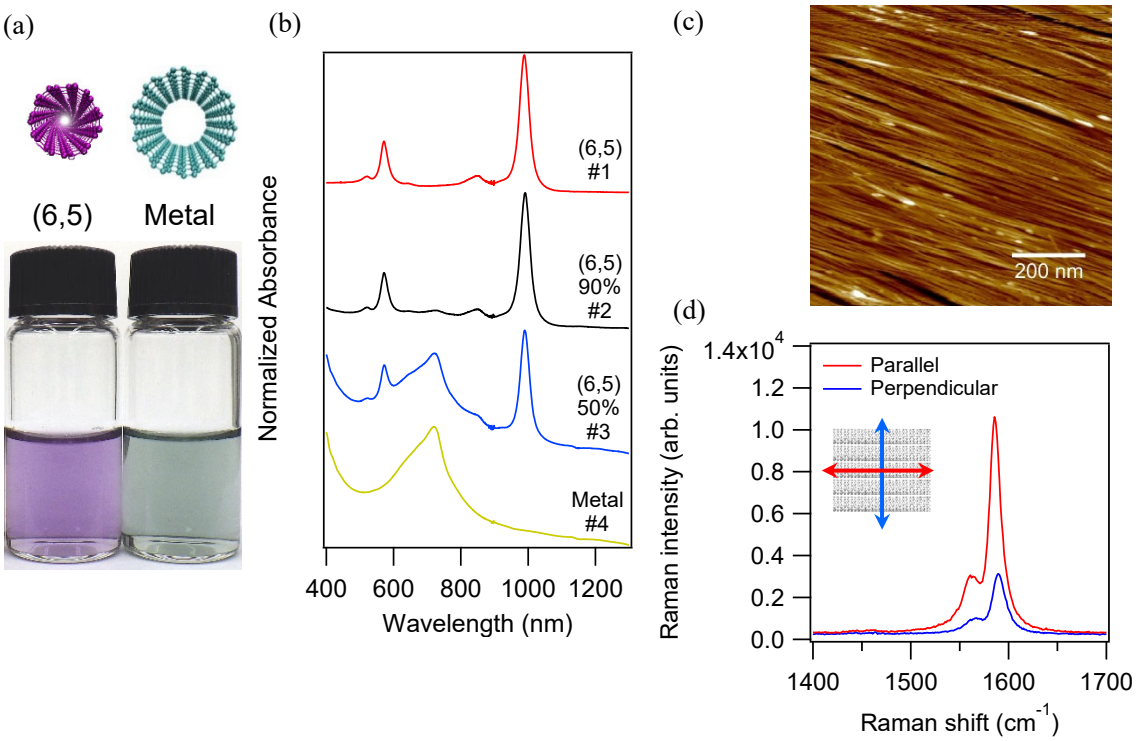

Figure 4.2. Sample information. (a) A picture of aqueous solutions of purified SWCNTs used for making thin films. They are enriched in (6,5) SWCNTs (left) and metallic SWCNTs (right), respectively. (b) Optical absorbance spectra for Samples 1-4. We systematically changed the (6,5)-metal ratio – #1: 100%-0%, #2: 90%-10%, #3: 50%-50%, and #4: 0%-100%. (c) A picture of an atomic force microscopy (MultiMode 8, Bruker Japan K.K.) image of an aligned metallic SWCNT film (Sample 5). (d) Raman spectra for sample 5 with excitation light polarized parallel (red line) and perpendicular (blue line) to the nanotube alignment axis. Adapted with permission from Y. Ichinose et al., Nano letters 19, 7370 (2019). Copyright 2019 American Chemical Society.

remove residual Triton and organic solvent, the sample was annealed at 200°C for 2 hours in a vacuum (< 10^{-3} Pa). A heater (KFR-02N-120-C1-11N10C2, Kyowa Dengyo Co.) was attached on one side of the film, and thermocouples (KFT(TW)-50-100-050, ANBE SMT Co.) were fixed on the electrodes at both film ends by silver paste (D-500 DOTITE, Fujikura Kasei Co.). To make sure that no chemical reaction occurs between silver and ionic liquid, insulating sealant (TSE397-C, Momentive Performance Materials Japan LLC.) covered the silver paste. Ionic liquid (TMPA-TFSI, Kanto Chemical Co.) was dropped to cover the SWCNT film and gate electrodes to create an electrolyte gating system. **Figure 4.3**(a) shows a schematic illustration of the experimental setup. We injected electrons and holes through electric double-layer formation, which was controlled by the gate voltage (V_G). The device pictures are schematically depicted in **Figure 4.3**(b-c).

4.2.4 Conductivity and Seebeck Coefficient Measurements

Electrical conductivity and Seebeck coefficient measurements were conducted in a vacuum (~10^{-3} Pa) using a vacuum- and low-temperature probe station (Grail 10, Nagase Techno Co.). By changing V_G from +3.2 V to −2.8 V, we injected electrons or holes into the SWCNT film, *i.e.*, shifting the μ. For the transport measurements, the source-drain voltage was kept as small as possible, such as 0.1 V for (6,5) and 5 mV for metallic SWCNTs, and then the transport properties were evaluated in the linear response region. σ was calculated from the measured resistance of the film at each gate voltage. S as a function of V_G was measured in the same manner as that described in ref. [98]. S were always measured in the same gate-shift direction, such as from positive to negative, in order to eliminate the influence of hysteresis during the measurements.

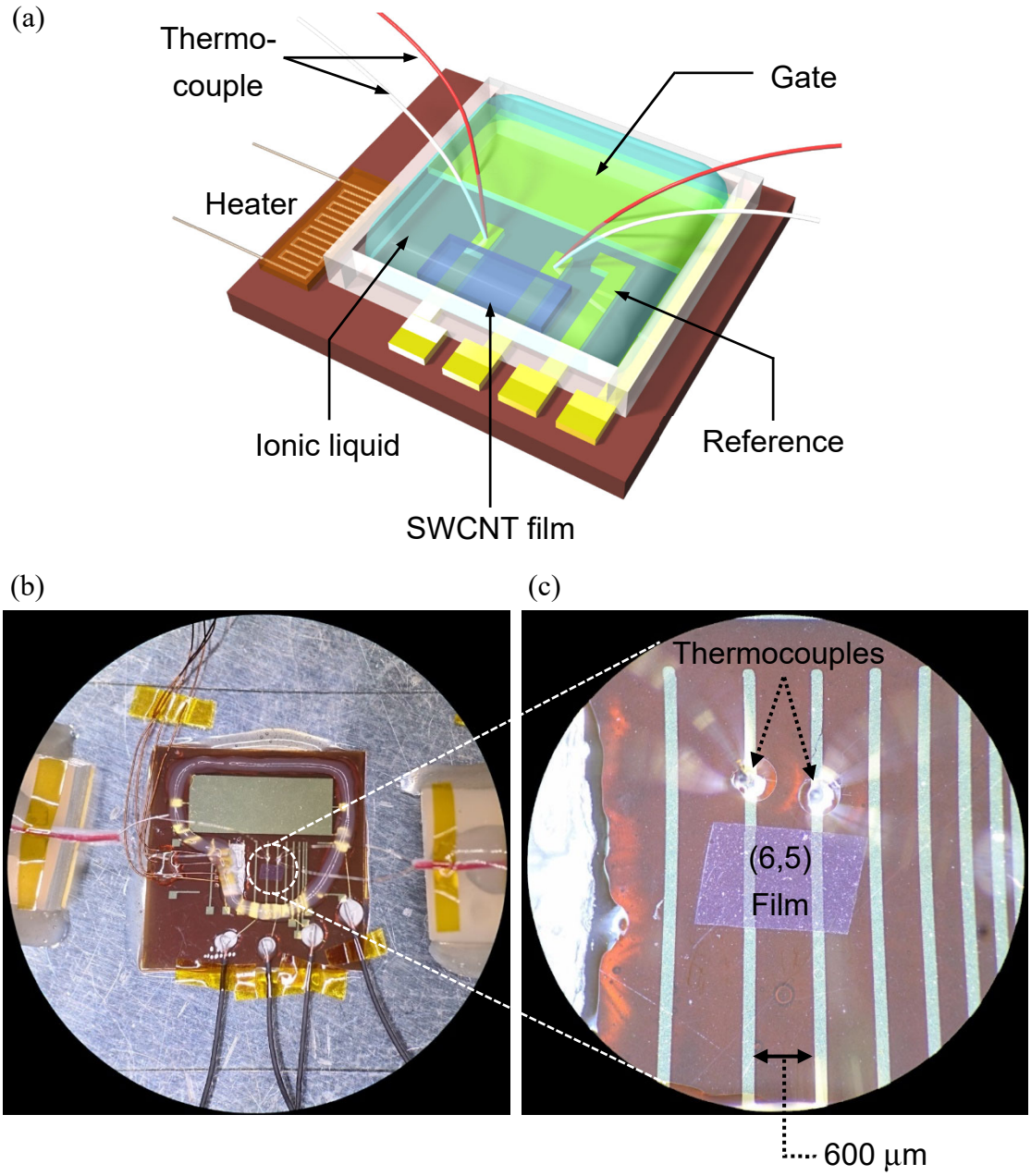

Figure 4.3. Device information. (a) Schematic diagram of the experimental setup used for measuring thermoelectric properties of carbon nanotube films using electrolyte gating. (b) A picture of the whole device. (b) A picture zoomed in on a (6,5) film. The temperature gradient and thermoelectric voltage was measured by thermocouples near both ends of the film. The distance between channels was 600 µm. Adapted with permission from Y. Ichinose et al., Nano letters 19, 7370 (2019). Copyright 2019 American Chemical Society.

4.3 Results

Figure 4.4 shows experimentally measured σ for samples 1−5 as a function of V_G. In all plots, the CNP is set to be at $V_G = 0$ V. All samples exhibited transistor behavior with on/off ratios varying from <10 (samples 4 and 5) to ~10^5 (sample 1). **Figure 4.5**(a) shows S versus V_G for the samples, where μ was tuned in a wide range, going from the *p*-type regime to the *n*-type regime. In sample 1, positive and negative peaks are observed slightly below and above the CNP, respectively, with a sudden change of sign of S at the CNP. This is a typical behavior for semiconductors, with the peak separation in energy given by $\sim k_B T$. The data for sample 2 in **Figure 4.5**(a) shows that inclusion of metallic SWCNTs, even at 10%, completely diminishes the peak of S near the CNP and significantly suppresses the value of S from 300 μVK^{-1} to 60 μVK^{-1}. At the same time, the overall line shapes of V_G dependence drastically changes. As the metal ratio further increases, the peak structure in the S−V_G curve tends to diminish (sample 3), and in the 100% metallic case (samples 4 and 5), no peak structure is observed.

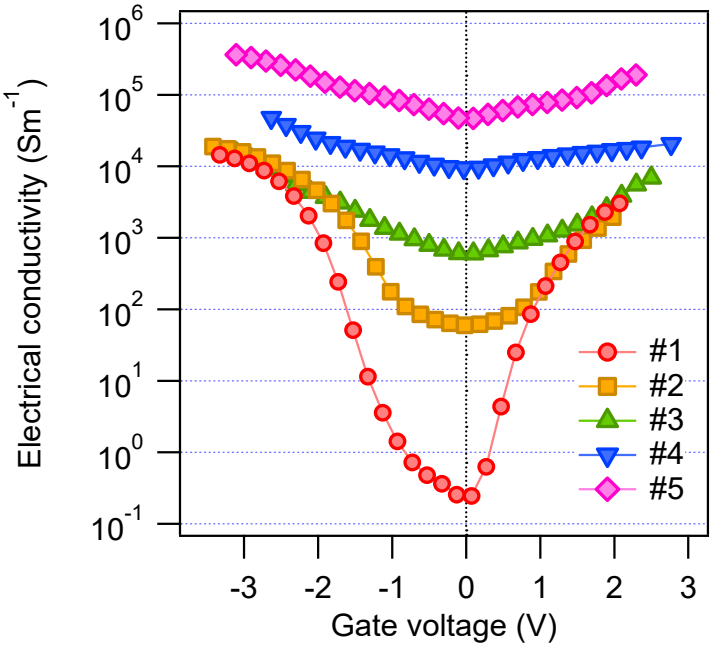

Figure 4.4. Electrical conductivity as a function of gate voltage for a series of samples with different semiconductor-metal ratios (#1: 100%-0%, red circles; # 2: 90%-10%, orange squares; #3: 50%-50%, green triangles; #4: 0%-100%, blue inverted triangles; #5: 0%-100%, pink diamonds). Adapted with permission from Y. Ichinose et al., Nano letters 19, 7370 (2019). Copyright 2019 American Chemical Society.

Figure 4.5(b) shows the corresponding V_G dependence of P, for the five samples, which exhibits peak structures. A peak in P is expected to appear when the μ coincides with the first vHs either in the valence or conduction band [98]. The sharpness of the power factor peak for sample 1 indicates that fine-tuning of V_G is necessary for achieving and maintaining a high P in a highly purified (6,5) SWCNT sample. When the

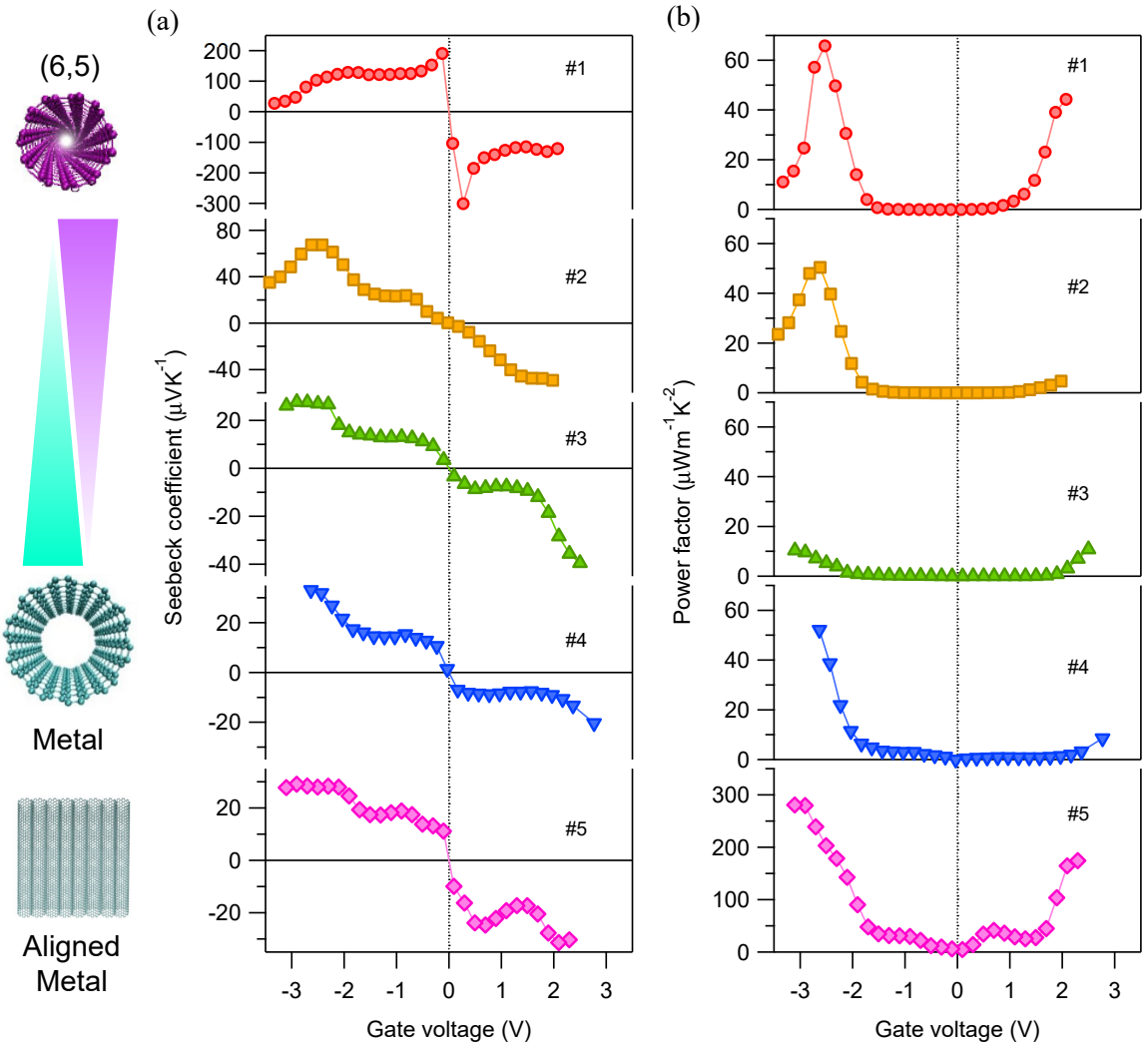

Figure 4.5. Gate-tuning the thermoelectric properties of semiconductor-enriched, type-mixed, and metal-enriched single-wall carbon nanotubes. (a) Seebeck coefficient, and (b) power factor as a function of gate voltage for a series of samples with different semiconductor-metal ratios (#1: 100%-0%, red circles; # 2: 90%-10%, orange squares; #3: 50%-50%, green triangles; #4: 0%-100%, blue inverted triangles; #5: 0%-100%, pink diamonds). See Table 4.1 for sample descriptions. Adapted with permission from Y. Ichinose et al., Nano letters 19, 7370 (2019). Copyright 2019 American Chemical Society.

chirality purity is higher, the peak power factor value is higher at the vHs, as demonstrated by the data for Samples 1, 2, and 3 in **Figure 4.5**(b). However, in sample 4 (>99% metallic) at a high $|V_G|$, such as when $V_G < -2$ V, it is seen that P continues to increase, reaching the value for the highest-purity semiconducting sample (sample 1). Finally, the peak P value of an aligned metallic film (sample 5) exceeds that of sample 1.

Figure 4.6(a) is a summary of the relationship between $|S|$ and σ for the five samples. This figure highlights the following three points: (1) In the metallically purified SWCNT samples (samples 4 and 5), S increases monotonically with σ, *i.e.*, the trade-off between them is fully eliminated. (2) As the content of semiconducting types increases (samples 2 and 3), the range where the trade-off is lifted becomes narrower and shifts toward a lower σ region, and a plateau region develops. (3) In the highest-purity semiconducting sample (sample 1), the unconventional regime is absent, *i.e.*, S decreases with increasing σ in the entire range.

In the highest conductivity region, $\sigma > 10^4$ Sm^{-1}, only the S of the purely metallic samples continues to increase as σ increases, while those of the other samples rapidly decrease with increasing σ. The same behavior is also seen in P, as shown in **Figure 4.6**(b). Sample 1 exhibits a peak at $\sigma \sim 6 \times 10^3$ Sm^{-1}, while samples 2 and 3 show the maximum values at $\sigma \sim 1 \times 10^4$ Sm^{-1}. Samples 4 and 5 show a continuous increase of P with σ up to the highest value of σ. The highest value of P of sample 4 (achieved at the highest σ) is essentially equal to that of sample 1 (achieved at $\sigma \sim 6 \times 10^3$ Sm^{-1}) within the experimental error. Sample 5 exhibits an even higher P than sample 4, as expected from the fact that alignment leads to an enhanced σ [157], while S remains constant [106]. The highest value of P of sample 5 is ~300 $\mu W m^{-1} K^{-2}$, which is the highest among all the samples studied in this work. That is, the aligned and metallically enriched SWCNT film outperforms the highest-purity semiconducting SCWNT film in terms of thermoelectric power factor.

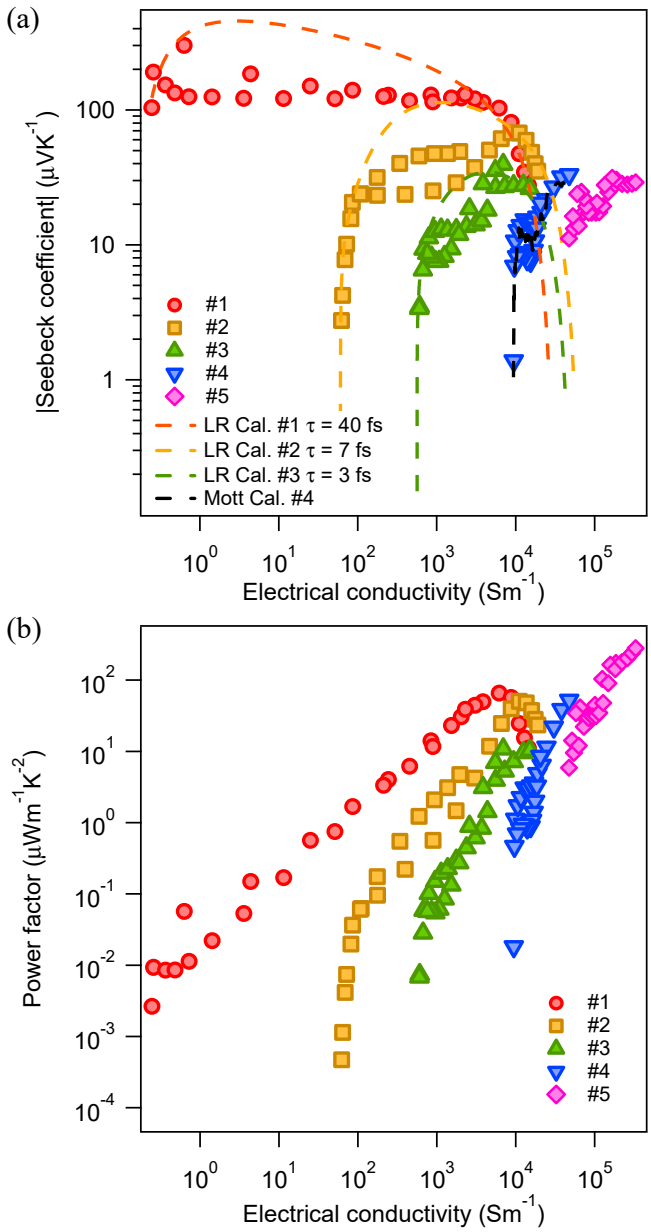

Figure 4.6. Seebeck coefficient and power factor of carbon nanotube films with different semiconductor-metal ratios. (a) Relationship between the absolute value of Seebeck coefficient and conductivity of the five samples [see Table 4.1]. (b) Relationship between power factor and conductivity of the five samples with different semiconductor-metal ratios (#1: 100%-0%, red circles; # 2: 90%-10%, orange squares; #3: 50%-50%, green triangles; #4: 0%-100%, blue inverted triangles; #5: 0%-100%, pink diamonds). The dashed lines in panel (a) are theoretical simulations. Mott's formula was used for sample 4 (Mott Cal.), whereas the linear response theory combined with the thermal Green's function method within the constant-relaxation-time approximation was used for samples 1−3 (LR Cal.). Adapted with permission from Y. Ichinose et al., Nano letters 19, 7370 (2019). Copyright 2019 American Chemical Society.

4.4 Discussion

In this section, we discuss the observations of S and P quantitatively to clarify the relationship between the electronic structure of SWCNTs and the thermoelectric properties.

4.4.1 Application of Mott formula to metallic SWCNTs

We first analyzed the relationship between S and σ for all samples on the basis of the standard Mott formula for metals [124]:

$$S = -\frac{\pi^2 k_{\mathrm{B}}^2 T}{3e} \frac{1}{\sigma(V_{\mathrm{G}})} \frac{\partial \sigma(V_{\mathrm{G}})}{\partial V_{\mathrm{G}}} \left(\frac{\partial \mu}{\partial V_{\mathrm{G}}} \right)^{-1}. \quad (4.1)$$

Here, $\sigma(V_{\mathrm{G}})$ is a function of V_{G} as measured in Section 4.3. We assume $\partial\mu/\partial V_{\mathrm{G}}$ to be constant; that is, $\mu = \alpha V_{\mathrm{G}}$, where α is a fitting parameter. **Figure 4.7** compares the calculation results with the experimental data for samples 1-5. As shown in the figure, this analysis well reproduced the experimental data for sample 4 and 5, indicating that, in metallic SWCNTs, the behavior of S is consistent with the conventional Mott formula, in which the increase of S can be attributed to the increase of DOS as μ increases. Hence, the simultaneous increase of S and σ can be interpreted as a consequence of the μ approaching the first 1D vHs in metallic SWCNTs.

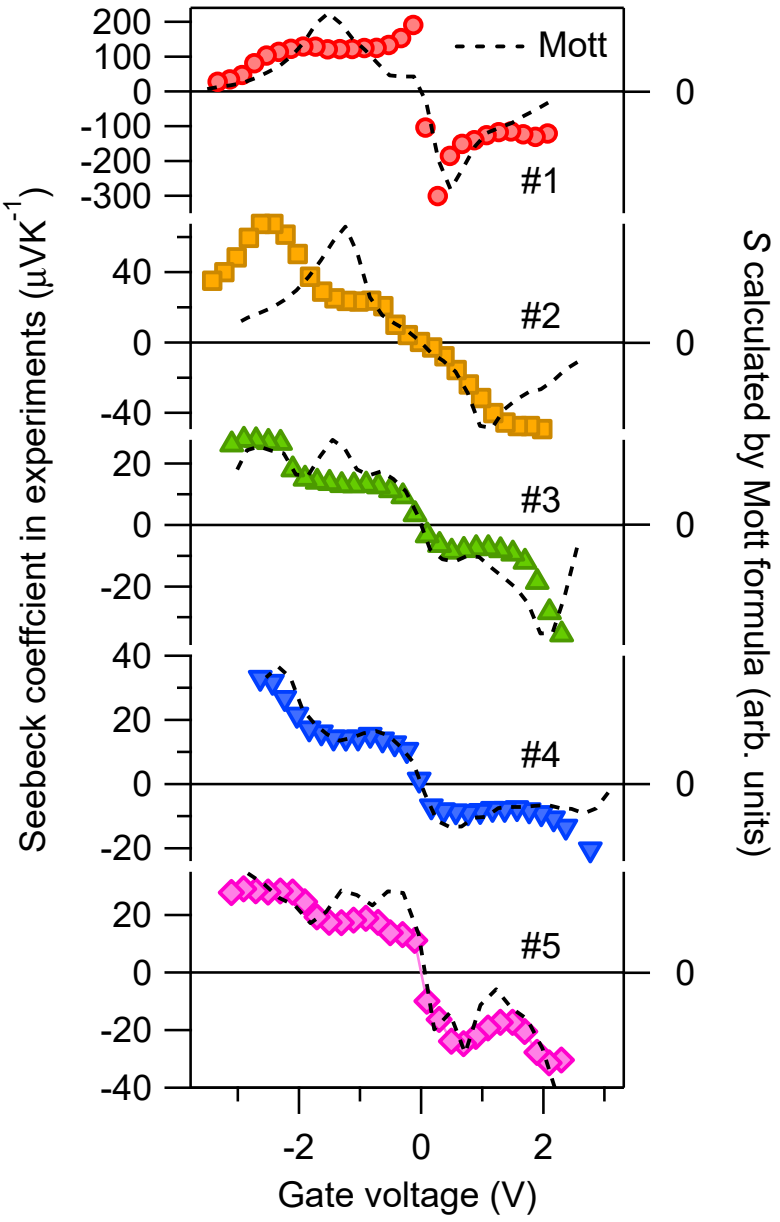

Figure 4.7. Comparison between experimental data and theoretical calculation by the Mott formula for the five samples with different semiconductor-metal ratios (#1: 100%-0%, red circles; # 2: 90%-10%, orange squares; #3: 50%-50%, green triangles; #4: 0%-100%, blue inverted triangles; #5: 0%-100%, pink diamonds). Color points are the experimental data and black dashed lines are the results of calculations by the Mott formula. Adapted with permission from Y. Ichinose et al., Nano letters 19, 7370 (2019). Copyright 2019 American Chemical Society.

4.4.2 Kubo-Lüttinger theory

The results for high-purity semiconducting samples (samples 1 and 2) cannot be explained within the conventional Mott formalism [see **Figure 4.7**]. Equation (4.1) or an approximate formula more appropriate for conventional semiconductors [4,152], completely fails to reproduce the observed behavior. The reason for this is that the energy region from the band edge to the band gap of semiconducting SWCNTs is not appropriate to be treated by the Boltzmann transport equation because the system is highly disordered [120]. Therefore, in order to calculate the relationship between S and σ in samples 1−3, we used the linear response theory combined with the thermal Green's function method within the constant-relaxation-time approximation [119]. The details of the calculation procedure are given in Appendix. We assumed that the electronic dispersions near the conduction- and valence-band edges of a (6,5) SWCNT can be described as gapped 1D Dirac bands. The presence of metallic SWCNT impurities in these samples can be treated by introducing finite DOS inside the band gap, or "in-gap states," the amount of which can be represented by the relaxation time of Dirac electrons. Thus, we varied the relaxation time depending on the sample as a fitting parameter. The calculation results are shown as dashed lines in **Figure 4.6**(a). There is a good overall agreement between theory and experiment.

4.4.3 Validity of the high performance of metallic SWCNTs

To further corroborate our finding that metallic SWCNTs can be better thermoelectric materials than semiconducting SWCNTs, we examined the relationships among S, electrical conductance G, and $P' \equiv S^2G$ of single (6,5) and (10,10) SWCNTs using the nonequilibrium Green's function formalism. Detailed calculation methods are given in Appendix. (10,10) SWCNTs are metallic with a diameter of ~1.4 nm, which is assumed to be the metallic SWCNTs used in the experiment. **Figure 4.8** demonstrates the G, S, P', and DOS obtained from the calculation. Focusing on DOS, the values of chemical potential at which DOS diverges sharply, *i.e.*, the first vHs, are approximately ±0.5 eV and ±0.8 eV for (6,5) and (10,10) SWCNTs, respectively. At these points, (6,5) SWCNTs show an increase in G and a decrease in the absolute value of S. On the other hand,

(10,10) SWCNTs show an increase in G and peak structures in S. The behavior is consistent with the expected behavior of each in **Figure 4.1**. As a result, both (6,5) and (10,10) SWCNTs have maximum values of P' at the first vHs.

Figure 4.9 represents a plot of S and P' with σ on the horizontal axis to facilitate comparisons with the experimental results. As shown in **Figure 4.9**(a), for a (6,5) SWCNT, which is semiconducting, S decreases as G increases; *i.e.*, the usual trade-off is observed. However, in a (10,10) SWCNT, which is metallic, we can identify a region

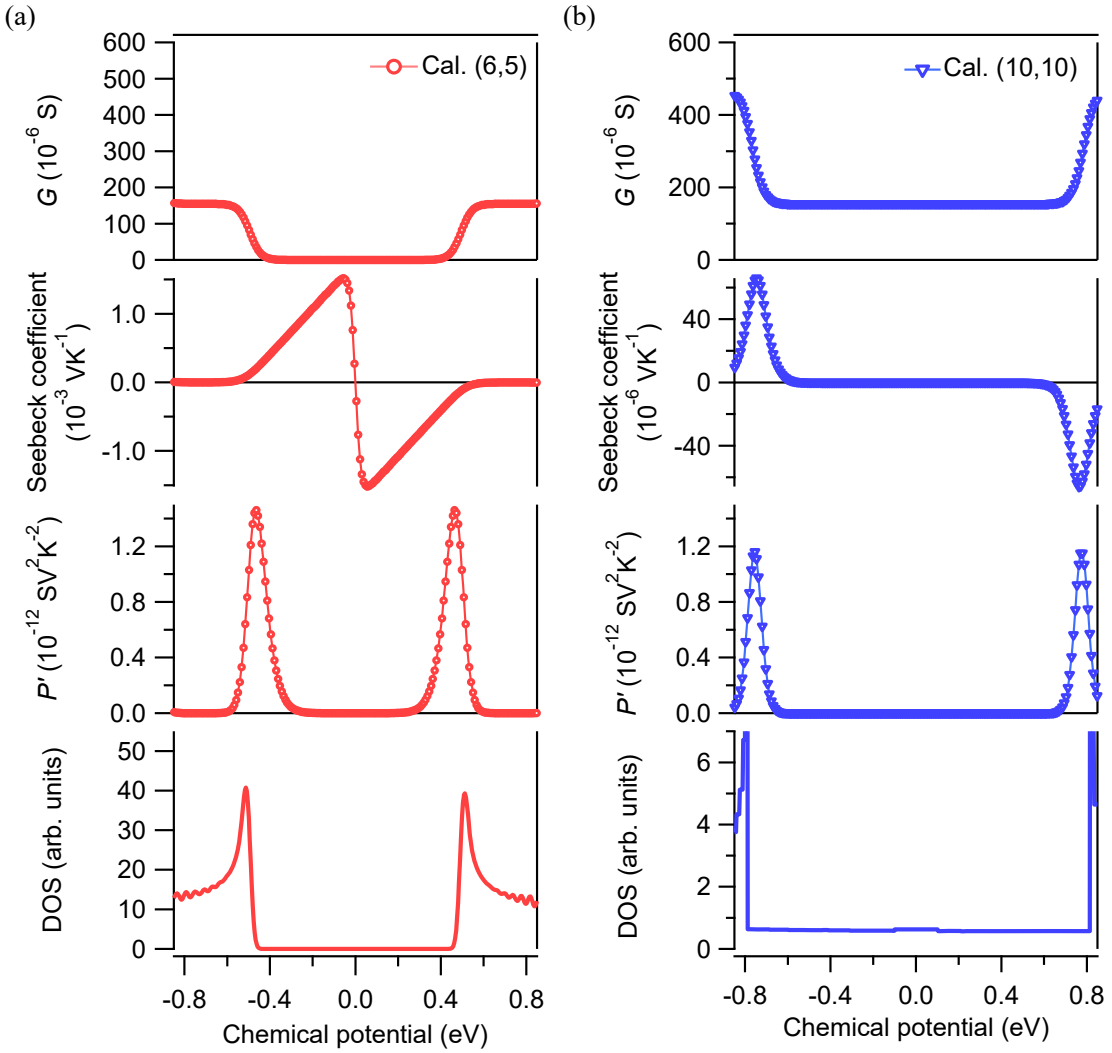

Figure 4.8. Calculated conductance, Seebeck coefficient, power factor and DOS of (a) (6,5) and (b) (10,10) SWCNT are shown as a function of chemical potential. Adapted with permission from Y. Ichinose et al., Nano letters 19, 7370 (2019). Copyright 2019 American Chemical Society.

where S and G simultaneously increase, which is similar to the experimentally observed behavior. These calculations clearly indicate that this behavior is caused by the enhancement of S around the first vHs of the metallic SWCNT. Regarding the power factor (Figure 4.9(b)), in a large G region ($> 10^{-4}$ S), the P' of the (10,10) SWCNT increases with G, achieving a peak value at $G \approx 3 \times 10^{-4}$ S, which is comparable to the peak P' value of the (6,5) SWCNT. Although these calculations were performed on single SWCNTs and thus cannot be directly compared with our experimental data on macroscopic films, the results basically support the notion that a chemical-potential-optimized metallic SWCNT can be a better thermoelectric material than a semiconducting SWCNT.

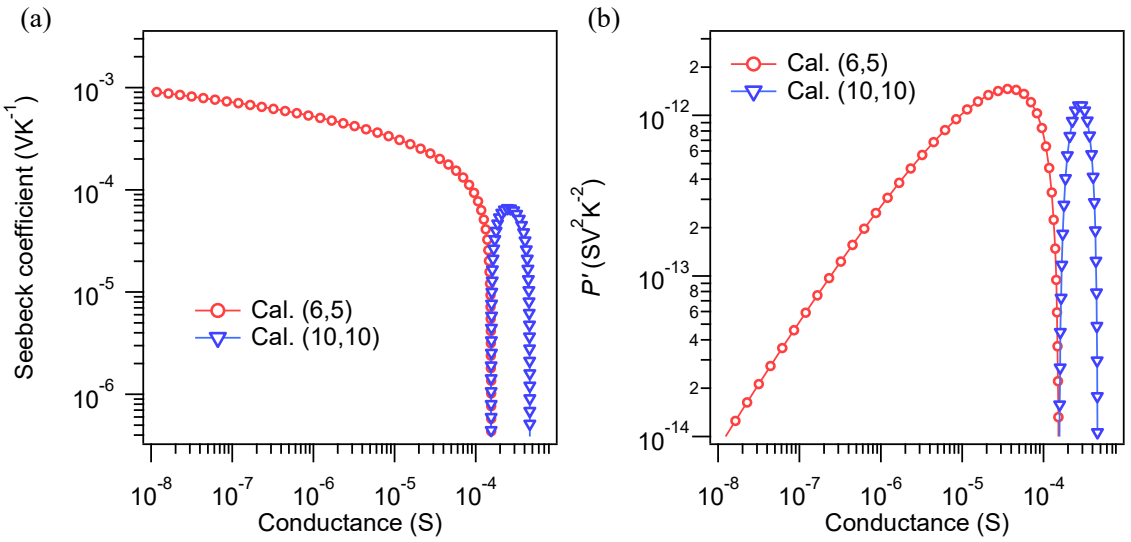

Figure 4.9. Calculated Seebeck coefficient and power factor of (6,5) and (10,10) SWCNTs as a function of electrical conductance. (a) Relationship between Seebeck coefficient and electrical conductance and (b) relationship between power factor and electrical conductance for a (6,5) SWCNT (red circles) and a (10,10) SWCNT (blue triangles) calculated using the nonequilibrium Green's function method. Adapted with permission from Y. Ichinose et al., Nano letters 19, 7370 (2019). Copyright 2019 American Chemical Society.

4.5 Conclusion

It is important to emphasize that metallic SWCNTs show negligibly small S and P when μ is near the CNP, consistent with conventional wisdom that high-purity semiconducting nanomaterials are far superior to metallic nanomaterials for thermoelectric applications. However, metallic SWCNTs are unique in possessing semiconductor-like properties [159,160], especially wide chemical potential tunability. When we move μ from the CNP, either to the *p*- or *n*-side, both S and σ increase. This behavior can be attributed to the existence of the 1D vHs in the DOS of metallic SWCNTs. Contrastingly, although there is a plateau region where S is almost constant as a function of σ, semiconducting SWCNTs exhibit the conventional trade-off, *i.e.*, S decreases with increasing σ. As a result, the P of metallic SWCNTs can become larger than that of semiconducting SWCNTs in the largest σ region.

Chapter 5

One-Dimensionality on Thermoelectric Properties of Semiconducting SWCNTs

Lowering the dimensionality of semiconductor thermoelectric materials is a promising approach for improving thermoelectric performance, ultimately one-dimensional (1D) semiconductor materials. However, experimentally verifying the effect of the 1D nature on the thermoelectric performance in semiconductor nanomaterials has been difficult because we cannot observe any traces of the 1D electronic structure in terms of conventional thermoelectric parameters, such as the Seebeck coefficient or power factor. Here, we show that a thermoelectric parameter, the thermoelectrical conductivity (L_{12}), is strongly correlated with the electronic structure and exhibits a unique 1D trace with single-walled carbon nanotubes (SWCNTs). We experimentally clarify that the L_{12} of high-purity semiconducting SWCNTs has a peak structure with a chemical potential in the vicinity of the vHs. For comparison, the L_{12} of monolayer molybdenum disulfides and graphene, which are chosen as 2D models, shows a different behavior, simply exhibiting constant values. Furthermore, we find that theoretical calculations support these L_{12} behaviors, which are consistent with the expected behaviors of 1D and 2D electronic structures. Our results demonstrate that L_{12} is a very good parameter for evaluating the traces of dimensionalities, thereby advancing the elucidation of the fundamental thermoelectric properties necessary for the development of low-dimensional materials.

5.1 Introduction

The demand for flexible high-performance thermoelectric materials to power wearable electronics and sensors has been increasing [4]. Semiconductor materials with low dimensions have been pursued for their superior thermoelectrics, as predicted in seminal papers by Hicks and Dresselhaus [65]. In particular, one-dimensional (1D) semiconductor materials are expected to achieve the highest performance due to the decrease in thermal

conductivity and the formation of 1D electronic structures, such as the van Hove singularity (vHs) in the density of states (DOS) [19,66]. The former factor has been experimentally confirmed by many studies [20,28]; however, the experimental verification of how the 1D electronic structure influences the thermoelectric properties remains elusive. One of the reasons is that it is very difficult to discuss the dimensionalities of conventional thermoelectric parameters, such as the Seebeck coefficient S and power factor P. For example, within conventional theoretical models, such as the Boltzmann transport theory with a constant relaxation-time approximation and an effective-mass approximation, S in the band gap of a d-dimensional ($d = 1, 2, 3$) semiconductor as a function of the chemical potential μ can be expressed as

$$S = \frac{k_{\mathrm{B}}}{q}\left(\frac{d}{2} - \frac{\mu}{k_{\mathrm{B}}T} + 1\right), \tag{5.1}$$

where k_{B} is Boltzmann's constant, q is the charge of carriers, and T is the temperature [116]. Equation (5.1) indicates that the difference in d does not influence the line shapes of S as a function of μ. Thus, the doping dependence of S, *i.e.*, the shift of μ, never signals the dimensionality. These characteristics make it difficult to understand how lowering the dimensions of materials enhances the thermoelectric performance, except for the apparent tendency of lowering the thermal conductivity.

Recently, a theoretical study using the linear-response theory by Yamamoto and Fukuyama noted the importance of the L_{12} term, which they called the "thermoelectrical conductivity," for understanding the thermoelectric properties of nanomaterials [119]. Here, we briefly discuss their notations. The current density J in the presence of an electric field E and a temperature gradient dT/dx along the x-direction is described as

$$J = L_{11}E - \frac{L_{12}}{T}\frac{dT}{dx}. \tag{5.2}$$

Here, $E = -\Delta V/L$ and $dT/dx = \Delta T/L$ for a spatially uniform system with length L, where we have introduced a temperature difference ΔT and an induced voltage ΔV between the two ends of the materials. L_{11} corresponds to the electrical conductivity σ. According to the definition, S is expressed as $S = L_{12}/(T\sigma)$. Yamamoto and Fukuyama's paper implies that the structure of the DOS significantly affected the line shape of

the L_{12} term. The line shape of the DOS reflects the dimensionality of the electronic structure of the samples, suggesting that traces of the dimensionalities can be found in the L_{12} term. The clarification of the independent thermoelectric parameter, which strongly couples with the dimensionality of the electronic structure or the structure of the DOS, will provide a bottom-up strategy for applying low-dimensional effects to improve thermoelectric performance. Therefore, in this study, first we theoretically discuss the relationships between the dimensionality and thermoelectric parameters, including L_{12}, in the Boltzmann transport theory framework, and then we discuss the line shapes of L_{12} using actual samples that utilize semiconducting single-walled carbon nanotubes (SWCNTs), which are 1D models. We compare these line shapes with the L_{12} line shape of molybdenum disulfide (MoS_2) and graphene, which are 2D models, and then we demonstrate how the 1D characteristics appear in the L_{12} of semiconducting SWCNTs.

5.2 Theory

5.2.1 Boltzmann expression of thermoelectric coefficients for semiconductors

In this section, we summarize how the thermoelectric parameters are represented in a simple system using the Boltzmann expression. We mainly discuss the electrical conductivity $L_{11}(=\sigma)$, the thermoelectrical conductivity L_{12} and Seebeck coefficient $S = L_{12}/TL_{11}$ when the chemical potential μ lies in (A) a band gap and (B) a conduction- and valence-band.

According to the Sommerfeld-Bethe relation, L_{11} and L_{12} are

$$L_{11} = \int_{-\infty}^{\infty} dE \left(-\frac{\partial f(E-\mu)}{\partial E}\right) \alpha(E)\,, \tag{5.3}$$

and

$$L_{12} = \frac{1}{q}\int_{-\infty}^{\infty} dE \left(-\frac{\partial f(E-\mu)}{\partial E}\right) (E-\mu)\alpha(E), \tag{5.4}$$

where $f(E-\mu)$ is the Fermi-Dirac distribution function and $\alpha(E)$ is the spectral conductivity, and q is the charge of carrier. Hence, we need to know $\alpha(E)$ to derive L_{11} and L_{12}. For a d-dimensional homogenous semiconductor ($d = 1, 2, 3$), when the relaxation time τ of carriers is sufficiently long because of low-concentration scatters, $\alpha(E)$

can be described by the Boltzmann expression as

$$\alpha(E) = 2q^2\rho(E)\tau(E)\frac{\upsilon^2(E)}{d} \tag{5.5}$$

where the factor 2 reflects the spin degeneracy, $\rho(E)$ is the density of states per unit volume, and $\upsilon(E)$ is the group velocity of carrier. Considering a d-dimensional semiconductor with a bandgap 2Δ, $\upsilon^2(E)$ and $\rho(E)$ of a free electron having an effective mass m^* are

$$\upsilon^2(E) = \frac{2(|E|-\Delta)}{m^*}, \qquad |E| \geq \Delta \tag{5.6}$$

and

$$\rho(E) = \rho_0^d(|E|-\Delta)^{\frac{d}{2}-1}, \qquad |E| \geq \Delta. \tag{5.7}$$

Here, ρ_0^d is a coefficient depending on the dimension d:

$$\rho_0^d = \frac{1}{2^{\frac{d}{2}}(2\pi)^{\frac{d}{2}}\Gamma\left(\frac{d}{2}\right)a^{3-d}}\left(\frac{2m^*}{\hbar^2}\right)^{\frac{d}{2}}, \tag{5.8}$$

where a is the length of a unit cell and $\Gamma(\frac{d}{2})$ is the gamma function. Substituting Eqs. (5.6) and (5.7) into Eq. (5.5), we obtain

$$\alpha(E) = \frac{4q^2\rho_0^d\tau(E)}{m^*d}(|E|-\Delta)^{\frac{d}{2}}, \qquad |E| \geq \Delta. \tag{5.9}$$

(A) μ-dependence of L_{11}, L_{12}, and S in band gap ($-\Delta < \mu < \Delta$)

When μ lies in band gap of semiconductors, Fermi-Dirac distribution function can be approximately expressed as Boltzmann distribution function $f(E-\mu) \approx \exp\left(-\frac{E-\mu}{k_{\mathrm{B}}T}\right)$, thus, L_{11} and L_{12} are given as

$$L_{11} = \frac{4q^2\rho_0^d\tau}{m^*d}(k_{\mathrm{B}}T)^{\frac{d}{2}}e^{\frac{|\mu|-\Delta}{k_{\mathrm{B}}T}}\Gamma\left(\frac{d}{2}+1\right) \tag{5.10}$$

and

$$L_{12} = \frac{4q\rho_0^d\tau}{m^*d}(k_{\mathrm{B}}T)^{\frac{d}{2}+1}e^{\frac{|\mu|-\Delta}{k_{\mathrm{B}}T}}\left(\frac{d}{2}+1-\frac{|\mu|-\Delta}{k_{\mathrm{B}}T}\right)\Gamma\left(\frac{d}{2}+1\right) \tag{5.11}$$

within the constant-τ approximation. Therefore, S is given by

$$S = \frac{1}{T}\frac{L_{12}}{L_{11}} = \frac{k_{\mathrm{B}}}{q}\left(\frac{d}{2}+1-\frac{|\mu|-\Delta}{k_{\mathrm{B}}T}\right). \tag{5.12}$$

Note that Eqs. (5.10), (5.11) and (5.12) are valid for single-band electron systems, and thus, they cannot apply to the band center around $\mu = 0$.

(B) μ-dependence of L_{11}, L_{12}, and S in conduction and valence bands ($\mu \gg \Delta$)

When μ lies in the conduction or valence bands, $\alpha(E)$ can be expanded by Taylor expansion around $E = \mu$ as

$$\alpha(E) = \alpha(\mu) + \alpha'(\mu)(E - \mu) + \cdots. \tag{5.13}$$

Substituting Eq. (5.13) into Eqs. (5.3) and (5.4), low-temperature L_{11} and L_{12} are approximately expressed as

$$L_{11} \approx \frac{4q^2\rho_0^d\tau}{m^* d}(|\mu| - \Delta)^{\frac{d}{2}} \tag{5.14}$$

and

$$L_{12} \approx \frac{2\pi^2 q\rho_0^d\tau}{3m^*}(k_{\mathrm{B}}T)^2(|\mu| - \Delta)^{\frac{d}{2}-1} \tag{5.15}$$

within the constant-τ approximation. Therefore, S is also approximately given by

$$S \approx \frac{\pi^2 k_{\mathrm{B}} d}{6q}\frac{k_{\mathrm{B}}T}{|\mu| - \Delta}. \tag{5.16}$$

Table 5.1 summarizes L_{11}, L_{12}, and S derived above in (A) a band gap region and (B) a conduction- and valence-band energy region.

Table 5.1. Relationship between thermoelectric properties and the location of chemical potential.

	(A) $-\Delta < \boldsymbol{\mu} < \Delta$		**(B)** $\boldsymbol{\mu} \gg \lvert\Delta\rvert$	
$\boldsymbol{L_{11}}$	$\propto e^{\frac{\lvert\mu\rvert-\Delta}{k_{\mathrm{B}}T}}$	Eq. (5.10)	$\propto (\lvert\mu\rvert - \Delta)^{\frac{d}{2}}$	Eq. (5.14)
$\boldsymbol{L_{12}}$	$\propto \mp\left(\frac{d}{2} + 1 - \frac{\lvert\mu\rvert-\Delta}{k_{\mathrm{B}}T}\right) e^{\frac{\lvert\mu\rvert-\Delta}{k_{\mathrm{B}}T}}$	Eq. (5.11)	$\propto \mp(\lvert\mu\rvert - \Delta)^{\frac{d}{2}-1}$	Eq. (5.15)
$\boldsymbol{S}$	$\propto \pm(\lvert\mu\rvert - \Delta)$	Eq. (5.12)	$\propto \mp(\lvert\mu\rvert - \Delta)^{-1}$	Eq. (5.16)

5.2.2 Relationships between dimensionality and thermoelectric properties

We discuss the relationships among the dimensionalities, S, P, and L_{12}. **Figure 5.1** describes the calculated DOS, S, P, and L_{12} for semiconductor models with 1D, 2D, and 3D electronic structures. The calculations are performed within the Boltzmann transport theory with a constant relaxation-time approximation and effective-mass

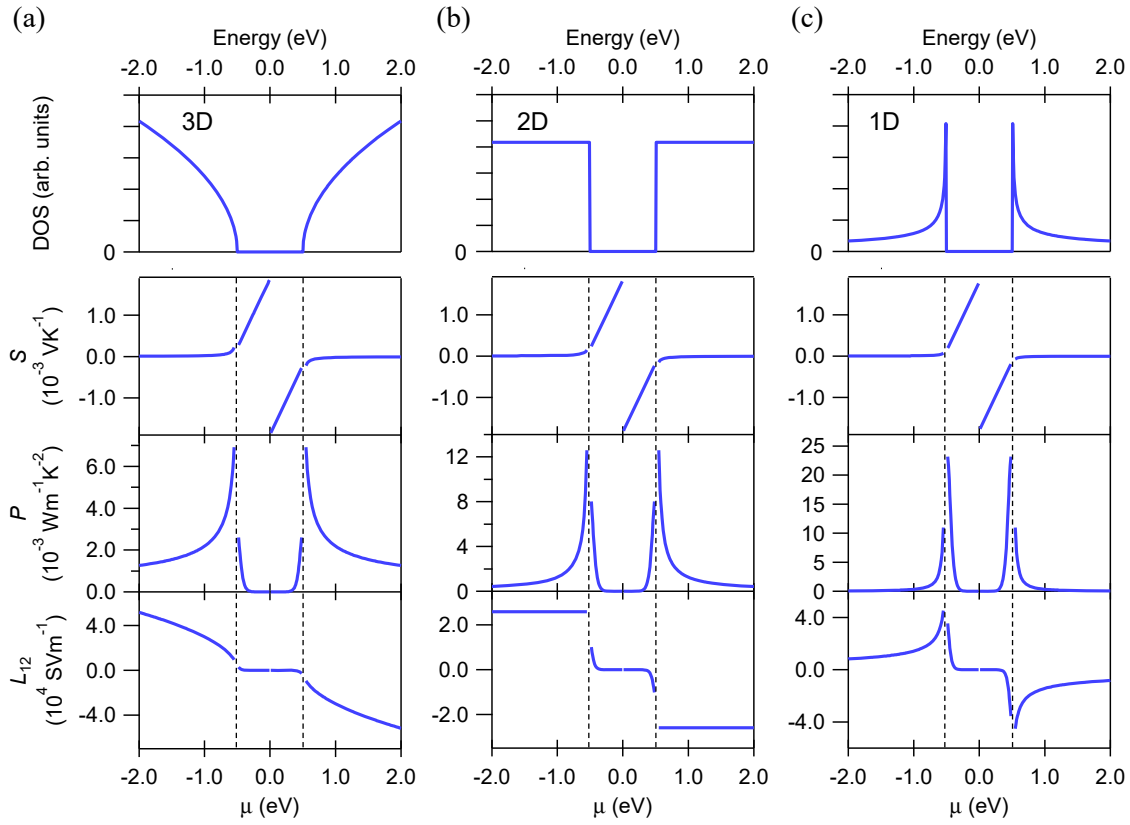

Figure 5.1. Thermoelectric properties for homogeneous semiconductors calculated using the Boltzmann transport theory within an effective-mass approximation. The top panels show the energy dependence of the density of states (DOS) for (a) 3D, (b) 2D, and (c) 1D structures. Underneath the top row and from top to bottom, the panels show the Seebeck coefficient (S), power factor (P), and thermoelectrical conductivity (L_{12}) as a function of chemical potential (μ) for an effective mass $m^* = 9.11 \times 10^{-31}$ kg, a relaxation time $\tau = 100$ fs, and a unit-cell length $a = 1$ nm at $T = 300$ K. The vertical axes of (b) and (c) are the same as those in (a). The band edges of the valence and conduction bands for all semiconductors are set to ±0.5 eV (dotted lines). Details are provided in **Table 5.1**. Reprinted figure with permission from Y. Ichinose et al., Phys. Rev. Mater. 5, 025404 (2021). Copyright 2021 by the American Physical Society.

approximation [see **Table 5.1**]. Note that the Boltzmann transport theory cannot apply to the disordered state in the energy region around the band edges [120]. Here, we plot the data by setting the potential of μ at the charge neutral point to zero. As shown in the figures, although the line shapes of the DOS change depending on the dimensionalities, those of S are similar among all the dimensions. Regarding P, the value just becomes the maximum around the band edge in any dimensionality, and the line shapes are almost the same. Therefore, we cannot distinguish the dimensionalities of the samples from the conventional thermoelectric parameters S and P. However, in the case of L_{12}, the line shapes exhibit distinct characteristics depending on the dimensionalities. The L_{12} values are negligible in all dimensions when μ is located within the band gap. In 3D, the absolute values of L_{12} increase monotonically as μ shifts from the band-edge position. However, in 2D, the values are constant, and in 1D, the value becomes the maximum around the band edge and decreases as μ shifts from the band edge. These simple theoretical analyses clearly indicate that L_{12} is a good parameter to discuss the dimensionalities of thermoelectric properties.

From an experimental point of view, it is rather difficult to precisely discuss the thermoelectric parameters as a function of μ. Thus, we plotted the relationship between the thermoelectric parameters and σ in the 3D, 2D, and 1D semiconductors in **Figure 5.2**. Here, σ at the band edge is described as σ_{b}. **Figure 5.2**(a–c) indicate the relationships between S and σ in the case of the 3D, 2D, and 1D electronic structures. As shown in the figures, it is very difficult to distinguish the dimensionalities from these plots. **Figure 5.2** (d–f) indicate the relationships between L_{12} and σ. These panels clearly present the characteristic behaviors that depend on the dimensionalities. In all dimensionalities, when μ is located within the band gap, *i.e.*, $\sigma < \sigma_{\mathrm{b}}$, L_{12} increases as σ increases. When μ is located outside the band gaps, *i.e.*, $\sigma > \sigma_{\mathrm{b}}$, in the 3D case L_{12} increases as σ increases, and in the 2D case L_{12} stays constant, whereas in the 1D case L_{12} decreases as σ increases. Therefore, L_{12} strongly reflects the dimensionalities of the electronic structure of materials, indicating that we can deduce the dimensionality of samples from this term. Thus, to clarify this point, we experimentally investigated the L_{12} term with SWCNTs.

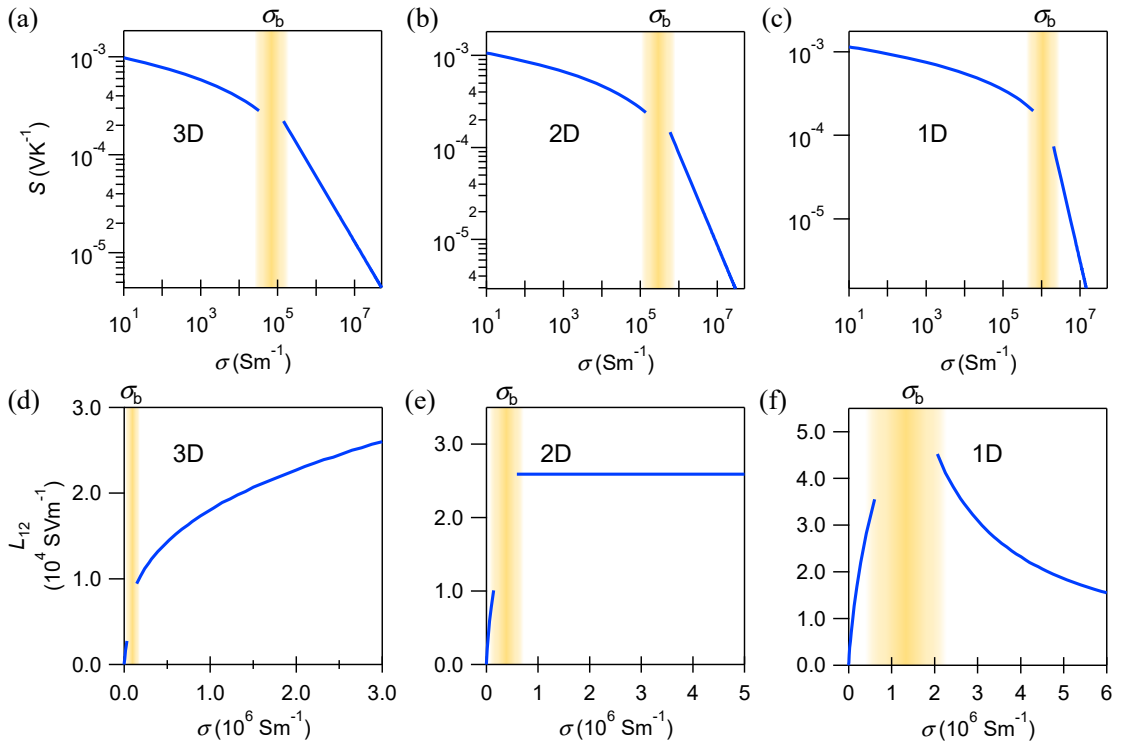

Figure 5.2. Thermoelectric parameters as a function of electrical conductivity (σ), calculated using the Boltzmann transport theory within an effective-mass approximation. The relationship is shown between the Seebeck coefficient (S) and σ for the (a) 3D, (b) 2D, and (c) 1D structures. σ at the band edge is described as σ_{b} (yellow gradient color). The vertical axes of (b) and (c) are the same as those in (a). The relationship is shown between thermoelectrical conductivity (L_{12}) and σ for the (d) 3D, (e) 2D, and (f) 1D structures. The vertical axes of (e) and (f) are the same as those in (d). Reprinted figure with permission from Y. Ichinose et al., Phys. Rev. Mater. 5, 025404 (2021). Copyright 2021 by the American Physical Society.

5.3 Experiments

SWCNTs are one of the most suitable materials for tackling this subject because they have a sharp vHs in the DOS of their individual states. Since the discovery of SWCNTs, many studies have been conducted focusing on the thermoelectric properties of SWCNTs in their individual and thin-film forms [16]. Regarding the topic of the 1D characteristics of thermoelectric properties, Chapter 4 revealed the uniqueness of the 1D thermoelectric properties of the "metallic" type as breaking the thermoelectric trade off. However, we could not those of the "semiconducting" type, because, as discussed above, we cannot identify the 1D characteristics in the behavior of conventional thermoelectric parameters in the case of semiconductors. Here, we focused on the thermoelectrical conductivity, namely the L_{12} term, of semiconducting SWCNTs to verify the traces of the vHs on the thermoelectric properties.

5.3.1 SWCNT film preparation

To systematically understand the relationships between the electronic structures of semiconducting SWCNTs and the thermoelectric properties, we prepared four kinds of semiconducting SWCNTs. High-purity semiconducting (6,5), (9,4), and (10,3) SWCNTs were prepared through gel chromatography from the original SWCNTs synthesized by the CoMoCAT© method (SG65, Sigma-Aldrich) for (6,5) and by HiPco (HiPco Raw SWNTs HR32-166, NanoIntegris) for (9,4) and (10,3). The details of these separation procedures can be found in Chapter 3. We also prepared Semiconducting SWCNTs (Semi) and metallic SWCNTs with a diameter of 1.4 nm using density gradient ultracentrifugation [86] from the original SWCNTs synthesized by the arc-discharge method (Arc SO, Meijyo Nano Carbon Co.). **Figure 5.3** shows sample information for four semiconducting SWCNTs, namely, (6,5), (9,4), (10,3), and Semi. We can see the sharp vHs, i.e., 1D electronic structure and the corresponding optical absorption peak. Metallic SWCNTs was used in the purity dependence experiments (**Figure 5.8**). In the purity dependence experiments, we prepared samples by mixing the (6,5) and metallic SWCNTs as the same manner of Chapter 4. The films were prepared using conventional transfer techniques using a polycarbonate membrane filter (Whatman Nuclepore Track-Etched membrane 25 mm 0.2 μm) to form a thin film.

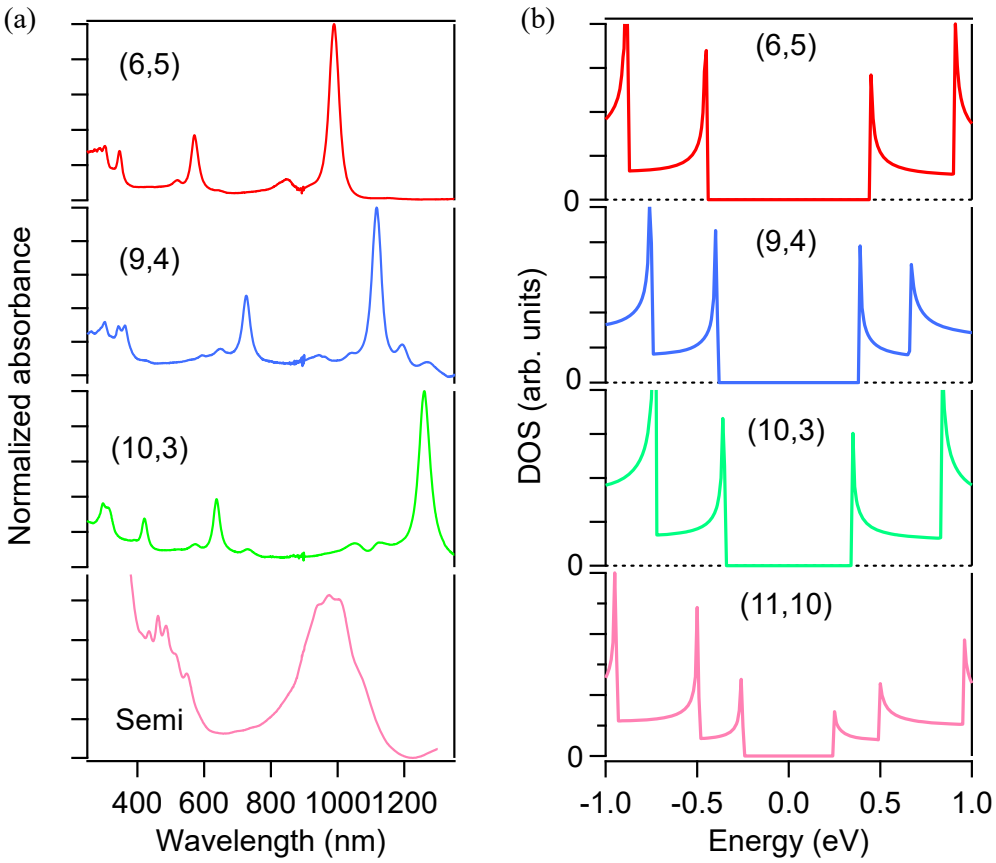

Figure 5.3. Sample information for four semiconducting species of SWCNTs. (a) Optical absorbance spectra for (6,5), (9,4), (10,3), and Semi SWCNTs. The largest peaks in (6,5), (9,4) and (10,3) are S_{11} peaks, which is the absorbance between 1st vHs of a valence band and a conduction band. The largest peak in Semi around 1000 nm corresponds to S_{22} peaks of semiconducting SWCNTs. (b) Density of states calculated by the tight-binding method. Detailed calculation methods are given in Appendix C.2. Since Semi contains several semiconducting chiralities with a diameter of about 1.4 nm, the main chirality, (11,10), is shown as a representative. Reprinted figure with permission from Y. Ichinose et al., Phys. Rev. Mater. 5, 025404 (2021). Copyright 2021 by the American Physical Society.

5.3.2 Device fabrication and the evaluation of thermoelectric properties

To experimentally investigate the thermoelectric properties over a wide range of carrier densities, we systematically controlled the carrier injection by an electrolyte gating technique, which is a method used in previous studies [98,161]. The details of device structures and the method of measurements are the same as Chapter 4 [see **Figure 4.3**]. We used an ionic liquid (TMPA-TFSI, Kanto Chemical Co.) for the electrolyte. All the

measurements were conducted in vacuum (~10^{-3} Pa) using a vacuum and low-temperature probe station (Grail 10, Nagase Techno Co.). Although S and σ values of (6,5) have already been evaluated in Chapter 4, we prepared another (6,5) sample with the same high purity (>99%) for this study to evaluate its L_{12}, S, and σ. In addition, we clarified the thermoelectric properties of (9,4), (10,3), and Semi SWCNTs and evaluated the L_{12} values.

By changing the gate voltage V_{G}, the carrier injection is precisely controlled. L_{12} and P are obtained experimentally by measuring σ and S at each V_{G}. On the other hand, it is rather difficult to precisely determine the relationships between the V_{G} and the location of μ in the SWCNT networks; thus, the L_{12} obtained in this study is plotted and discussed as a function of σ.

5.4 Results

5.4.1 Gate voltage dependence of electrical conductivity and Seebeck coefficient

First, we depict σ and S of the semiconducting SWCNTs with different chiralities as a function of V_{G} in **Figure 5.4**. In all the plots, the charge neutral point is set at $V_{\mathrm{G}} = 0$ V. The transport properties of all the samples show clear ambipolar behaviors and an on/off ratio $\geq 10^4$. Reflecting the ambipolar behavior, S exhibits positive or negative values, depending on the carrier type. The maximum values of S are exhibited around the charge neutral point and decrease as V_{G} shifts. Such behavior is in agreement with

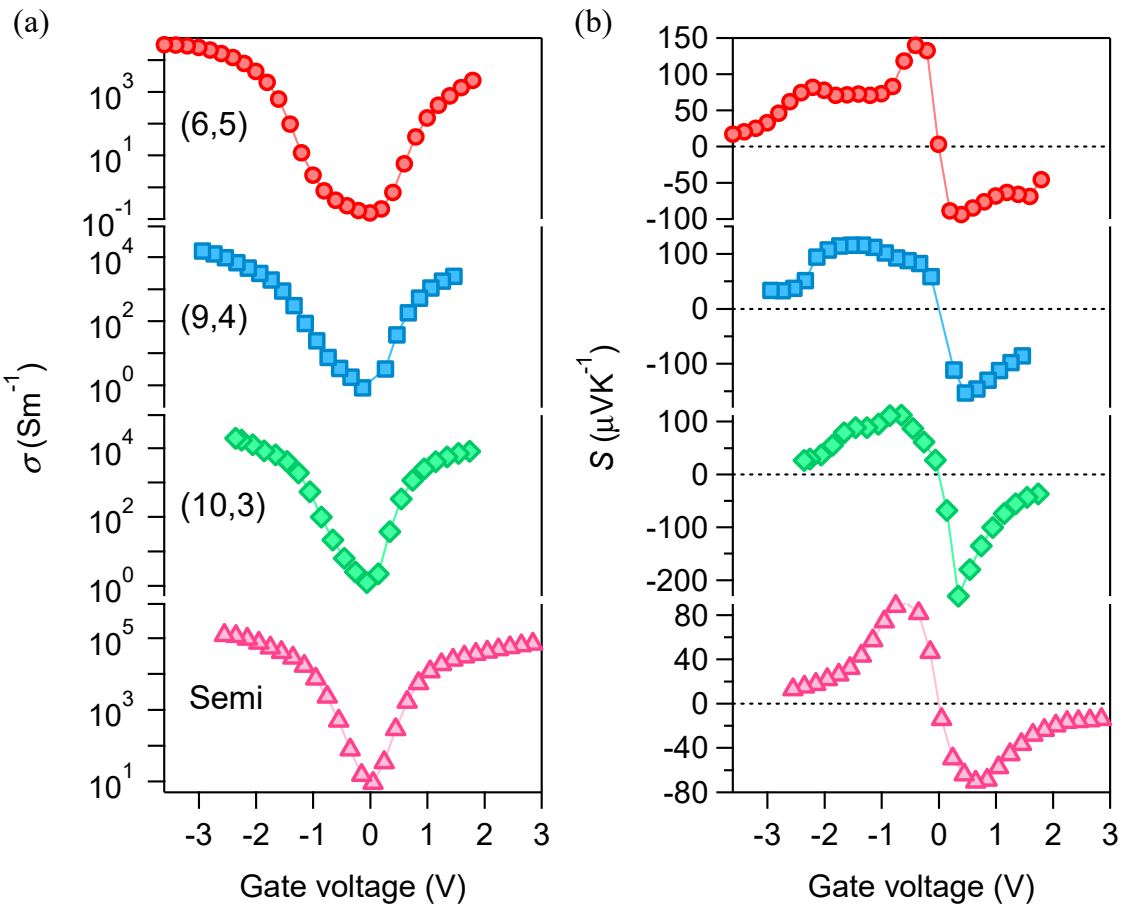

Figure 5.4. Experimental results of four species of SWCNT films. (a) electrical conductivity (σ) and (b) Seebeck coefficient (S) of SWCNT films as a function of gate voltage. From the top panel to bottom, the panels show (6,5), (9,4), (10,3), and Semi. In the all plots, the charge neutral points are set at $V_G = 0$ V. Reprinted figure with permission from Y. Ichinose et al., Phys. Rev. Mater. 5, 025404 (2021). Copyright 2021 by the American Physical Society.

the general trend of S vs. μ in semiconductors as discussed in Section 5.2.

5.4.2 Estimating the band edges of semiconducting SWCNTs

In this section, we analyze P to estimate the location of the band edge. **Figure 5.5**(a) shows the DOS of (6,5) obtained by Kubo-Lüttinger theory [119]. The details of calculations are shown in the Appendix. The vHs are located at around ±0.5 eV. **Figure 5.5**(b) plots P and σ as a function of μ. We found that P has peak structures at the positions of vHs, *i.e.*, at the band edges, which is consistent with the result in **Figure 5.1**(c). We note that $\sigma \sim 4 \times 10^6$ Sm^{-1} at the band edges. Subsequently, **Figure 5.5**(c) shows the relationship between P and σ. P takes a maximum at a black arrow

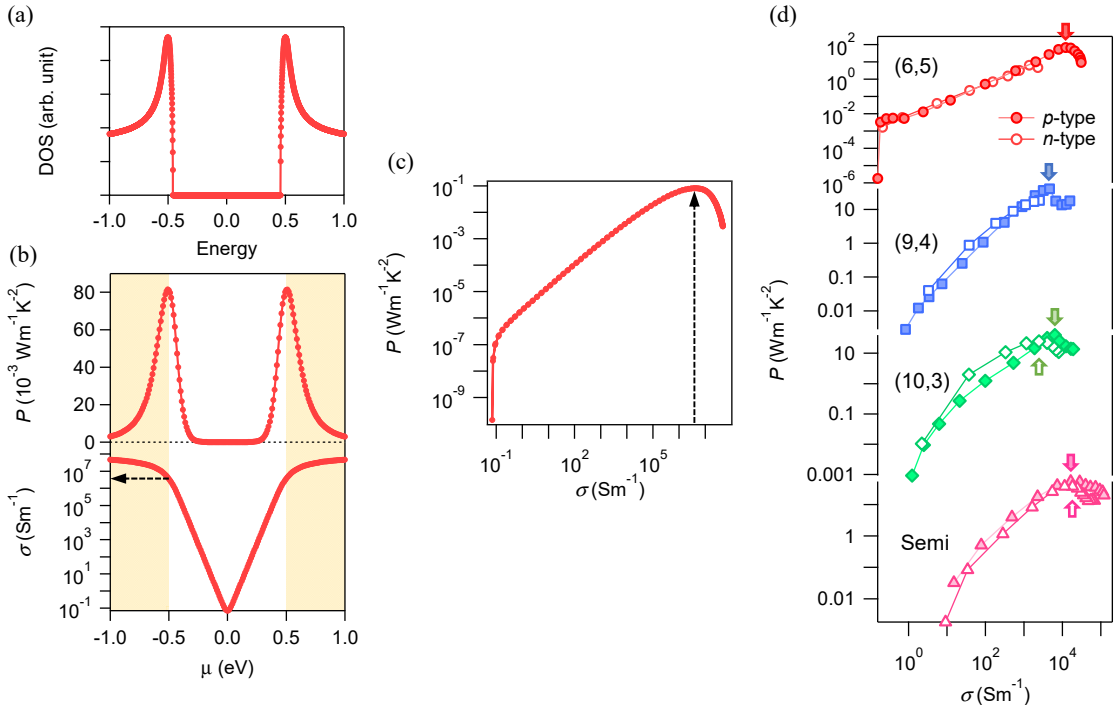

Figure 5.5. Estimation of the band edges of semiconducting SWCNTs using relationship between peaks in power factor (P) and electronic structures. (a) Calculated density of states (DOS) for (6,5) using Kubo-Lüttinger theory. (b) P and electric conductivity (σ) of (6,5) as a function of μ. (c) Plot of P vs. σ obtained from panel (b). The black arrow indicates the P peak, where $\sigma \sim 4 \times 10^6$ Sm^{-1}. (d) Relationship between P and σ for (6,5), (9,4), (10,3), and Semi obtained from the experiments. The peak positions of each chirality are pointed by small arrows. Color-filled markers represent the *p*-type and white outlined markers represent the *n*-type. Reprinted figure with permission from Y. Ichinose et al., Phys. Rev. Mater. 5, 025404 (2021). Copyright 2021 by the American Physical Society.

position, where $\sigma \sim 4 \times 10^6$ Sm^{-1}. Therefore, we conclude that the peak in the P–σ plot corresponds to the band edge of semiconducting SWCNTs and the high conductivity region to the right of this peak corresponds to the situation that the location of μ is in the conduction or valence band. Finally, **Figure 5.5**(d) represents the plots of P–σ for (6,5), (9,4), (10,3), and Semi obtained from the experiments. The line shapes are in good agreement with the calculated results in **Figure 5.5**(c). The peak positions of P of each chirality are pointed by small arrows. We defined the σ values at the P peak as $\sigma_{\rm b}$, which indicate the electrical conductivity when μ matches band edges.

5.4.3 Observation of one dimensionality in high-purity (6,5) SWCNTs.

Figure 5.6 presents the experimental result of the relationship between L_{12} and σ of the (6,5) SWCNTs. Here, we obtained L_{12} through the equation

$$L_{12} = SL_{11}T = S\sigma T, \tag{5.17}$$

where S and σ are experimentally measured values of **Figure 5.4**, and T is the room temperature. In order to focus on the appearance of the dimensionalities on the data, we plotted only the *p*-type regions of L_{12} because we obtained a clear P peak in *p*-type for the estimation of the band edge. As shown in the figure, L_{12} exhibits a clear peak structure around $\sigma \sim 1.6 \times 10^4$ Sm^{-1} and then gradually decreases as σ increases. We find that σ at this peak position almost corresponds to $\sigma_{\rm b}$. Therefore, we find that L_{12} reaches its maximum around the band edge and decreases as σ increases. These behaviors are consistent with the 1D behavior of L_{12} predicted in **Figure 5.2**(f) except for the energy region around the band edges. To evaluate the correctness of the observed behavior of L_{12}, we compare this experimental result to the theoretical calculation based on the Kubo-Lüttinger theory, which can apply even to disordered states around band edges [119,120,162]. Here, we used the linear-response theory combined with the thermal Green's function method [see Appendix]. The calculation results are plotted as a solid line in **Figure 5.6**(a). As shown here, the theoretical calculation based on the 1D Dirac model of (6,5) SWCNTs can reproduce the experimental L_{12} behavior of (6,5) SWCNTs.

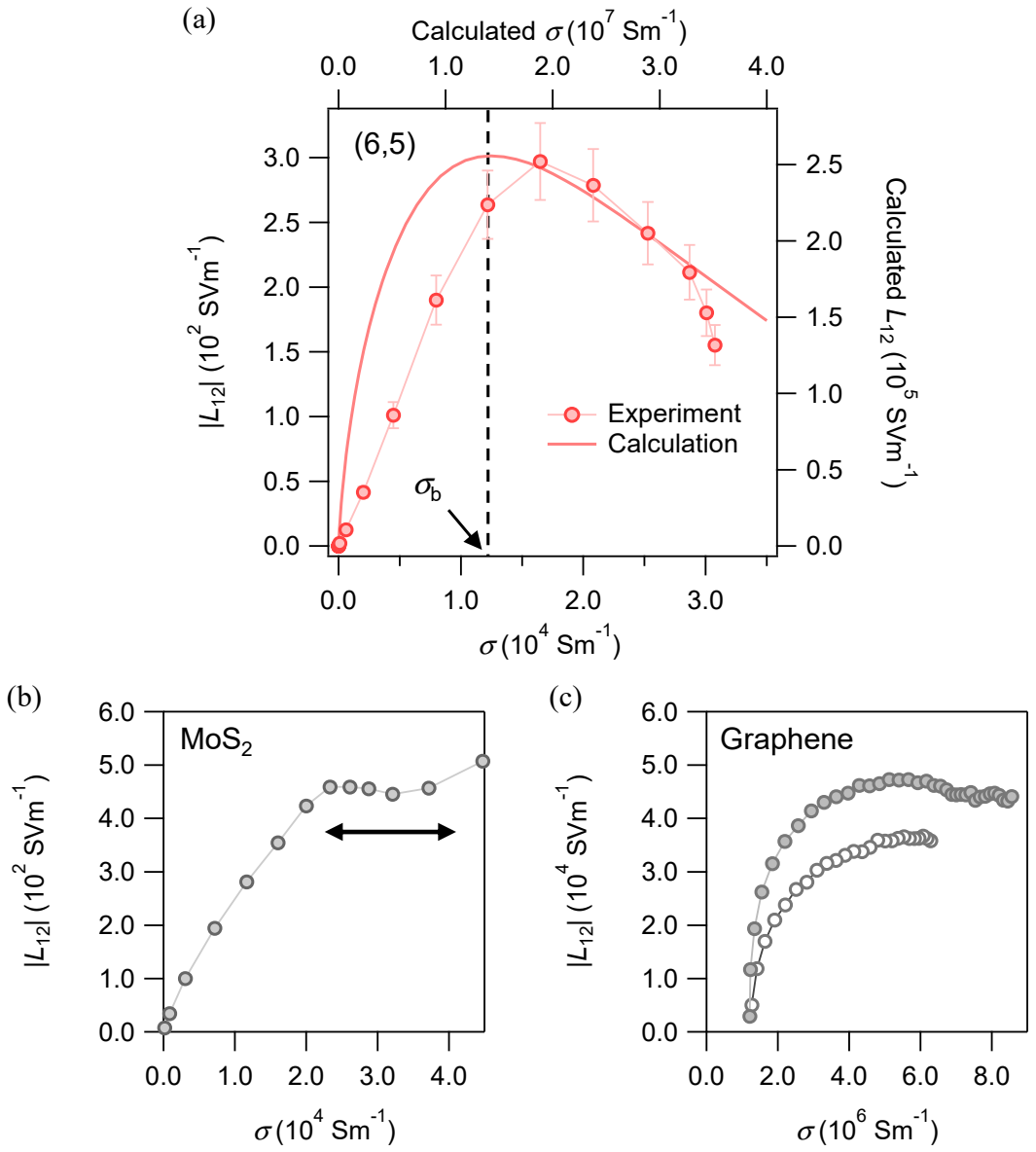

Figure 5.6. Experimental results of the thermoelectrical conductivity (L_{12}) as a function of electrical conductivity (σ). (a) $|L_{12}|$ for (6,5) SWCNTs. σ at the band edge is described as σ_b, which is obtained by analyzing the relationship between the power factor and σ (see **Figure 5.5**). A solid line presents the result of the theoretical calculation by the Kubo-Lüttinger theory. The relative error in L_{12} is ~10%, calculated from the Seebeck coefficient measurement errors of the devices. (b) $|L_{12}|$ for monolayer MoS_2 as a representative 2D semiconducting material. The black arrow indicates the plateau region. (c) $|L_{12}|$ for graphene. Color-filled markers represent the *p*-type and white outlined markers represent the *n*-type. Reprinted figure with permission from Y. Ichinose et al., Phys. Rev. Mater. 5, 025404 (2021). Copyright 2021 by the American Physical Society.

For comparison, we checked the L_{12} line shape of monolayer MoS_2, which is a model for 2D semiconductors. L_{12} is derived from the data of S and σ in Ref. [118]. As shown in **Figure 5.6**(b), in the case of MoS_2, L_{12} does not show a peak structure but rather a plateau, reflecting the L_{12} behavior of the 2D-like semiconductor [see **Figure 5.2**(e)]. Additionally, we also checked the L_{12} line shape of graphene using the data of S and σ in Ref. [64]. We observe that L_{12} becomes almost constant in the high-conductivity region [see **Figure 5.6**(c)]. These results indicate that the peak structure of L_{12} can only be observed in (6,5) SWCNTs. Therefore, we conclude that the experimentally observed peak structure of L_{12} in (6,5) SWCNT thin films reflects the 1D trace of the (6,5) SWCNT samples.

Although we find such 1D character in the L_{12} of (6,5) SWCNTs, we sometimes find other-dimensional behavior in other samples. **Figure 5.7** indicates L_{12} vs. σ plots in (9,4), (10,3), and Semi SWCNTs. In contrast to the case of (6,5) SWCNTs, we cannot observe clear peak structures in the L_{12} results of (9,4), (10,3), and Semi SWCNTs. In the figures, the position of σ_{b} is determined from P versus σ [see **Figure 5.5**]. In all of the samples, when $\sigma < \sigma_{\mathrm{b}}$, we observe increases in L_{12} as σ increases. However, the (9,4), (10,3), and Semi SWCNTs did not show a clear decrease in L_{12} as σ increases, when $\sigma > \sigma_{\mathrm{b}}$. In these samples, the L_{12} value becomes constant or increases as σ increases, when $\sigma > \sigma_{\mathrm{b}}$. The behavior is relatively similar to the L_{12} behavior in 2D or 3D electronic structures.

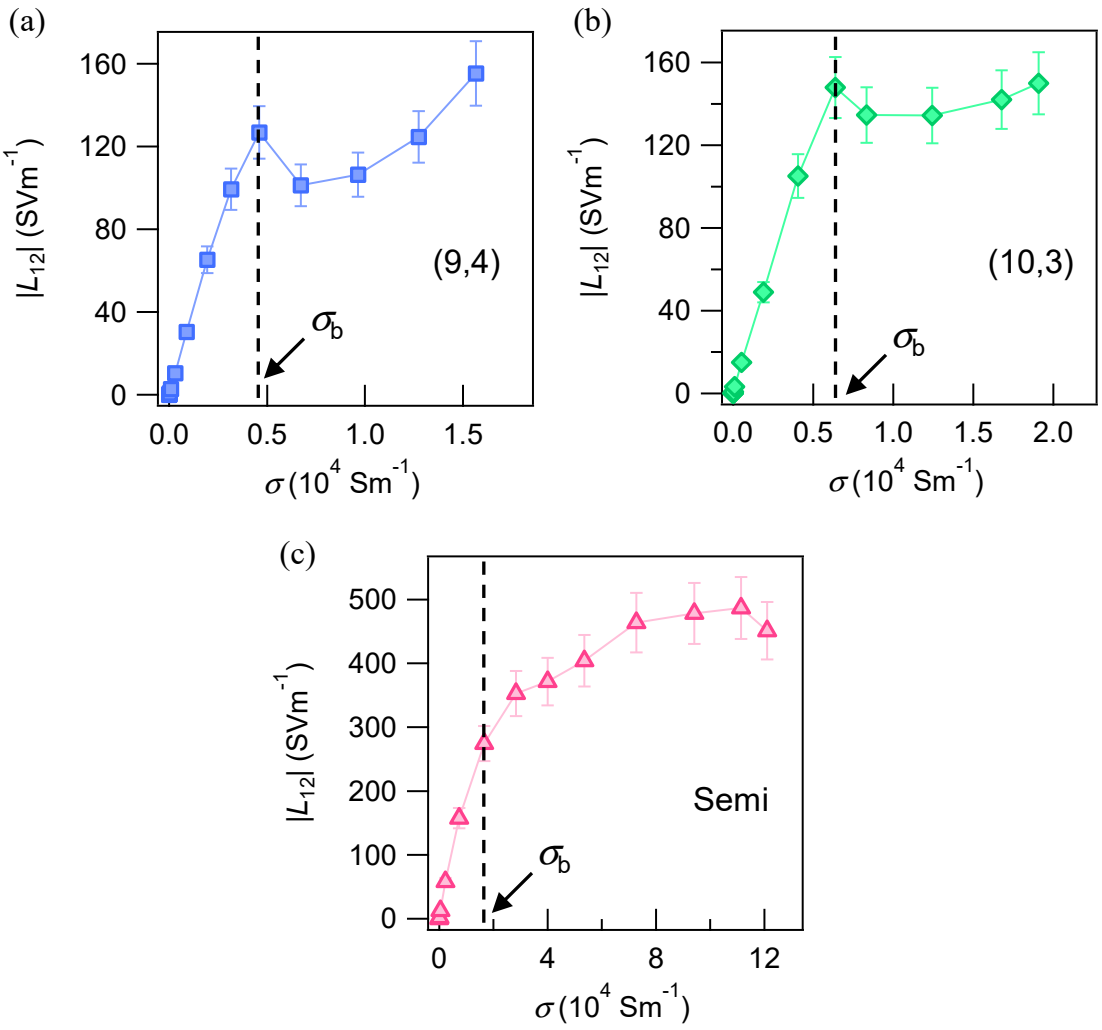

Figure 5.7. Chirality dependence of the thermoelectrical conductivity (L_{12}). Experimental results of $|L_{12}|$ in the *p*-type regions for (a) (9,4), (b) (10,3), and (c) Semi SWCNTs as a function of electrical conductivity (σ). σ at the band edge is described as σ_b, which is obtained by analyzing the relationship between the power factor and σ. The relative error in L_{12} is ~10%, calculated from the Seebeck coefficient measurement errors of the devices. Reprinted figure with permission from Y. Ichinose et al., Phys. Rev. Mater. 5, 025404 (2021). Copyright 2021 by the American Physical Society.

5.5 Discussion

To understand the background of the failure to observe one-dimensionality in chirality other than (6,5), we discuss the following two possible mechanisms: (i) the influence of bundle and network formation in films, and (ii) the influence of metallic SWCNTs as impurities. Regarding the former influence, in thin films of SWCNTs, the SWCNTs form a bundled structure in which individual SWCNTs are tightly packed and form networks. The bundle formation will broaden the peak of the vHs and will blur the 1D characteristics. SWCNTs with larger diameters tend to form bundles more easily than SWCNTs with smaller diameters [163]. Therefore, we assume that the peak structure in the L_{12} of large-diameter semiconducting SWCNTs may be blunted by the broadening of the vHs through the formation of the bundled structures. In addition, the presence of junctions between the bundles will also contribute to the thermoelectric properties, and these junctions will make the transport in SWCNT networks deviate from that of 1D-like transport. These factors will cause 2D- or 3D-like thermoelectric properties in the thin films of (9,4), (10,3), and Semi SWCNTs.

For the latter influence, we describe how the presence of metallic SWCNTs in the sample influences the line shape of L_{12}. There have been many reports that metallic impurities can significantly affect the thermoelectric properties [94,112,120]. **Figure 5.8** compares the line shapes of L_{12} for the 100% (6,5) SWCNTs and mixed samples with metallic SWCNTs (9:1 and 1:1). These L_{12} line shapes are derived from the data of S and σ in Chapter 4. According to the results, the small amount of metallic SWCNTs significantly influences the peak structure of L_{12}. Only a 10% inclusion of metallic SWCNTs in the thin film decreases the value of L_{12} over the entire range, while a 50% inclusion completely eliminates the peak structure. In the present study, the purity of the (6,5) SWCNTs is greater than 99%, whereas the purities of the other semiconducting SWCNTs are not [see **Figure 3.4**]. Therefore, we conclude that the presence of metallic SWCNTs or other chiral SWCNT impurities will influence the decrease in the L_{12} peak structure results of semiconducting SWCNT thin films.

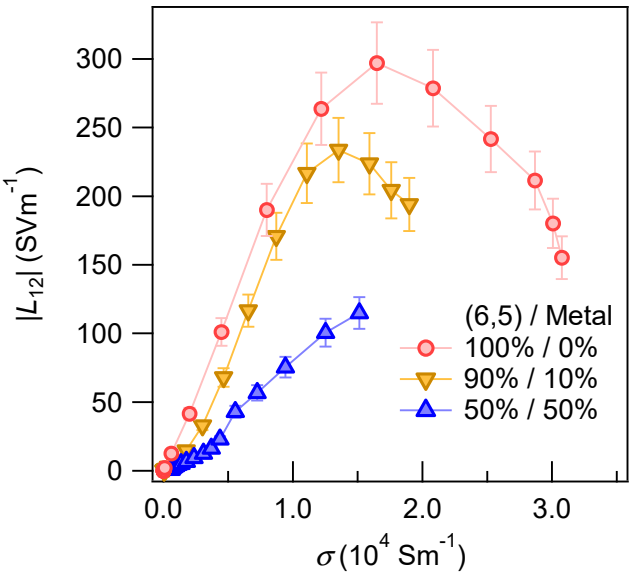

Figure 5.8. Purity dependence of the thermoelectrical conductivity (L_{12}) for (6,5). Experimental results for three types of purity. The (6,5):metal ratios are 100:0 (red circles), 90:10 (yellow reversed triangles) and 50:50 (blue triangles). Reprinted figure with permission from Y. Ichinose et al., Phys. Rev. Mater. 5, 025404 (2021). Copyright 2021 by the American Physical Society.

From the above discussion, we find that L_{12} is an important parameter for discussing the dimensionality of thermoelectric properties, but it should be further noted that L_{12} is also an important parameter for improving the thermoelectric performance. The power factor ($= S^2\sigma$) can be expressed using L_{12} as $P = {L_{12}}^2/T^2\sigma$. According to this equation, to improve the value of P, it is necessary to prepare materials with a large L_{12} and a small σ. A small σ also leads to a small thermal conductivity; thus, finding materials with a large L_{12} at a small σ is a good strategy for improving the thermoelectric performance. In fact, recently the enhancement of thermoelectric generation using the anomalous Nernst effect was reported in iron-based materials [164], and the enhancement was found to be due to the large increase in L_{12}. Therefore, the understanding of L_{12} in materials will help us understand the background of thermoelectric phenomena and to improve the thermoelectric performance.

5.6 Conclusions

In summary, the present study discusses how the dimensionalities of low-dimensional semiconductor electronic structures influence the thermoelectric properties. In the line shape of conventional thermoelectric parameters, such as S and P, it is very difficult to find traces of the dimensionality of the electronic structure. However, the thermoelectrical conductivity, L_{12}, strongly depends on the line shape of the DOS, and we can evaluate the dimensionality of the sample from the L_{12} line shape. We find that L_{12} of the (6,5) SWCNTs exhibits a unique character that reflects the 1D electronic structure: the peak structure of L_{12} reflects the presence of a sharp DOS due to a vHs. Our results indicate the importance of L_{12} for understanding the relationships between the semiconducting electronic structure and thermoelectric properties. In addition, our results imply that the 1D properties of nanomaterials can also be observed at a macroscopic scale, such as in films. This fact can be beneficial for promoting the potential thermoelectric application of 1D materials and encouraging further research.

Chapter 6

Conclusion

6.1 Summary

Developing efficient thermoelectric materials is one of the most important issues for our sustainable society. Dresselhaus et al. theoretically proposed that one-dimensional (1D) materials with nanostructures have the potential to exhibit the highest thermoelectric performance due to unique electronic structure, i.e., van Hove singularity. Experimentally verifying the prediction is essential to promote the development of thermoelectric materials from the viewpoint of condensed matter physics. Thus, many researchers have studied the thermoelectric properties of SWCNTs. However, no reports experimentally have revealed the relationship between the 1D electronic structure of SWCNTs and the thermoelectric properties. Previous studies could not discuss the relationship between 1D electronic structure and thermoelectric properties in detail due to multiple experimental problems.

The purpose of this study is to clarify how the unique thermoelectric properties of 1D electronic structures are embodied and whether the improvement in thermoelectric performance can be observed experimentally.

In order to achieve this goal, we first established an experimental method to solve the experimental problems of precise control of chirality and chemical potential, which have been the main issues in the previous thermoelectric property studies of SWCNTs. The development of the technique to obtain high-purity semiconducting SWCNTs was carried out in Chapter 3. By improving the conventional separation method, we obtained single-chirality semiconducting SWCNTs with more than 99% purity. The chemical potential control was performed using ionic liquids, an electric double layer carrier injection method, and combined with thermoelectric property measurements to establish a unique measurement. Finally, we establish the unique experimental method with the combination of extremely high-purity single-chirality SWCNT samples and thermoelectric

measurement with the precise chemical potential control. This approach allowed us to proceed with the subsequent study on SWCNTs thin-film samples with systematically different electronic structures, namely, metallic and semiconducting 1D electronic structures, in Chapters 4 and 5.

In Chapter 4, we investigated the relationship between 1D electronic structure and thermoelectric properties in metallic SWCNTs. Metallic SWCNTs exhibited behavior in which σ and S increased simultaneously when the chemical potential was positioned in the vicinity of vHs. This phenomenon was an unusual behavior that violated the trade-off problem of conventional thermoelectric materials. Metallic SWCNTs had mainly been disregarded in thermoelectric studies because of their typically small thermoelectric performance under normal circumstances. However, this simultaneous increase of σ and S in metallic SWCNTs led to a large P comparable to the semiconducting SWCNTs. Through the analysis of several simulations and comparison with experimental results, we found that the position of the chemical potential coincided with vHs, which caused these phenomena. Therefore, we concluded that the 1D thermoelectric properties of metallic SWCNTs appear in the relationship between σ and S as the violation of the conventional trade-off relation, resulting in the increase of P.

In Chapter 5, we investigated the relationship between 1D electronic structure and thermoelectric properties in semiconducting SWCNTs. In semiconductors, the information of the dimensionalities in thermoelectric properties cannot be found in typical thermoelectric parameters. However, by focusing on the thermoelectric conductivity term L_{12}, we experimentally found the peak structure at vHs in the experiment on high-purity semiconducting SWCNTs. We compared this phenomenon with the behavior predicted by Boltzmann theory and linear response theory. As a result, we found that the behavior of L_{12} strongly depends on the electronic structure, and the peak structure of L_{12} is unique to one-dimensional electronic structures. Therefore, we concluded that the 1D thermoelectric properties of semiconducting SWCNTs appear in L_{12}. The result indicates that L_{12} is a valuable metric for investigating the fundamental thermoelectric properties of low-dimensional materials.

In summary, the results of this study provided experimental evidence for a previously unknown relationship between 1D electronic structure and thermoelectric properties in metallic and semiconducting SWCNTs. Therefore, we conclude that the purpose of this study, which is to experimentally clarify the relationship between the 1D electronic structure and thermoelectric properties, has been achieved.

6.2 Prospect

The relationship between the 1D electronic structure and thermoelectric properties is thus better understood by the many experimental facts and theoretical supports discussed in this thesis. Therefore, we believe that we can strongly support the guideline and the possibility of improving the thermoelectric performance of CNTs. Recently, we observed a huge power factor (~14 $mWm^{-1}K^{-2}$) exceeding conventional thermoelectric materials such as Bi_2Te_3 in a sample of CNT fibers [165]. To the best of the author's knowledge, this value is the highest among freestanding materials that are stable in air at around room temperature. This dramatic performance improvement is based on the principle elucidated in Chapter 4, i.e., the violation of the trade-off by matching the chemical potential to vHs in the 1D electronic structure. Thus, this is an example of the immediate application of the findings of this study. We hope that the series of research will help solve social problems by increasing the momentum for using CNTs as flexible, safe, and high-performance thermoelectric materials.

On the other hand, there remain issues to be addressed. In this thesis, the samples such as the SWCNT thin film are an aggregate system of many SWCNTs. Thus, the physical model applied in this research would not fully capture the observed phenomena. For example, the SWCNT samples in this study were in the form of millimeter-scale thin films. Because of the assembly of SWCNTs, there are numerous interfaces between individual nanotubes. Electrons must perform hopping conduction with thermal excitation to cross these barriers, i.e., the variable range hopping (VRH) model [79,116]. However, in this study, we have not performed an analysis that explicitly includes the effect of the hopping. At present, there is no obvious solution to why one-dimensionality was clearly visible in the system, such as the VRH model, which is different from the band conduction

model such as the Boltzmann theory. In other words, the mechanism of thermoelectric properties in the systems containing many interfaces remains unresolved. Solving the problem by incorporating the effects of hopping conduction may provide a solution to optimizing the macroscopic shape of SWCNT samples as thermoelectric materials. For example, changing the internal morphology of SWCNT samples, such as the macroscopic orientation and the density of SWCNTs, will alter the picture of hopping conduction and the thermoelectric properties. Once the relationship between the thermoelectric parameters and the hopping conduction is clear, we can fabricate thermoelectric devices with maximum performance.

Furthermore, the elucidation of thermoelectric properties in hopping conduction systems will provide a guideline to improve the performance of not only SWCNTs but also flexible thermoelectric materials in general. For example, organic polymers have been actively studied in thermoelectrics and are expected to be candidates for flexible thermoelectric materials [2,166-169]. Organic polymers are often treated as hopping conduction systems, like SWCNTs, and there is a high possibility that a common mechanism exists in their thermoelectric properties. We hope that the thermoelectric mechanisms of hopping conduction systems in SWCNTs will be elucidated by incorporating some recently developed models in this field [170,171].

Finally, on the basis of the uniqueness of the 1D electronic structure in thermoelectric properties shown in this study, we hope that the research on thermoelectric properties of SWCNTs will make further progress, leading to solving social issues related to energy problems for the next generation and beyond.

Appendix A

Methods of Gel-Chromatography Separation for High-Purity Semiconducting SWCNTs

A.1 Separation procedures for single-chirality (6,5) and (7,5) SWCNTs

We used CoMoCAT SWCNTs as a starting raw material to separate (6,5) and (7,5) SWCNTs. After CoMoCAT was dispersed into water with surfactants, a two-step gel separation was performed, in which the composition of surfactants was changed in each separation step to take advantage of different selectivity.

Dispersion of CoMoCAT sample

1. Prepare an aqueous solution of 1.0 wt% sodium cholate (SC).
2. Add CoMoCAT SWCNTs (SG65, Sigma-Aldrich) at a rate of 1.0 w/v% and disperse the SWCNTs with bath sonication (UT-106H, Sharp) for 10 min.
3. Isolate and disperse the SWCNTs using a chip sonication (Digital Sonifier® 250D advanced, BRANSON) with the power of 30% Amp. for 3 hours.
4. Pour the solution into a special plastic centrifuge tube, set on a swinging rotor (P40ST, Hitachi Koki), and then centrifuged (34,400 rpm, 2 hours) using an ultracentrifuge (Himac CP100WX, Hitachi Koki).
5. After centrifugation, collect the supernatant liquid as a sample, leaving about 1 cm from the bottom of the tube.

Gel chromatography separation (1st step)

Mix an equal amount of 4.0 wt% SDS solution into the 1.0%SC/SWCNT solution in which CoMoCAT is dispersed to make a 2.0%SDS/0.5%SC/SWCNT solution (Solution A). Since the separation is sensitive to temperature, cool the solution to 17°C to obtain stable separation results. Next, prepare a sufficient amount of gel in the column tube with a volume ratio of solution A: gel = 6:7, and feed the solution into the gel [**Figure A.1**(a)]. After the SWCNT solution is fed, collect the effluent (Solution B) while continuing to feed the 2.0%SDS/0.5%SC solution until the color of the effluent disappears.

Check that the lower edge of the gel is whiter than the upper edge. If the bottom of the gel is uniformly black, you should conduct the same procedure above using Solution B, and then you can continue the gel separation (2nd step).

The first step is the separation using the chiral angle selectivity. **Figure A.1**(b) shows the chirality map of SWCNTs. In the condition of 2.0%SDS/0.5%SC, only semiconducting SWCNTs with a small chiral angle (red range) are adsorbed on the gel, while semiconducting with a large chiral angle (blue range) and metallic SWCNTs are not adsorbed on the gel [126]. Taking the specific chirality of SWCNTs abundant in CoMoCAT, as an example, the small chiralities such as (9,1) and (8,3) are adsorbed on the gel. On the other hand, chiralities with large chiral angles such as (6,5) and (7,5) and metallic types are not adsorbed on the gel and are contained in the elution. This elution (solution B) is used in the second step.

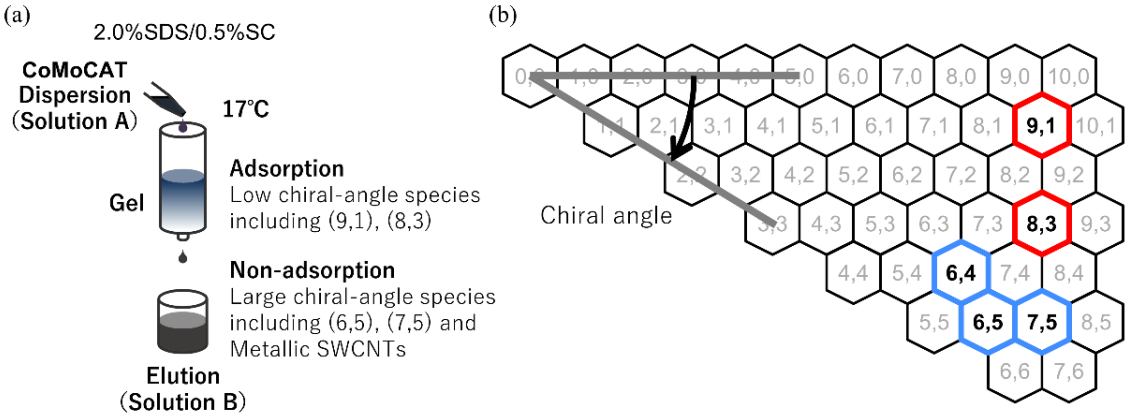

Figure A.1. First step of the separations. (a) Schematic diagram of the gel chromatography. (b) Relationship between chirality map and elution chirality. Semiconducting SWCNTs with small chiral angles (red range) are adsorbed on the gel. The others are not adsorbed and pass the gel.

Gel chromatography separation (2nd step)

The 2.0%SDS/0.5%SC/SWCNT solution (Solution B) collected in the first step is mixed with 0.5%SC solution of three times the volume of Solution B to make 0.5%SDS/0.5%SC/SWCNT solution (Solution C) [**Figure A.2**(a)]. For the second step, prepare the gel in a column tube with a volume ratio of Solution A: gel = 5:2, and feed

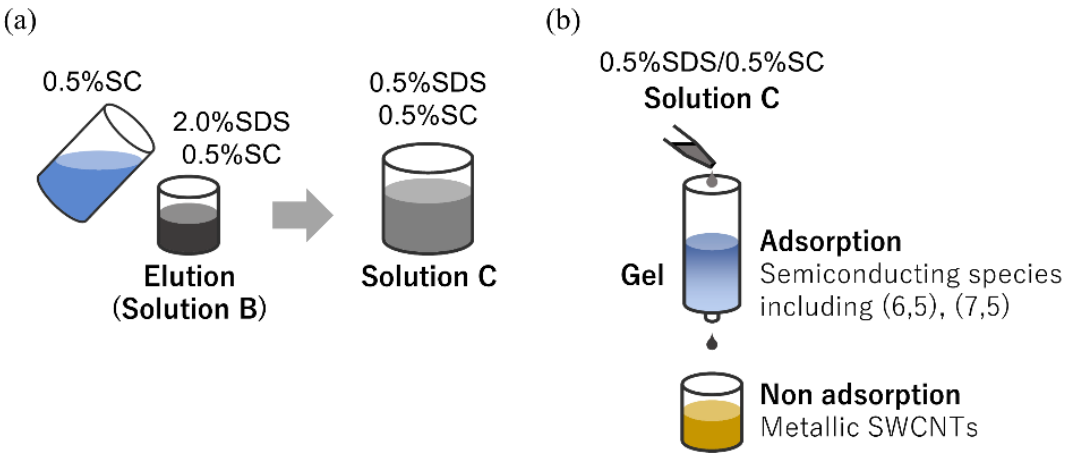

Figure A.2. Adsorption process before the second step of separations. (a) Dilution of solution B. (b) Adsorption process on gel.

the solution into the gel [**Figure A.2**(b)]. At this time, the volume of solution C is quite large, so to shorten the time, the flow rate can be increased by applying pressure with nitrogen from the top of the column tube. After all Solution C is added, 0.5%SDS/0.5%SC solution is continuously added until the color of the eluent disappears (about three times the volume of the gel). The semiconducting types adsorb on the gel, and the metal types pass through the gel under the condition of 0.5%SDS/0.5%SC.

Next, stepwise elution with DOC is performed. 0.5%SDS/0.5%SC/xDOC solution is used, and the x value is prepared in 0.005% increments from 0.020% to 0.060%. First, put 0.5%SDS/0.5%SC/0.020%DOC solution into the gel and collect the elution. In the same way, solutions with larger DOC concentrations are poured in turn, and the elution

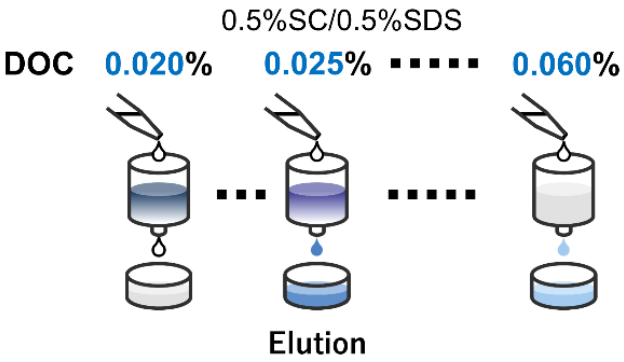

Figure A.3. Second step of separations. The DOC concentration was increased in a stepwise manner with fixed concentrations of 0.5% SC and 0.5% SDS.

is collected [**Figure A.3**].

The second step is a separation using diameter selectivity. As the DOC concentration in the SDS/SC/DOC solution is increased, the chirality with the smallest diameter is sequentially desorbed from the gel. **Figure A.4**(a) shows the optical absorption spectrum of the solution collected by DOC step elution. The DOC concentration increases from the top to the bottom. This result shows that (6,4) is desorbed first, followed by (6,5), (7,5), and (7,6) in that order. **Figure A.4**(b) shows the chirality map. It can be seen that the desorbed SWCNTs change from small diameter chirality to large diameter chirality. 0.035%DOC was collected as the high purity (6,5) sample, and 0.050%DOC was collected as the (7,5) sample.

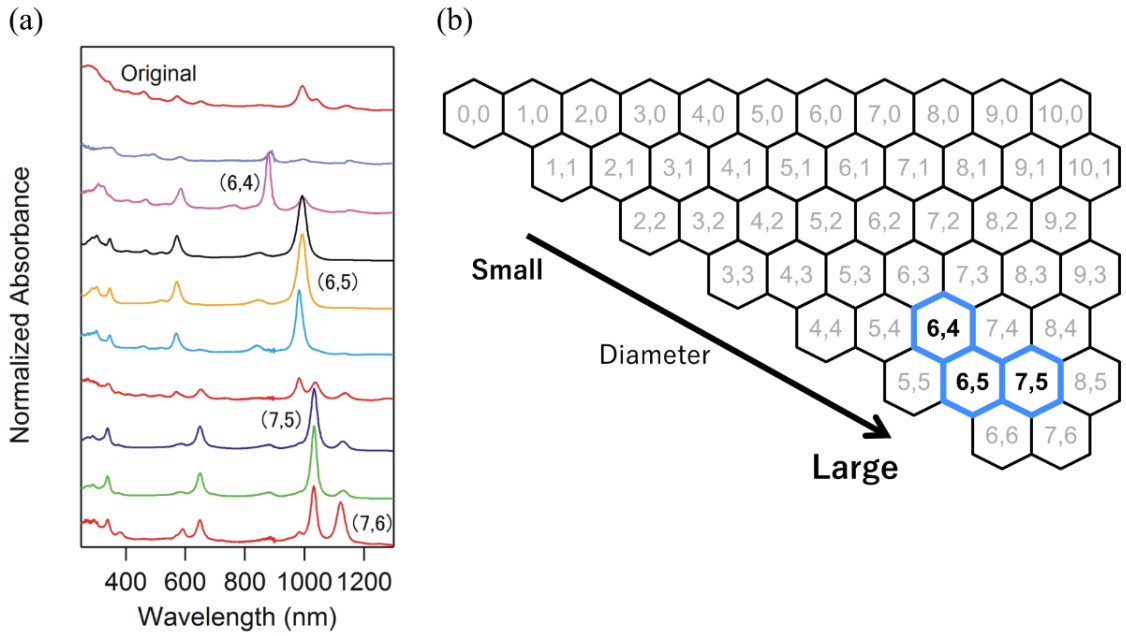

Figure A.4. Separation result of the second step. (a) Absorption spectrum. The top spectrum is Solution B. The DOC concentration is from 0.020% to 0.060% in 0.005% increments. (b) Relationship between chirality map and elution chirality. Reprinted with permission from Y. Ichinose et al., J. Phys. Chem. C 121, 13391 (2017). Copyright 2017 American Chemical Society.

A.2 Separation procedures for single-chirality (9,4) and (10,3) SWCNTs

In order to separate (9,4) and (10,3), HiPco is used as a raw material, and after dispersing HiPco, a one-step gel separation is performed here. The selectivity used for the separation is basically the same as that of CoMoCAT, so the explanation is omitted.

Dispersion of HiPco samples

1. Prepare an aqueous solution of 1.0 wt% sodium cholate (SC).
2. Add HiPco at a rate of 1.0 w/v% and disperse the SWCNTs with bath sonication (UT-106H, Sharp) for 10 minutes.
3. Use a high-speed rotating blade homogenizer (T18BS1, IKA®) for 1 hour to break up the residual solid sample that could not be fully dispersed.
4. Isolate and disperse the SWCNTs using a chip sonication (Digital Sonifier® 250D advanced, BRANSON) with the power of 30% Amp. for 3 hours.
5. Pour the solution into a special plastic centrifuge tube, set on a swinging rotor (P40ST, Hitachi Koki), and then centrifuged (34,400 rpm, 2 hours) using an ultracentrifuge (Himac CP100WX, Hitachi Koki).
6. After centrifugation, collect the supernatant liquid as a sample, leaving about 1 cm from the bottom of the tube.

Gel chromatography separation

Mix an equal amount of 2.0%SDS solution with the 1.0%SC/SWCNT solution in

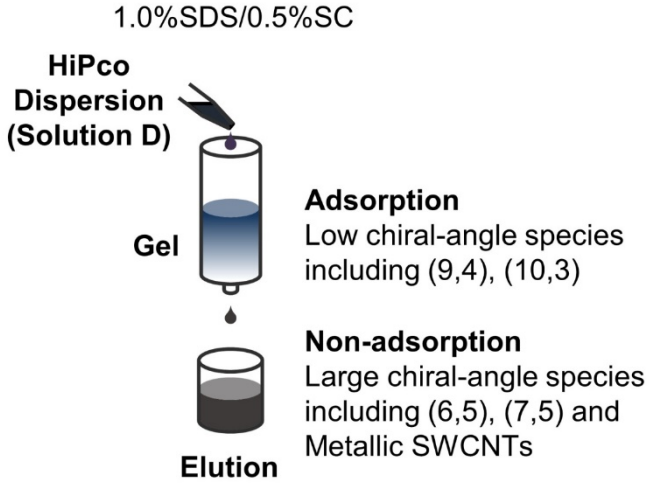

Figure A.5. Adsorption process to separate HiPco SWCNTs.

which HiPco is dispersed to make 1.0%SDS/0.5%SC/SWCNT solution (Solution D). Prepare the gel in the column tube with the volume ratio of solution A: gel = 1:1, and pour the solution into the gel. After all Solution D is fed, continue to feed 1.0%SDS/0.5%SC solution until the color of the eluent disappears (about three times the volume of the gel). In this process, the semiconducting-metal type selectivity and the chiral angle selectivity are utilized. The semiconducting types with large chiral angles and metal types pass through the gel under the condition of 1.0%SDS/0.5%SC [**Figure A.5**].

Next, we perform stepwise elution of the HiPco-adsorbed gel. The poured solution is 1.0%SDS/0.5%SC/xDOC with x values of 0.10%, 0.13%, 0.14%, 0.15%, 0.16%, 0.17% and 0.18%. First, we put 1.0%SDS/0.5%SC/0.10%DOC solution into the gel and collect the eluent. In the same way, the solutions with a large DOC concentration are added in turn, and the eluent are collected (**Figure A.6**(a)). The absorption spectra of the collected eluent are shown in **Figure A.6**(b). In this process, diameter selectivity is used. 0.16% DOC was collected as the high purity (9,4) sample, and 0.18% DOC was collected as the (10,3) sample.

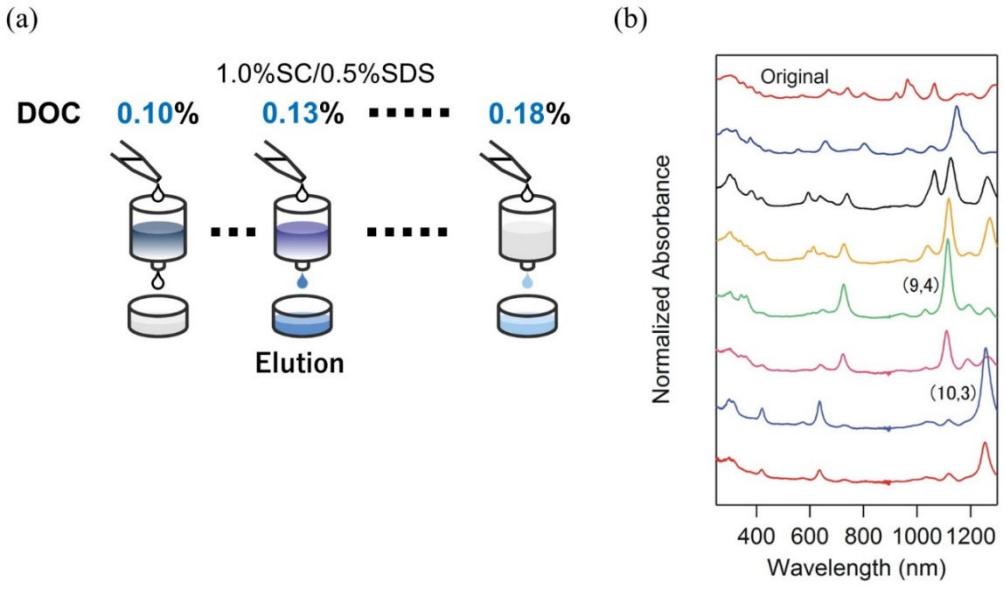

Figure A.6. Separation process for HiPco SWCNTs. (a) Step-wise elution process. The DOC concentration is 0.10%, and from 0.013% to 0.18% in 0.01% increments. (b) Elution of absorption spectra. The top spectrum is Solution D. The second top to the bottom correspond to the DOC concentration of 0.10% to 0.18%. Reprinted with permission from Y. Ichinose et al., J. Phys. Chem. C 121, 13391 (2017). Copyright 2017 American Chemical Society.

Appendix B

Fabrication Method of Thermoelectric Property Measurement Device Using EDLT Structure

After the high purity separation of SWCNTs, the SWCNTs are dispersed in the surfactant solution. From this stage, the process to prepare SWCNTs thin film and to complete the EDLT thermoelectric measurement device will be described in detail.

B.1 Preparation of SWCNT films

Removal of surfactants

In the dispersion of SWCNTs after separation, surfactants are attached to the surface of SWCNTs. Therefore, it is necessary to remove the surfactant before the fabrication of SWCNTs thin film. In this study, we used water and organic solvent for the washing process. The instruments used were a set of funnels for vacuum filtration and a diaphragm pump [see **Figure B.7**].

Figure B.7.
A set of funnels.

(a) Add an equal or greater amount of methanol to the SWCNT dispersion and stir well. The hydrophobic groups of the surfactant are reversed, and the surfactant leaves the SWCNTs, resulting in the SWCNTs becoming bundles.
(b) Filter the solution with vacuum filtration using a membrane filter made of PTFE with a pore size of 0.2 μm (Omnipore, Merck Millipore Ltd.). The bundled SWCNTs are deposited on the filter, and the surfactant-containing aqueous solution and methanol pass through the filter.
(c) Pour an appropriate amount of hot water heated from pure water through the filter where SWCNTs are deposited. The purpose is to desorb as much surfactant as possible from the SWCNTs by the hot water at high temperatures.
(d) Put the filter with SWCNTs in a bottle of methanol and disperse them by bath sonication; after the SWCNTs have left the filter, remove the membrane filter from the

methanol as necessary.

(e) Repeat (b) to (d) about three times, adjusting the number of times according to the volume and concentration of the solution.

(f) Filter the solution with vacuum filtration using the membrane filter with a pore size of 0.2 μm. And then, without pouring hot water, place the filter in a bottle of toluene, and disperse the SWCNTs by bath sonication.

(g) Repeat (f) twice.

(h) After filtration with vacuum filtration through the membrane filter with a pore size of 0.2 μm, methanol is passed through the filter. Finally, put the filter into a bottle filled with methanol and disperse SWCNTs by bath sonication to finish the washing process.

Redispersion of SWCNTs

After the surfactant is removed, the SWCNTs form bundles and aggregate like algae in the solution. Since it is difficult to fabricate a uniform thin film by filtration in this condition, the SWCNTs are re-dispersed with Triton (Triton X-100, Wako Industries, Ltd.), a surfactant that can be easily removed by thermal decomposition even after the fabrication of thin film.

(i) After step (h), perform steps (b) and (c) again.

(j) Put the filter with deposited SWCNTs into a bottle with 1% Triton aqueous solution and disperse SWCNTs by bath sonication; after the SWCNTs have left the filter, remove the membrane filter from the solution as necessary. Since Triton has a weaker dispersing effect than the surfactant used in the separation, the bath sonication should be performed for at least 30 minutes.

Vacuum filtration

A polycarbonate membrane filter (Whatman Nuclepore Track- Etched membrane 25 mm 0.2 μm) is used for thin film preparation. Set the filter in the funnel with the shiny side up and apply ambient pressure. Put the required amount of SWCNT solution into the funnel from the top, remove the bubbles on the surface of the solution using a Pasteur, etc., and then filter under vacuum. After the film is formed, put the film under a vacuum for about one hour to dry out excess water.

B.2 Fabrication of thermoelectric property measurement device

The thermoelectric properties of SWCNT thin film samples are investigated by the ionic liquid-based electric double layer carrier implantation method with precise control of the chemical potential.

(a) Parylene substrate

Parylene (Parylene HT, Nihon Parylene Godo Kaisha, Ltd.) is deposited on a polyimide substrate at a thickness of 10 μm as a thermal insulator (hereafter referred to as "Parylene substrate"), and the substrate is cut into 1.5 cm x 1.5 cm pieces and cleaned in an acetone reflux apparatus.

(b) Gold deposition

Gold electrodes are deposited with a thickness of 100 nm using a vacuum evaporator.

(a) (b)

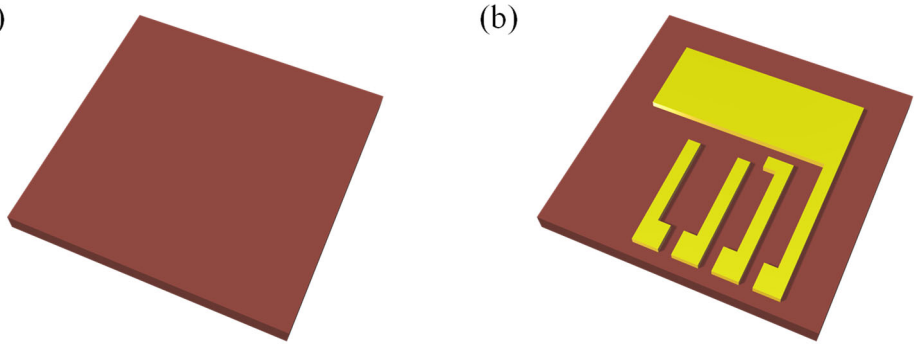

(c) Transfer of the film

The SWCNT thin film was cut into 2 mm x 2 mm pieces and bridged between the source and drain electrodes so that the SWCNT deposited surface was in contact with the substrate. 2-propanol (IPA) was dripped in small amounts and adhered to the substrate, followed by chloroform reflux and acetone reflux to dissolve and rinse the polycarbonate filter.

(d) Vacuum annealing

Vacuum annealing at 200°C for 2 hours is performed to volatilize and remove residual organic solvents and surfactants (Transition) from the thin film.

(e) Attachment of the heater

Attach a heater (strain gauge, KFR-02N-120-C1-16 N10C2, Kyowa Dengyo Co., Ltd.) near one side of the thin film. To avoid uneven temperature rises by the heater, place a copper foil of the same size as the heater between the heater and the substrate,

and attach it with silver paste (DOTITE D-500, Fujikura Kasei Co., Ltd.).

(c)

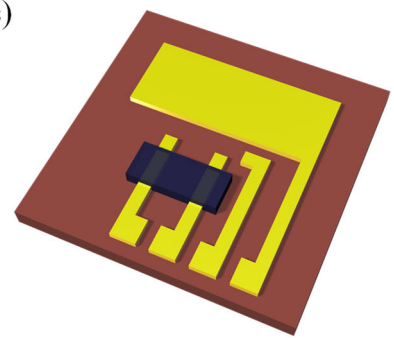

(e)

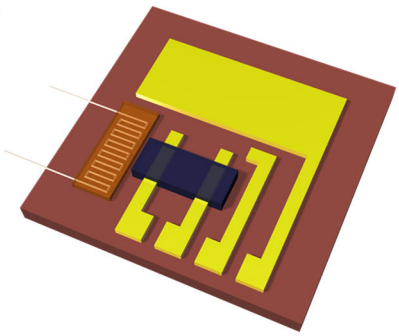

(f) Attaching lead wires

Attach lead wires with silver paste to the source, drain, reference, and gate electrodes. In order to harden the silver paste, leave the device under low-vacuum condition for 1~2 hours or overnight in the atmosphere. To avoid the reaction between the ionic liquid and the silver paste, a sealant (non-corrosive quick-drying adhesive sealant, TSE 397-C, Momentive Performance Materials Japan, LLC) is applied to the silver paste.

(g) Installation of the pool

Make a pool to prevent the ionic liquid from flowing. The pool can be made by piling up sealant, but if it is not high enough, it can be made higher by piling up a second pool on top of the first one.

(f)

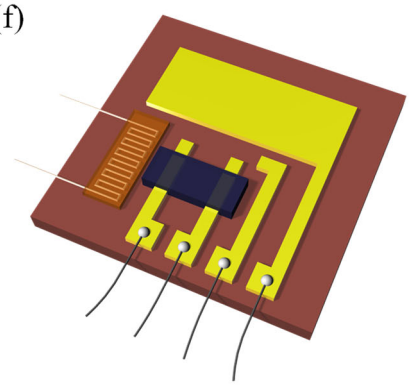

(g)

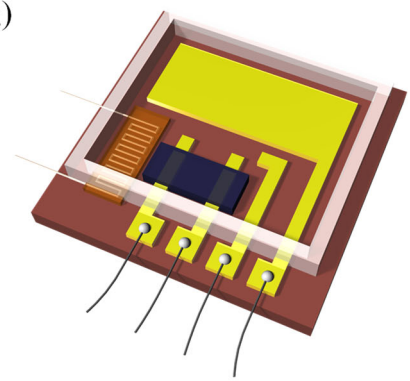

(h) Attachment of thermocouples

Attach the thermocouples to the electrodes on both ends of the thin film using silver paste. When the silver paste hardens, it is applied over the sealant. Leave the film in the air for at least one night until the sealant hardens completely, and then proceed to the next ionic liquid coating.

(i) Coating with ionic liquid

After the silver paste/sealant has completely stiffened, the device is left under vacuum for at least 30 minutes to volatize the water adhering to the surface of the thin film and substrate. The device is then moved into a glove box, carefully avoiding exposure to air, and an ionic liquid (Trimethyl propyl ammonium bis(trifluoromethanesulfonyl)imide, TMPA-TFSI, Kanto Kagaku Co., Ltd.) is dropped into the pool. The ionic liquid is spread over the entire pool by tilting it appropriately. Vacuuming before coating the ionic liquid is important. If the ionic liquid is applied without this process, the water adhering to the thin film will volatilize in the measurement vacuum prober, causing the ionic liquid to boil. This may cause the thin film to break.

(h)

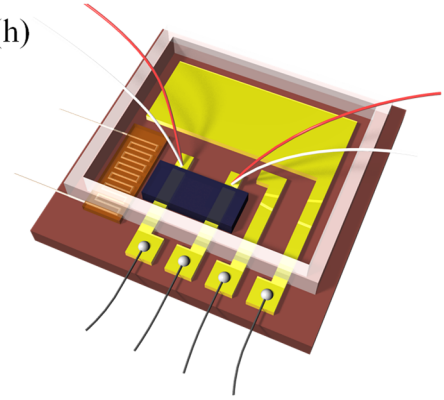

(i)

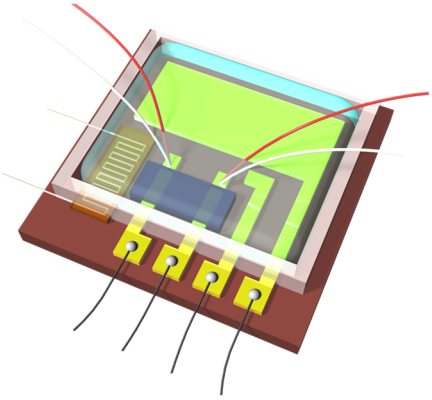

Appendix C

Theoretical Calculation Methods

C.1 Calculations in Chapter 4

Linear response theory combined with the thermal Green's function method within the constant-relaxation-time approximation.

Here we explain the theoretical procedure we used to obtain the relationships between the Seebeck coefficient S and the electrical conductivity σ in semiconducting SWCNTs, which are indicated by dashed curves in **Figure 4.6**. Within Kubo's linear response theory, S as a function of σ can be expressed as

$$S = \frac{1}{T}\frac{L_{12}}{\sigma}$$

Here, σ and L_{12} are given, respectively, by

$$\sigma = \int_{-\infty}^{\infty} dE \left(-\frac{\partial f(E-\mu)}{\partial E}\right) \alpha(E)$$

and

$$L_{12} = -\frac{1}{e}\int_{-\infty}^{\infty} dE \left(-\frac{\partial f(E-\mu)}{\partial E}\right) (E-\mu)\alpha(E),$$

where e (> 0) is the elementary charge, μ is the chemical potential, $f(E-\mu)$ is the Fermi-Dirac distribution function, and $\alpha(E)$ is the spectral conductivity.

The electronic states of the lowest conduction- and highest valence-band edges of a semiconducting SWCNT can be regarded as one-dimensional (1D) Dirac electrons [119]. For 1D Dirac electrons, $\alpha(E)$ can be expressed as

$$\alpha(E) = \frac{\hbar e^2 v^2}{2\pi V}\sum_k \mathrm{Tr}\left[\sigma_x G^A(k,E)\sigma_x G^R(k,E) - \mathrm{Re}\{\sigma_x G^R(k,E)\sigma_x G^R(k,E)\}\right]$$

using the retarded/advanced Green's functions $G^{R/A}(k,E)$, where v is the velocity of a Dirac electron, V is the volume of a system, and σ_x is the x component of Pauli matrix. Within the constant-relaxation-time approximation, the retarded/advanced Green's functions for a 1D Dirac electron are given by

$$G^{R/A}(k,E) = \left\{ \left(E \pm i\frac{\hbar}{2\tau} \right) I - (\hbar v k \sigma_x + \Delta \sigma_z) \right\}^{-1}$$

where τ is the relaxation time of a Dirac electron, I is the 2×2 identity matrix, and σ_z is the z component of Pauli matrix. Once $G^{R/A}(k,E)$ is calculated, we can easily calculate $\alpha(E)$ and eventually can obtain both S and σ.

As mentioned in the main text, the appearance of in-gap state due to the presence of metallic SWCNTs in a semiconducting SWCNT film can be demonstrated by the relaxation time τ [119]. In fact, the in-gap DOS increases with decreasing τ. Thus, the experimental data of S and σ for semiconducting SWCNTs including various amount of metallic SWCNTs can be theoretically fitted by choosing adequate τ.

Tight-binding method for the calculation on thermoelectric properties of single (6,5) and (10,10) SWCNTs.

For theoretical comparison (**Figure 4.8** and **Figure 4.9**) between the power factor of single (6,5) and (10,10) SWCNTs, we performed the following calculation. Within the framework of the Landauer formula, the conductance $G(\mu)$ and Seebeck coefficient $S(\mu)$ with the chemical potential μ are expressed as

$$G(\mu) = \frac{2q^2}{h} \int dE \; T(E) \left(-\frac{\partial f(E,\mu)}{\partial E} \right)$$

and

$$S(\mu) = \frac{1}{qT} \frac{\int dE \; T(E) \left(-\frac{\partial f(E,\mu)}{\partial E} \right) (E-\mu)}{\int dE \; T(E) \left(-\frac{\partial f(E,\mu)}{\partial E} \right)},$$

where q is the charge of carriers, h is the Planck constant, $f(E,\mu)$ is the Fermi–Dirac distribution function and $T(E)$ is the transmission function. As can be seen here, we can obtain $G(\mu)$ and $S(\mu)$, once $T(E)$ is calculated.

We used the tight-binding method to calculate the thermoelectric properties of isolated (6,5) and (10,10) SWCNTs with 1×1×9 Monkhorst-Pack K-grid. The Slater-Koster parameters used in this method were obtained by the density-functional tight-binding method [172] utilizing the “hotbit” code [173]. Under these parameters we performed the calculation of DOS for bulk SWCNTs. In addition, $T(E)$ of SWCNTs was calculated

by combing the nonequilibrium Green's function method with the tight-binding method. SWCNTs were divided into three regions; device region, a left and a right electrode. The length of device region is 5 unit-cells for (6,5) SWCNT and 10 unit-cells for (10,10) SWCNT. The above-mentioned calculation was implemented in the ATK-SE package (Ver. 2019.3) [174].

C.2 Calculations in Chapter 5

Based on the Kubo-Lüttinger formula [175,176], L_{11} and L_{12} of a single-electron system can be expressed as the Sommerfeld-Bethe relations [119-123]:

$$L_{11} = \int_{-\infty}^{\infty} dE \left(-\frac{\partial f(E-\mu)}{\partial E}\right) \alpha(E)\,,$$

$$L_{12} = -\frac{1}{e}\int_{-\infty}^{\infty} dE \left(-\frac{\partial f(E-\mu)}{\partial E}\right) (E-\mu)\alpha(E),$$

where e is the elementary charge, $f(E-\mu)$ is the Fermi-Dirac distribution function, and $\alpha(E)$ is the spectral conductivity. Using L_{11} and L_{12}, S and P are expressed as

$$S = \frac{1}{T}\frac{L_{12}}{L_{11}},$$

$$P = L_{11}S^2 = \frac{1}{T^2}\frac{L_{12}^2}{L_{11}}.$$

An effective Hamiltonian of SWCNTs is known to be expressed as a 1D free Dirac Hamiltonian, which is given by

$$\mathcal{H}_0(k) = \begin{pmatrix} \Delta & \hbar v k \\ \hbar v k & -\Delta \end{pmatrix},$$

where Δ is half of the band gap, v is the velocity of a Dirac electron in the high-energy region of $|E| \gg \Delta$, k is the wave number of a Dirac electron, and $\hbar = h/2\pi$ is the Dirac constant [119]. In the self-consistent Born approximation for short-range random potential, $\alpha(E)$ and $\rho(E)$ can be analytically calculated by

$$\alpha(E) = \frac{1}{A}\frac{e^2}{h}\frac{1}{\mathrm{Im}(\kappa_1\kappa_2)}\mathrm{Re}\left\{\frac{2\kappa_1\kappa_2 + \kappa_1^*\kappa_2 + \kappa_1\kappa_2^*}{\sqrt{\kappa_1\kappa_2}}\right\}$$

with $\mathrm{Im}\sqrt{\kappa_1\kappa_2} > 0$, and

$$\rho(E) = \frac{a}{2\pi\hbar\upsilon}\mathrm{Re}\left\{\frac{\kappa_1+\kappa_2}{\sqrt{\kappa_1\kappa_2}}\right\},$$

where A is the cross-sectional area of the system, a is the unit-cell length,

$$\kappa_1 \equiv \frac{E-\Delta-\sum_{11}^{R}(E)}{\hbar\upsilon},$$

$$\kappa_2 \equiv \frac{E+\Delta-\sum_{22}^{R}(E)}{\hbar\upsilon}.$$

$\sum_{11}^{R}(E)$ and $\sum_{22}^{R}(E)$ are the diagonal elements of the retarded self-energy matrix. This calculation procedure was conducted for the four chirality SWCNTs; (6,5) SWCNTs, (9,4) SWCNTs, (10,3) SWCNTs, and (11,10) SWCNTs, with the relaxation time of 100 fs. **Figure C.8** shows the results of the density of states as a function of energy, L_{11}, L_{12}, S, and P as a function of the chemical potential. The results are used to discussion in Chapter 5.

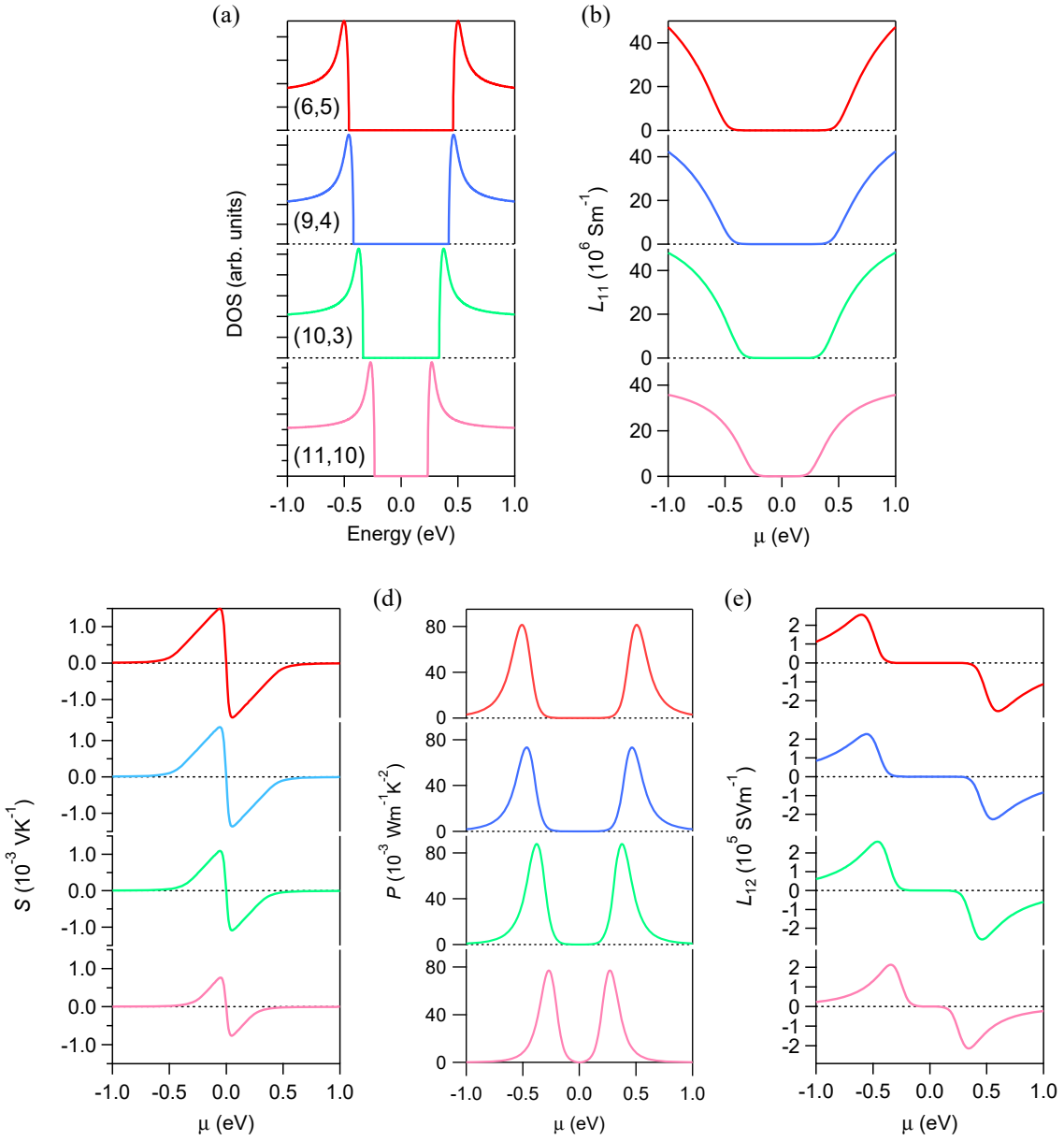

Figure C.8. Calculation results of the thermoelectric properties for (6,5), (9,4), (10,3) and (11,10) using the Kubo-Lüttinger theory. (11,10) is the representative chirality of Semi, which has a diameter of ~1.4 nm. (a) Density of states DOS as a function of energy. (b) electrical conductivity ($L_{11} = \sigma$), (c) Seebeck coefficient (S), (d) power factor (P), and (e) thermoelectrical conductivity (L_{12}) as a function of chemical potential (μ). Reprinted figure with permission from Y. Ichinose et al., Phys. Rev. Mater. 5, 025404 (2021). Copyright 2021 by the American Physical Society.

Appendix D

Supporting information

Additional evaluation of purity of (6,5) SWCNTs

In Chapter 3, the purity of high-purity (6,5) SWCNTs was evaluated to be over 99%. In this section, we will perform additional analysis to confirm that at least 99% is guaranteed. The data in **Figure 3.8** was re-fitted using the same procedure as for the purity evaluation by fitting in Chapter 3. In **Figure D.9**, the dark blue color is the result of the fitting to (6,5) conducted in Chapter 3. We prepared a fitting function for (6,5) that is clearly smaller than the measured data, and it is shown in light blue. The area of (6,5) relative to (9,1), which can be regarded as an impurity, is shown in **Table D.1**. The (6,5) purity was still greater than 99%, although it decreased steadily. Therefore, we conclude that the purity of (6,5) obtained in Chapter 3 of this study is at least 99%.

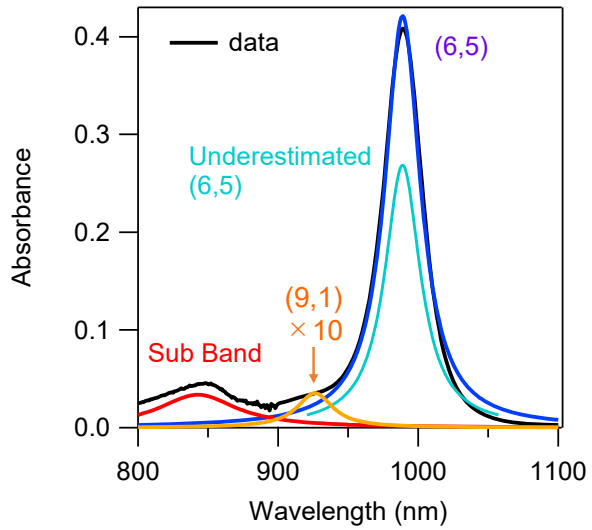

Figure D.9. Additional evaluation of (6,5) SWCNTs. The black line is the measured absorbance spectrum. The underestimated fitting function for (6,5) is plotted as a light blue line.

Table D.1. Comparison of peak area.

Chirality	(6,5)	(9,1)	Total
Area	13.00	0.13	13.13
Ratio (%)	99.01	0.99	100

Shoulder structure of the Seebeck coefficient of high-purity (6,5) SWCNTs

Figure 5.4(b) in Chapter 5 shows the gate voltage dependence of S of semiconducting SWCNTs. Here, there is a small peak (shoulder structure) around $V_{\mathrm{G}} = -2$ V in the data of (6,5). The origin of the shoulder structure is still unknown, but its behavior is different from the theoretically expected S as a function of chemical potential in pure (6,5) SWCNTs. We analyzed whether L_{12} forms a peak structure even in the absence of this shoulder structure. We processed the experimental data of S in the *p*-type region into a straight line for the gate voltage dependence [see **Figure D.10**(a)]. Even when there is no shoulder structure in S, L_{12} decreases in the high-doped region and has a peak structure [see **Figure D.10**(b)]. Therefore, the presence or absence of the shoulder structure of S does not change the discussion and conclusions in Chapter 5 of this study.

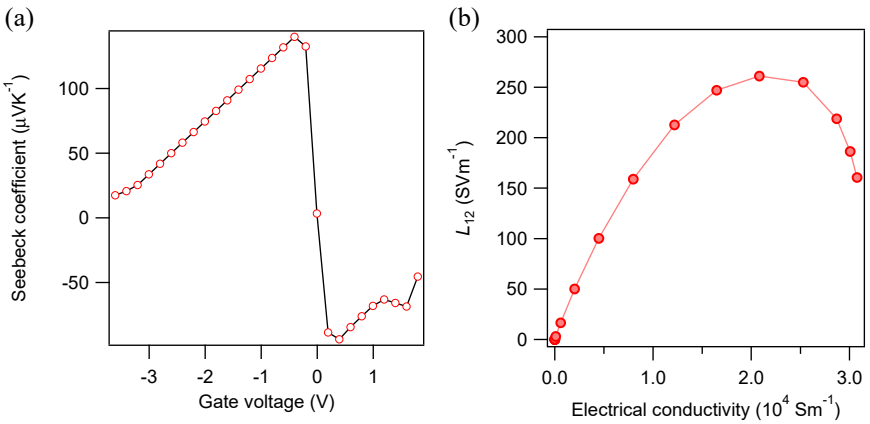

Figure D.10. Analysis of the shoulder structure of the Seebeck coefficient. (a) Seebeck coefficient with data processing; the range from −0.4 V to −3.2 V in the *p*-type region was processed into a straight line. (b) L_{12} calculated by the Seebeck coefficient obtained in (a).

Relationship between chirality of SWCNTs and power factor

In Chapter 5, we measured the thermoelectric properties of several semiconducting SWCNTs. However, the purity of each sample was not uniformed experimentally. Therefore, we compared P obtained by calculation for future research to get a perspective of which chirality shows the largest thermoelectric performance. **Figure D.11** shows P of each chirality calculated by linear response theory in Chapter 5. The details of the calculation method can be found in Appendix C.2. According to the results, all the chirality showed the value of $P \sim 80$ mWm^{-1}K^{-2}, and no significant difference was observed. Therefore, for semiconducting SWCNTs, the chirality in the diameter range of 0.7 nm to 1.4 nm is ideally expected to have a similar thermoelectric performance.

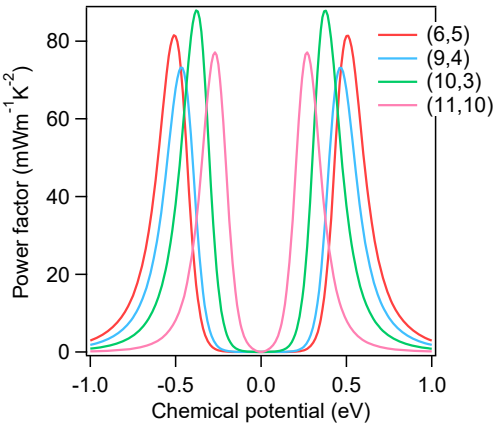

Figure D.11. Power factor calculated by the linear response theory for four semiconducting SWCNTs, namely, (6,5), (9,4), (10,3), and (11,10).

Acknowledgement

I received a great deal of direction and cooperation from many people in writing this dissertation. I would like to acknowledge them as follows.

Prof. Dr. Kazuhiro Yanagi of Tokyo Metropolitan University has been my advisor for six years. He always clearly showed me the policy for writing papers and carrying out research and his attitude and beliefs toward research. The way of thinking I learned from him enabled me always to keep the importance of my research and continue doing my best research. He also willingly gave me opportunities to travel to academic conferences and study abroad. Each time I did so, he gave me the chance to grow. Those six years were precious in my life. I would like to express my heartfelt appreciation to him for his support and guidance over the years.

Assistant Prof. Dr. Yohei Yomogida of Tokyo Metropolitan University guided me in a wide range of areas, including basic knowledge about research and techniques necessary for presentation. In addition, he sometimes stayed with me late into the night to discuss my research and gave me calm and accurate advice. Due to his supervision, I was able to carry out my daily research and write this thesis. I sincerely thank him.

I would like to express my sincere thanks to Assistant Prof. Dr. Kan Ueji of Tokyo Metropolitan University for his technical guidance on my experiments and for writing my papers. Furthermore, our daily discussions in the laboratory have been an important guideline for me to carry out my research.

I would like to thank Prof. Dr. Takahiro Yamamoto and Assistant Prof. Dr. Manaho Matsubara of Tokyo University of Science for their theoretical support throughout this research. Without their cooperation, I could not have quantitatively understood the experimental results and discovered many new findings.

I would like to thank Prof. Dr. Junichiro Kono, Dr. Weilu Gao, Dr. Fumiya Katsutani, and Ms. Natsumi Komatsu of Rice University for supporting my research activities at Rice University and for allowing me to participate in many important collaborative research projects.

I would like to express my sincere gratitude to Associate Prof. Dr. Kazumasa Hattori and Associate Prof. Dr. Yoshikazu Mizuguchi of Tokyo Metropolitan University for reviewing my thesis and giving me many suggestions to improve it.

Thanks to all the seniors, peers, and juniors in my laboratory, I enjoyed and spent a meaningful research life. Mr. Ryotaro Okada, a fellow student, spent three years with me. By advising each other on our experiments of research and presentations, we improved our outcomes. Ms. Akari Yoshida supported me in my experiments many times. I learned a lot from her precise suggestions and her attitude towards research. I want to thank all my colleagues in the laboratory for all their support.

Finally, I sincerely thank my family members for their willingness to support my entry into the doctoral program and their many supports in my research life.

As a Research Fellow, I received support for my research and living expenses from the Japan Society for the Promotion of Science (JSPS), and support for my living expenses from the Nakamura Sekizen-kai. I appreciate it very much.

Reference

[1] C. Forman, I. K. Muritala, R. Pardemann, and B. Meyer, Estimating the global waste heat potential, *Renewable and Sustainable Energy Reviews* **57**, 1568 (2016).

[2] M. Massetti, F. Jiao, A. J. Ferguson, D. Zhao, K. Wijeratne, A. Würger, J. L. Blackburn, X. Crispin, and S. Fabiano, Unconventional Thermoelectric Materials for Energy Harvesting and Sensing Applications, *Chemical Reviews* **121**, 12465 (2021).

[3] T. J. Seebeck, Magnetische Polarisation der Metalle und Erze durch Temperatur-Diffrenz, *Abhandluge der Deuschen Akademic Der Weissenschaften zu Berlin*, 265 (1822).

[4] J.-H. Bahk, H. Fang, K. Yazawa, and A. Shakouri, Flexible thermoelectric materials and device optimization for wearable energy harvesting, *Journal of Materials Chemistry C* **3**, 10362 (2015).

[5] E. W. Zaia, M. P. Gordon, P. Yuan, and J. J. Urban, Progress and Perspective: Soft Thermoelectric Materials for Wearable and Internet-of-Things Applications, *Advanced Electronic Materials* **5**, 1800823 (2019).

[6] Y. Jia, Q. Jiang, H. Sun, P. Liu, D. Hu, Y. Pei, W. Liu, X. Crispin, S. Fabiano, Y. Ma, and Y. Cao, Wearable Thermoelectric Materials and Devices for Self-Powered Electronic Systems, *Advanced Materials* **33**, 2102990 (2021).

[7] K. Kanahashi, J. Pu, and T. Takenobu, 2D Materials for Large-Area Flexible Thermoelectric Devices, *Advanced Energy Materials* **10**, 1902842 (2020).

[8] H. J. Goldsmid and R. W. Douglas, The use of semiconductors in thermoelectric refrigeration, *British Journal of Applied Physics* **5**, 386 (1954).

[9] J. P. Heremans, M. S. Dresselhaus, L. E. Bell, and D. T. Morelli, When thermoelectrics reached the nanoscale, *Nature Nanotechnology* **8**, 471 (2013).

[10] G. J. Snyder and E. S. Toberer, Complex thermoelectric materials, *Nature Materials* **7**, 105 (2008).

[11] B. Abeles, D. S. Beers, G. D. Cody, and J. P. Dismukes, Thermal Conductivity of Ge-Si Alloys at High Temperatures, *Physical Review* **125**, 44 (1962).

[12] J. P. Dismukes, L. Ekstrom, E. F. Steigmeier, I. Kudman, and D. S. Beers, Thermal and Electrical Properties of Heavily Doped Ge-Si Alloys up to 1300°K, *Journal of Applied Physics* **35**, 2899 (1964).

[13] C. B. Vining, W. Laskow, J. O. Hanson, R. R. V. d. Beck, and P. D. Gorsuch, Thermoelectric properties of pressure-sintered Si0.8Ge0.2 thermoelectric alloys, *Journal*

of Applied Physics **69**, 4333 (1991).

[14] D. M. Rowe and G. Min, α-in σ plot as a thermoelectric material performance indicator, *J. Mater. Sci.* **14**, 617 (1995).

[15] G. D. Mahan, in *Solid State Physics*, edited by H. Ehrenreich, and F. Spaepen (Academic Press, 1998), pp. 81.

[16] J. L. Blackburn, A. J. Ferguson, C. Cho, and J. C. Grunlan, Carbon-Nanotube-Based Thermoelectric Materials and Devices, *Advanced Materials* **30**, 1704386 (2018).

[17] G. Homm and P. J. Klar, Thermoelectric materials – Compromising between high efficiency and materials abundance, *physica status solidi (RRL)* **5**, 324 (2011).

[18] L. D. Hicks and M. S. Dresselhaus, Effect of quantum-well structures on the thermoelectric figure of merit, *Physical Review B* **47**, 12727 (1993).

[19] L. D. Hicks and M. S. Dresselhaus, Thermoelectric figure of merit of a one-dimensional conductor, *Physical Review B* **47**, 16631 (1993).

[20] B. Poudel, Q. Hao, Y. Ma, Y. Lan, A. Minnich, B. Yu, X. Yan, D. Wang, A. Muto, D. Vashaee, X. Chen, J. Liu, M. S. Dresselhaus, G. Chen, and Z. Ren, High-Thermoelectric Performance of Nanostructured Bismuth Antimony Telluride Bulk Alloys, *Science* **320**, 634 (2008).

[21] R. Venkatasubramanian, E. Siivola, T. Colpitts, and B. O'Quinn, Thin-film thermoelectric devices with high room-temperature figures of merit, *Nature* **413**, 597 (2001).

[22] W. Xie, X. Tang, Y. Yan, Q. Zhang, and T. M. Tritt, Unique nanostructures and enhanced thermoelectric performance of melt-spun BiSbTe alloys, *Applied Physics Letters* **94**, 102111 (2009).

[23] S. I. Kim, K. H. Lee, H. A. Mun, H. S. Kim, S. W. Hwang, J. W. Roh, D. J. Yang, W. H. Shin, X. S. Li, Y. H. Lee, G. J. Snyder, and S. W. Kim, Dense dislocation arrays embedded in grain boundaries for high-performance bulk thermoelectrics, *Science* **348**, 109 (2015).

[24] T. C. Harman, P. J. Taylor, M. P. Walsh, and B. E. LaForge, Quantum Dot Superlattice Thermoelectric Materials and Devices, *Science* **297**, 2229 (2002).

[25] F. Hsu Kuei, S. Loo, F. Guo, W. Chen, S. Dyck Jeffrey, C. Uher, T. Hogan, E. K. Polychroniadis, and G. Kanatzidis Mercouri, Cubic $AgPb_mSbTe_{2+m}$: Bulk Thermoelectric Materials with High Figure of Merit, *Science* **303**, 818 (2004).

[26] K. Biswas, J. He, I. D. Blum, C.-I. Wu, T. P. Hogan, D. N. Seidman, V. P. Dravid,

and M. G. Kanatzidis, High-performance bulk thermoelectrics with all-scale hierarchical architectures, *Nature* **489**, 414 (2012).

[27] G. Tan, F. Shi, S. Hao, L.-D. Zhao, H. Chi, X. Zhang, C. Uher, C. Wolverton, V. P. Dravid, and M. G. Kanatzidis, Non-equilibrium processing leads to record high thermoelectric figure of merit in PbTe–SrTe, *Nature Communications* **7**, 12167 (2016).

[28] D. Li, Y. Wu, R. Fan, P. Yang, and A. Majumdar, Thermal conductivity of Si/SiGe superlattice nanowires, *Applied Physics Letters* **83**, 3186 (2003).

[29] G. Joshi, H. Lee, Y. Lan, X. Wang, G. Zhu, D. Wang, R. W. Gould, D. C. Cuff, M. Y. Tang, M. S. Dresselhaus, G. Chen, and Z. Ren, Enhanced Thermoelectric Figure-of-Merit in Nanostructured p-type Silicon Germanium Bulk Alloys, *Nano Letters* **8**, 4670 (2008).

[30] S. Bathula, M. Jayasimhadri, N. Singh, A. K. Srivastava, J. Pulikkotil, A. Dhar, and R. C. Budhani, Enhanced thermoelectric figure-of-merit in spark plasma sintered nanostructured n-type SiGe alloys, *Applied Physics Letters* **101**, 213902 (2012).

[31] J.-K. Yu, S. Mitrovic, D. Tham, J. Varghese, and J. R. Heath, Reduction of thermal conductivity in phononic nanomesh structures, *Nature Nanotechnology* **5**, 718 (2010).

[32] L. Yang, D. Huh, R. Ning, V. Rapp, Y. Zeng, Y. Liu, S. Ju, Y. Tao, Y. Jiang, J. Beak, J. Leem, S. Kaur, H. Lee, X. Zheng, and R. S. Prasher, High thermoelectric figure of merit of porous Si nanowires from 300 to 700 K, *Nature Communications* **12**, 3926 (2021).

[33] A. I. Hochbaum, R. Chen, R. D. Delgado, W. Liang, E. C. Garnett, M. Najarian, A. Majumdar, and P. Yang, Enhanced thermoelectric performance of rough silicon nanowires, *Nature* **451**, 163 (2008).

[34] H. J. van Daal, P. B. van Aken, and K. H. J. Buschow, The seebeck coefficient of $YbAl_2$ and $YbAl_3$, *Physics Letters A* **49**, 246 (1974).

[35] J. P. Heremans, V. Jovovic, E. S. Toberer, A. Saramat, K. Kurosaki, A. Charoenphakdee, S. Yamanaka, and G. J. Snyder, Enhancement of Thermoelectric Efficiency in PbTe by Distortion of the Electronic Density of States, *Science* **321**, 554 (2008).

[36] Y. Pei, X. Shi, A. LaLonde, H. Wang, L. Chen, and G. J. Snyder, Convergence of electronic bands for high performance bulk thermoelectrics, *Nature* **473**, 66 (2011).

[37] T. Takabatake, K. Suekuni, T. Nakayama, and E. Kaneshita, Phonon-glass

electron-crystal thermoelectric clathrates: Experiments and theory, *Reviews of Modern Physics* **86**, 669 (2014).

[38] A. Shakouri, Recent Developments in Semiconductor Thermoelectric Physics and Materials, *Annual Review of Materials Research* **41**, 399 (2011).

[39] D. T. Morelli and G. P. Meisner, Low temperature properties of the filled skutterudite CeFe4Sb12, *Journal of Applied Physics* **77**, 3777 (1995).

[40] B. C. Sales, D. Mandrus, B. C. Chakoumakos, V. Keppens, and J. R. Thompson, Filled skutterudite antimonides: Electron crystals and phonon glasses, *Physical Review B* **56**, 15081 (1997).

[41] X. Tang, Q. Zhang, L. Chen, T. Goto, and T. Hirai, Synthesis and thermoelectric properties of p-type- and n-type-filled skutterudite RyMxCo4−xSb12(R:Ce,Ba,Y;M:Fe,Ni), *Journal of Applied Physics* **97**, 093712 (2005).

[42] X. Shi, J. Yang, J. R. Salvador, M. Chi, J. Y. Cho, H. Wang, S. Bai, J. Yang, W. Zhang, and L. Chen, Multiple-Filled Skutterudites: High Thermoelectric Figure of Merit through Separately Optimizing Electrical and Thermal Transports, *Journal of the American Chemical Society* **133**, 7837 (2011).

[43] G. S. Nolas, J. L. Cohn, G. A. Slack, and S. B. Schujman, Semiconducting Ge clathrates: Promising candidates for thermoelectric applications, *Applied Physics Letters* **73**, 178 (1998).

[44] I. Fujita, K. Kishimoto, M. Sato, H. Anno, and T. Koyanagi, Thermoelectric properties of sintered clathrate compounds Sr8GaxGe46−x with various carrier concentrations, *Journal of Applied Physics* **99**, 093707 (2006).

[45] E. S. Toberer, M. Christensen, B. B. Iversen, and G. J. Snyder, High temperature thermoelectric efficiency in $Ba_8Ga_{16}Ge_{30}$, *Physical Review B* **77**, 075203 (2008).

[46] S. R. Culp, S. J. Poon, N. Hickman, T. M. Tritt, and J. Blumm, Effect of substitutions on the thermoelectric figure of merit of half-Heusler phases at 800 °C, *Applied Physics Letters* **88**, 042106 (2006).

[47] H. Xie, H. Wang, Y. Pei, C. Fu, X. Liu, G. J. Snyder, X. Zhao, and T. Zhu, Beneficial Contribution of Alloy Disorder to Electron and Phonon Transport in Half-Heusler Thermoelectric Materials, *Advanced Functional Materials* **23**, 5123 (2013).

[48] H. Xie, H. Wang, C. Fu, Y. Liu, G. J. Snyder, X. Zhao, and T. Zhu, The intrinsic disorder related alloy scattering in ZrNiSn half-Heusler thermoelectric materials, *Scientific Reports* **4**, 6888 (2014).

[49] G. Joshi, X. Yan, H. Wang, W. Liu, G. Chen, and Z. Ren, Enhancement in Thermoelectric Figure-Of-Merit of an N-Type Half-Heusler Compound by the Nanocomposite Approach, *Advanced Energy Materials* **1**, 643 (2011).

[50] J. W. Fergus, Oxide materials for high temperature thermoelectric energy conversion, *Journal of the European Ceramic Society* **32**, 525 (2012).

[51] J. He, Y. Liu, and R. Funahashi, Oxide thermoelectrics: The challenges, progress, and outlook, *Journal of Materials Research* **26**, 1762 (2011).

[52] L.-D. Zhao, S.-H. Lo, Y. Zhang, H. Sun, G. Tan, C. Uher, C. Wolverton, V. P. Dravid, and M. G. Kanatzidis, Ultralow thermal conductivity and high thermoelectric figure of merit in SnSe crystals, *Nature* **508**, 373 (2014).

[53] C. Zhou, Y. K. Lee, Y. Yu, S. Byun, Z.-Z. Luo, H. Lee, B. Ge, Y.-L. Lee, X. Chen, J. Y. Lee, O. Cojocaru-Mirédin, H. Chang, J. Im, S.-P. Cho, M. Wuttig, V. P. Dravid, M. G. Kanatzidis, and I. Chung, Polycrystalline SnSe with a thermoelectric figure of merit greater than the single crystal, *Nature Materials* **20**, 1378 (2021).

[54] J. He and T. M. Tritt, Advances in thermoelectric materials research: Looking back and moving forward, *Science* **357**, eaak9997 (2017).

[55] H. J. Goldsmid and A. W. Penn, Boundary scattering of phonons in solid solutions, *Physics Letters A* **27**, 523 (1968).

[56] D. M. Rowe, V. S. Shukla, and N. Savvides, Phonon scattering at grain boundaries in heavily doped fine-grained silicon–germanium alloys, *Nature* **290**, 765 (1981).

[57] W. Liu, H. S. Kim, Q. Jie, and Z. Ren, Importance of high power factor in thermoelectric materials for power generation application: A perspective, *Scripta Materialia* **111**, 3 (2016).

[58] N. T. Hung, E. H. Hasdeo, A. R. T. Nugraha, M. S. Dresselhaus, and R. Saito, Quantum Effects in the Thermoelectric Power Factor of Low-Dimensional Semiconductors, *Physical Review Letters* **117**, 036602 (2016).

[59] N. T. Hung, A. R. T. Nugraha, and R. Saito, Thermoelectric Properties of Carbon Nanotubes, *Energies* **12**, 4561 (2019).

[60] H. Ohta, S. Kim, Y. Mune, T. Mizoguchi, K. Nomura, S. Ohta, T. Nomura, Y. Nakanishi, Y. Ikuhara, M. Hirano, H. Hosono, and K. Koumoto, Giant thermoelectric Seebeck coefficient of a two-dimensional electron gas in SrTiO3, *Nature Materials* **6**, 129 (2007).

[61] H. Ohta, T. Mizuno, S. Zheng, T. Kato, Y. Ikuhara, K. Abe, H. Kumomi, K. Nomura, and H. Hosono, Unusually Large Enhancement of Thermopower in an Electric Field Induced Two-Dimensional Electron Gas, *Advanced Materials* **24**, 740 (2012).

[62] S. Shimizu, J. Shiogai, N. Takemori, S. Sakai, H. Ikeda, R. Arita, T. Nojima, A. Tsukazaki, and Y. Iwasa, Giant thermoelectric power factor in ultrathin FeSe superconductor, *Nature Communications* **10**, 825 (2019).

[63] J. Duan, X. Wang, X. Lai, G. Li, K. Watanabe, T. Taniguchi, M. Zebarjadi, and E. Y. Andrei, High thermoelectricpower factor in graphene/hBN devices, *Proceedings of the National Academy of Sciences* **113**, 14272 (2016).

[64] K. Kanahashi, M. Ishihara, M. Hasegawa, H. Ohta, and T. Takenobu, Giant power factors in p- and n-type large-area graphene films on a flexible plastic substrate, *npj 2D Materials and Applications* **3**, 44 (2019).

[65] M. S. Dresselhaus, G. Chen, M. Y. Tang, R. G. Yang, H. Lee, D. Z. Wang, Z. F. Ren, J.-P. Fleurial, and P. Gogna, New Directions for Low-Dimensional Thermoelectric Materials, *Advanced Materials* **19**, 1043 (2007).

[66] G. D. Mahan and J. O. Sofo, The best thermoelectric, *Proc. Natl. Acad. Sci.* **93**, 7436 (1996).

[67] Y.-M. Lin, X. Sun, and M. S. Dresselhaus, Theoretical investigation of thermoelectric transport properties of cylindrical Bi nanowires, *Physical Review B* **62**, 4610 (2000).

[68] J. P. Heremans, C. M. Thrush, D. T. Morelli, and M.-C. Wu, Thermoelectric Power of Bismuth Nanocomposites, *Physical Review Letters* **88**, 216801 (2002).

[69] Y. Tian, M. R. Sakr, J. M. Kinder, D. Liang, M. J. MacDonald, R. L. J. Qiu, H.-J. Gao, and X. P. A. Gao, One-Dimensional Quantum Confinement Effect Modulated Thermoelectric Properties in InAs Nanowires, *Nano Letters* **12**, 6492 (2012).

[70] S. Iijima and T. Ichihashi, Single-shell carbon nanotubes of 1-nm diameter, *Nature* **363**, 603 (1993).

[71] R. Saito, M. Fujita, G. Dresselhaus, and M. S. Dresselhaus, Electronic structure of graphene tubules based on C_{60}, *Physical Review B* **46**, 1804 (1992).

[72] T. Ando, Theory of Electronic States and Transport in Carbon Nanotubes, *Journal of the Physical Society of Japan* **74**, 777 (2005).

[73] H. Kataura, Y. Kumazawa, Y. Maniwa, I. Umezu, S. Suzuki, Y. Ohtsuka, and Y. Achiba, Optical properties of single-wall carbon nanotubes, *Synthetic Metals* **103**, 2555

(1999).

[74] R. B. Weisman and S. M. Bachilo, Dependence of Optical Transition Energies on Structure for Single-Walled Carbon Nanotubes in Aqueous Suspension: An Empirical Kataura Plot, *Nano Letters* **3**, 1235 (2003).

[75] J. P. Small, K. M. Perez, and P. Kim, Modulation of thermoelectric power of individual carbon nanotubes, *Physical Review Letters* **91**, 256801 (2003).

[76] M. C. Llaguno, J. E. Fischer, J. A.T. Johnson, and J. Hone, Observation of thermopower oscillations in the coulomb blockade regime in a semiconducting carbon nanotube, *Nano Lett.* **4**, 45 (2004).

[77] C. Yu, L. Shi, Z. Yao, D. Li, and A. Majumdar, Thermal Conductance and Thermopower of an Individual Single-Wall Carbon Nanotube, *Nano Letters* **5**, 1842 (2005).

[78] J. Hone, I. Ellwood, M. Muno, A. Mizel, M. L. Cohen, A. Zettl, A. G. Rinzler, and R. E. Smalley, Thermoelectric Power of Single-Walled Carbon Nanotubes, *Physical Review Letters* **80**, 1042 (1998).

[79] B. Kaiser, Y. W. Park, G. T. Kim, E. S. Choi, G. Düsberg, and S. Roth, Electronic transport in carbon nanotube ropes and mats, *Synthetic Metals* **103**, 2547 (1999).

[80] K. Bradley, S.-H. Jhi, P. G. Collins, J. Hone, M. L. Cohen, S. G. Louie, and A. Zettl, Is the Intrinsic Thermoelectric Power of Carbon Nanotubes Positive?, *Physical Review Letters* **85**, 4361 (2000).

[81] M. Baxendale, K. G. Lim, and G. A. J. Amaratunga, Thermoelectric power of aligned and randomly oriented carbon nanotubes, *Physical Review B* **61**, 12705 (2000).

[82] H. E. Romero, G. U. Sumanasekera, G. D. Mahan, and P. C. Eklund, Thermoelectric power of single-walled carbon nanotube films, *Physical Review B* **65**, 205410 (2002).

[83] M. J. O'Connell, S. M. Bachilo, C. B. Huffman, V. C. Moore, M. S. Strano, E. H. Haroz, K. L. Rialon, P. J. Boul, W. H. Noon, C. Kittrell, J. Ma, R. H. Hauge, R. B. Weisman, and R. E. Smalley, Band Gap Fluorescence from Individual Single-Walled Carbon Nanotubes, *Science* **297**, 593 (2002).

[84] M. Zheng, A. Jagota, E. D. Semke, B. A. Diner, R. S. McLean, S. R. Lustig, R. E. Richardson, and N. G. Tassi, DNA-assisted dispersion and separation of carbon nanotubes, *Nature Materials* **2**, 338 (2003).

[85] R. Krupke, F. Hennrich, H. v. Löhneysen, and M. M. Kappes, Separation of

Metallic from Semiconducting Single-Walled Carbon Nanotubes, *Science* **301**, 344 (2003).

[86] M. S. Arnold, A. A. Green, J. F. Hulvat, S. I. Stupp, and M. C. Hersam, Sorting carbon nanotubes by electronic structure using density differentiation, *Nature Nanotechnology* **1**, 60 (2006).

[87] T. Tanaka, H. Jin, Y. Miyata, S. Fujii, H. Suga, Y. Naitoh, T. Minari, T. Miyadera, K. Tsukagoshi, and H. Kataura, Simple and Scalable Gel-Based Separation of Metallic and Semiconducting Carbon Nanotubes, *Nano Letters* **9**, 1497 (2009).

[88] H. Liu, D. Nishide, T. Tanaka, and H. Kataura, Large-scale single-chirality separation of single-wall carbon nanotubes by simple gel chromatography, *Nature Communications* **2**, 308 (2011).

[89] C. Y. Khripin, J. A. Fagan, and M. Zheng, Spontaneous Partition of Carbon Nanotubes in Polymer-Modified Aqueous Phases, *Journal of the American Chemical Society* **135**, 6822 (2013).

[90] J. L. Blackburn, S. D. Kang, M. J. Roos, B. Norton-Baker, E. M. Miller, and A. J. Ferguson, Intrinsic and Extrinsically Limited Thermoelectric Transport within Semiconducting Single-Walled Carbon Nanotube Networks, *Advanced Electronic Materials* **5**, 1800910 (2019).

[91] M. Statz, S. Schneider, F. J. Berger, L. Lai, W. A. Wood, M. Abdi-Jalebi, S. Leingang, H.-J. Himmel, J. Zaumseil, and H. Sirringhaus, Charge and Thermoelectric Transport in Polymer-Sorted Semiconducting Single-Walled Carbon Nanotube Networks, *ACS Nano* **14**, 15552 (2020).

[92] J. Jiang, J. Wang, and B. Li, A nonequilibrium Green's function study of thermoelectric properties in single-walled carbon nanotubes, *J. Appl. Phys.* **109**, 014326 (2011).

[93] N. T. Hung, A. R. T. Nugraha, E. H. Hasdeo, M. S. Dresselhaus, and R. Saito, Diameter dependence of thermoelectric power of semiconducting carbon nanotubes, *Physical Review B* **92**, 165426 (2015).

[94] A. D. Avery, B. H. Zhou, J. Lee, E. Lee, E. M. Miller, R. Ihly, D. Wesenberg, K. S. Mistry, S. L. Guillot, B. L. Zink, Y. Kim, J. L. Blackburn, and A. J. Ferguson, Tailored semiconducting carbon nanotube networks with enhanced thermoelectric properties, *Nat. Energy* **1**, 16033 (2016).

[95] Y. Nakai, K. Honda, K. Yanagi, H. Kataura, T. Kato, T. Yamamoto, and Y.

Maniwa, Giant Seebeck coefficient in semiconducting single-wall carbon nanotube film, *Appl. Phys. Express* **7**, 025103 (2014).

[96] M. Piao, M.-K. Joo, J. Na, Y.-J. Kim, M. Mouis, G. Ghibaudo, S. Roth, W.-Y. Kim, H.-K. Jang, G. P. Kennedy, U. Dettlaff-Weglikowska, and G.-T. Kim, Effect of Intertube Junctions on the Thermoelectric Power of Monodispersed Single Walled Carbon Nanotube Networks, *The Journal of Physical Chemistry C* **118**, 26454 (2014).

[97] W. Huang, E. Tokunaga, Y. Nakashima, and T. Fujigaya, Thermoelectric properties of sorted semiconducting single-walled carbon nanotube sheets, *Science and Technology of Advanced Materials* **20**, 97 (2019).

[98] K. Yanagi, S. Kanda, Y. Oshima, Y. Kitamura, H. Kawai, T. Yamamoto, T. Takenobu, Y. Nakai, and Y. Maniwa, Tuning of the thermoelectric properties of one-dimensional material networks by electric double layer techniques using ionic liquids, *Nano Letters* **14**, 6437 (2014).

[99] Y. Oshima, Y. Kitamura, Y. Maniwa, and K. Yanagi, Fabrication of thermoelectric devices using precisely Fermi level-tuned semiconducting single-wall carbon nanotubes, *Appl. Phys. Lett.* **107**, 043106 (2015).

[100] S. Shimizu, T. Iizuka, K. Kanahashi, J. Pu, K. Yanagi, T. Takenobu, and Y. Iwasa, Thermoelectric detection of multi-subband density of states in semiconducting and metallic single-walled carbon nanotubes, *Small* **12**, 3388 (2016).

[101] Y. Nonoguchi, K. Ohashi, R. Kanazawa, K. Ashiba, K. Hata, T. Nakagawa, C. Adachi, T. Tanase, and T. Kawai, Systematic conversion of single walled carbon nanotubes into n-type thermoelectric materials by molecular dopants, *Scientific Reports* **3**, 3344 (2013).

[102] T. Fukumaru, T. Fujigaya, and N. Nakashima, Development of *n*-type cobaltocene-encapsulated carbon nanotubes with remarkable thermoelectric property, *Scientific Reports* **5**, 7951 (2015).

[103] A. T. Y. Nonoguchi, C. Goto, T. Kitano, T. Kawai, Thickness-dependent thermoelectric power factor of polymer-functionalized semiconducting carbon nanotube thin films, *J. Sci. Tech. of Adv. Mater.* **19**, 581 (2018).

[104] N. Behabtu, C. C. Young, D. E. Tsentalovich, O. Kleinerman, X. Wang, A. W. K. Ma, E. A. Bengio, R. F. t. Waarbeek, J. J. d. Jong, R. E. Hoogerwerf, S. B. Fairchild, J. B. Ferguson, B. Maruyama, J. Kono, Y. Talmon, Y. Cohen, M. J. Otto, and M. Pasquali, Strong, Light, Multifunctional Fibers of Carbon Nanotubes with Ultrahigh Conductivity,

Science **339**, 182 (2013).

[105] X. He, W. Gao, L. Xie, B. Li, Q. Zhang, S. Lei, J. M. Robinson, E. H. Hároz, S. K. Doorn, W. Wang, R. Vajtai, P. M. Ajayan, W. W. Adams, R. H. Hauge, and J. Kono, Wafer-scale monodomain films of spontaneously aligned single-walled carbon nanotubes, *Nature Nanotechnology* **11**, 633 (2016).

[106] K. Fukuhara, Y. Ichinose, H. Nishidome, Y. Yomogida, F. Katsutani, N. Komatsu, W. Gao, J. Kono, and K. Yanagi, Isotropic Seebeck coefficient of aligned single-wall carbon nanotube films, *Appl. Phys. Lett.* **113**, 243105 (2018).

[107] W. Zhou, Q. Fan, Q. Zhang, K. Li, L. Cai, X. Gu, F. Yang, N. Zhang, Z. Xiao, H. Chen, S. Xiao, Y. Wang, H. Liu, W. Zhou, and S. Xie, Ultrahigh-Power-Factor Carbon Nanotubes and an Ingenious Strategy for Thermoelectric Performance Evaluation, *Small* **12**, 3407 (2016).

[108] J. Choi, Y. Jung, S. J. Yang, J. Y. Oh, J. Oh, K. Jo, J. G. Son, S. E. Moon, C. R. Park, and H. Kim, Flexible and Robust Thermoelectric Generators Based on All-Carbon Nanotube Yarn without Metal Electrodes, *ACS Nano* **11**, 7608 (2017).

[109] C. J. An, Y. H. Kang, H. Song, Y. Jeong, and S. Y. Cho, High-performance flexible thermoelectric generator by control of electronic structure of directly spun carbon nanotube webs with various molecular dopants, *Journal of Materials Chemistry A* **5**, 15631 (2017).

[110] Q. Jin, S. Jiang, Y. Zhao, D. Wang, J. Qiu, D.-M. Tang, J. Tan, D.-M. Sun, P.-X. Hou, X.-Q. Chen, K. Tai, N. Gao, C. Liu, H.-M. Cheng, and X. Jiang, Flexible layer-structured Bi2Te3 thermoelectric on a carbon nanotube scaffold, *Nature Materials* **18**, 62 (2019).

[111] C. Cho, Y. Song, J.-H. Hsu, C. Yu, D. L. Stevens, and J. C. Grunlan, Organic thermoelectric thin films with large p-type and n-type power factor, *Journal of Materials Science* **56**, 4291 (2021).

[112] D. Hayashi, T. Ueda, Y. Nakai, H. Kyakuno, Y. Miyata, T. Yamamoto, T. Saito, K. Hata, and Y. Maniwa, Thermoelectric properties of single-wall carbon nanotube films: Effects of diameter and wet environment, *Appl. Phys. Express* **9**, 025102 (2016).

[113] X. Wei, T. Tanaka, Y. Yomogida, N. Sato, R. Saito, and H. Kataura, Experimental determination of excitonic band structures of single-walled carbon nanotubes using circular dichroism spectra, *Nature Communications* **7**, 12899 (2016).

[114] Y. M. Zuev, W. Chang, and P. Kim, Thermoelectric and Magnetothermoelectric

Transport Measurements of Graphene, *Physical Review Letters* **102**, 096807 (2009).
[115] O. Bubnova, M. Berggren, and X. Crispin, Tuning the Thermoelectric Properties of Conducting Polymers in an Electrochemical Transistor, *Journal of the American Chemical Society* **134**, 16456 (2012).
[116] N. F. Mott and E. A. Davis, *Electronic Processes in Non-Crystalline Materials* (Oxford University Press, Oxford, 1979), Second edn.
[117] D. Hayashi, Y. Nakai, H. Kyakuno, N. Hongo, Y. Miyata, K. Yanagi, and Y. Maniwa, Thermoelectric properties of single-wall carbon nanotube networks, *Japanese Journal of Applied Physics* **58**, 075003 (2019).
[118] J. Pu, K. Kanahashi, N. T. Cuong, C.-H. Chen, L.-J. Li, S. Okada, H. Ohta, and T. Takenobu, Enhanced thermoelectric power in two-dimensional transition metal dichalcogenide monolayers, *Physical Review B* **94**, 014312 (2016).
[119] T. Yamamoto and H. Fukuyama, Bipolar thermoelectric effects in semiconducting carbon nanotubes: description in terms of one-dimensional dirac electrons, *Journal of the Physical Society of Japan* **87**, 114710 (2018).
[120] T. Yamamoto and H. Fukuyama, Possible high thermoelectric power in semiconducting carbon nanotubes ~a case study of doped one-dimensional semiconductors~, *J. Phys. Soc. Jpn.* **87**, 024707 (2018).
[121] M. Jonson and G. D. Mahan, Mott's formula for the thermopower and the Wiedemann-Franz law, *Physical Review B* **21**, 4223 (1980).
[122] H. Kontani, General formula for the thermoelectric transport phenomena based on Fermi liquid theory: Thermoelectric power, Nernst coefficient, and thermal conductivity, *Physical Review B* **67**, 014408 (2003).
[123] M. Ogata and H. Fukuyama, Theory of Spin Seebeck Effects in a Quantum Wire, *Journal of the Physical Society of Japan* **86**, 094703 (2017).
[124] M. Cutler and N. F. Mott, Observation of Anderson localization in an electron gas, *Phys. Rev.* **181**, 1336 (1969).
[125] A. Thess, R. Lee, P. Nikolaev, H. Dai, P. Petit, J. Robert, C. Xu, Y. H. Lee, S. G. Kim, A. G. Rinzler, D. T. Colbert, G. E. Scuseria, D. Tománek, J. E. Fischer, and R. E. Smalley, Crystalline Ropes of Metallic Carbon Nanotubes, *Science* **273**, 483 (1996).
[126] Y. Yomogida, T. Tanaka, M. Zhang, M. Yudasaka, X. Wei, and H. Kataura, Industrial-scale separation of high-purity single-chirality single-wall carbon nanotubes for biological imaging, *Nature Communications* **7**, 12056 (2016).

[127] K. Yanagi, Y. Miyata, and H. Kataura, Optical and Conductive Characteristics of Metallic Single-Wall Carbon Nanotubes with Three Basic Colors; Cyan, Magenta, and Yellow, *Applied Physics Express* **1** (2008).

[128] A. A. Green and M. C. Hersam, Nearly Single-Chirality Single-Walled Carbon Nanotubes Produced via Orthogonal Iterative Density Gradient Ultracentrifugation, *Advanced Materials* **23**, 2185 (2011).

[129] R. M. Jain, R. Howden, K. Tvrdy, S. Shimizu, A. J. Hilmer, T. P. McNicholas, K. K. Gleason, and M. S. Strano, Polymer-Free Near-Infrared Photovoltaics with Single Chirality (6,5) Semiconducting Carbon Nanotube Active Layers, *Advanced Materials* **24**, 4436 (2012).

[130] X. Tu, S. Manohar, A. Jagota, and M. Zheng, DNA sequence motifs for structure-specific recognition and separation of carbon nanotubes, *Nature* **460**, 250 (2009).

[131] G. Ao, C. Y. Khripin, and M. Zheng, DNA-Controlled Partition of Carbon Nanotubes in Polymer Aqueous Two-Phase Systems, *Journal of the American Chemical Society* **136**, 10383 (2014).

[132] G. Ao, J. K. Streit, J. A. Fagan, and M. Zheng, Differentiating Left- and Right-Handed Carbon Nanotubes by DNA, *Journal of the American Chemical Society* **138**, 16677 (2016).

[133] S. Ghosh, S. M. Bachilo, and R. B. Weisman, Advanced sorting of single-walled carbon nanotubes by nonlinear density-gradient ultracentrifugation, *Nature Nanotechnology* **5**, 443 (2010).

[134] P. Zhao, E. Einarsson, G. Lagoudas, J. Shiomi, S. Chiashi, and S. Maruyama, Tunable separation of single-walled carbon nanotubes by dual-surfactant density gradient ultracentrifugation, *Nano Research* **4**, 623 (2011).

[135] M. Kawai, H. Kyakuno, T. Suzuki, T. Igarashi, H. Suzuki, T. Okazaki, H. Kataura, Y. Maniwa, and K. Yanagi, Single Chirality Extraction of Single-Wall Carbon Nanotubes for the Encapsulation of Organic Molecules, *Journal of the American Chemical Society* **134**, 9545 (2012).

[136] J. A. Fagan, C. Y. Khripin, C. A. Silvera Batista, J. R. Simpson, E. H. Hároz, A. R. Hight Walker, and M. Zheng, Isolation of Specific Small-Diameter Single-Wall Carbon Nanotube Species via Aqueous Two-Phase Extraction, *Advanced Materials* **26**, 2800 (2014).

[137] M. Zhang, C. Y. Khripin, J. A. Fagan, P. McPhie, Y. Ito, and M. Zheng, Single-

Step Total Fractionation of Single-Wall Carbon Nanotubes by Countercurrent Chromatography, *Analytical Chemistry* **86**, 3980 (2014).

[138] N. K. Subbaiyan, S. Cambré, A. N. G. Parra-Vasquez, E. H. Hároz, S. K. Doorn, and J. G. Duque, Role of Surfactants and Salt in Aqueous Two-Phase Separation of Carbon Nanotubes toward Simple Chirality Isolation, *ACS Nano* **8**, 1619 (2014).

[139] H. Liu, T. Tanaka, Y. Urabe, and H. Kataura, High-Efficiency Single-Chirality Separation of Carbon Nanotubes Using Temperature-Controlled Gel Chromatography, *Nano Letters* **13**, 1996 (2013).

[140] K. Tvrdy, R. M. Jain, R. Han, A. J. Hilmer, T. P. McNicholas, and M. S. Strano, A Kinetic Model for the Deterministic Prediction of Gel-Based Single-Chirality Single-Walled Carbon Nanotube Separation, *ACS Nano* **7**, 1779 (2013).

[141] A. Hirano, T. Tanaka, Y. Urabe, and H. Kataura, pH- and Solute-Dependent Adsorption of Single-Wall Carbon Nanotubes onto Hydrogels: Mechanistic Insights into the Metal/Semiconductor Separation, *ACS Nano* **7**, 10285 (2013).

[142] A. G. Hsieh, C. Punckt, S. Korkut, and I. A. Aksay, Adsorption of Sodium Dodecyl Sulfate on Functionalized Graphene Measured by Conductometric Titration, *The Journal of Physical Chemistry B* **117**, 7950 (2013).

[143] A. Hirano, T. Kameda, Y. Yomogida, M. Wada, T. Tanaka, and H. Kataura, Origin of the Surfactant-Dependent Redox Chemistry of Single-Wall Carbon Nanotubes, *ChemNanoMat* **2**, 911 (2016).

[144] B. S. Flavel, K. E. Moore, M. Pfohl, M. M. Kappes, and F. Hennrich, Separation of Single-Walled Carbon Nanotubes with a Gel Permeation Chromatography System, *ACS Nano* **8**, 1817 (2014).

[145] H. Gui, J. K. Streit, J. A. Fagan, A. R. Hight Walker, C. Zhou, and M. Zheng, Redox Sorting of Carbon Nanotubes, *Nano Letters* **15**, 1642 (2015).

[146] J. Wang, T. D. Nguyen, Q. Cao, Y. Wang, M. Y. C. Tan, and M. B. Chan-Park, Selective Surface Charge Sign Reversal on Metallic Carbon Nanotubes for Facile Ultrahigh Purity Nanotube Sorting, *ACS Nano* **10**, 3222 (2016).

[147] M. S. Strano, C. B. Huffman, V. C. Moore, M. J. O'Connell, E. H. Haroz, J. Hubbard, M. Miller, K. Rialon, C. Kittrell, S. Ramesh, R. H. Hauge, and R. E. Smalley, Reversible, Band-Gap-Selective Protonation of Single-Walled Carbon Nanotubes in Solution, *The Journal of Physical Chemistry B* **107**, 6979 (2003).

[148] M. Zheng and B. A. Diner, Solution Redox Chemistry of Carbon Nanotubes,

Journal of the American Chemical Society **126**, 15490 (2004).

[149] L.-C. Qin, Electron diffraction from carbon nanotubes, *Reports on Progress in Physics* **69**, 2761 (2006).

[150] H. Liu, T. Tanaka, and H. Kataura, One-step separation of high-purity (6,5) carbon nanotubes by multicolumn gel chromatography, *physica status solidi (b)* **248**, 2524 (2011).

[151] H. Shimotani, S. Tsuda, H. Yuan, Y. Yomogida, R. Moriya, T. Takenobu, K. Yanagi, and Y. Iwasa, Continuous Band-Filling Control and One-Dimensional Transport in Metallic and Semiconducting Carbon Nanotube Tangled Films, *Advanced Functional Materials* **24**, 3305 (2014).

[152] R. A. Smith, *Semiconductors* (Cambridge University Press, Cambrige, 1959).

[153] N. W. Aschcroft and N. D. Mermin, *Solid State Physics* (Saunders College, Philadelphia, 1976).

[154] W. Zhou, Q. Fan, Q. Zhang, L. Cai, K. Li, X. Gu, F. Yang, N. Zhang, Y. Wang, H. Liu, W. Zhou, and S. Xie, High-performance and compact-designed flexible thermoelectric modules enabled by a reticulate carbon nanotube architecture, *Nature Communications* **8**, 14886 (2017).

[155] B. Norton-Baker, R. Ihly, I. E. Gould, A. D. Avery, Z. R. Owczarczyk, A. J. Ferguson, and J. L. Blackburn, Polymer-free carbon nanotube thermoelectrics with improved charge carrier transport and power factor, *ACS Energy Lett.* **1**, 1212 (2016).

[156] Y. Ichinose, J. Eda, Y. Yomogida, Z. Liu, and K. Yanagi, Extraction of high-purity single-chirality single-walled carbon nanotubes through precise pH control using carbon dioxide bubbling, *J. Phys. Chem. C* **121**, 13391 (2017).

[157] X. He, W. Gao, L. Xie, B. Li, Q. Zhang, S. Lei, J. M. Robinson, E. H. Hároz, S. K. Doorn, W. Wang, R. Vajtai, P. M. Ajayan, W. W. Adams, R. H. Hauge, and J. Kono, Wafer-scale monodomain films of spontaneously aligned single-walled carbon nanotubes, *Nat. Nanotechnol.* **11**, 633 (2016).

[158] W. Gao and J. Kono, Science and applications of wafer-scale crystalline carbon nanotube films prepared through controlled vacuum filtration, *R. Soc. Open Sci.* **6**, 181605 (2019).

[159] E. H. Haroz, J. G. Duque, B. Y. Lu, P. Nikolaev, S. Arepalli, R. H. Hauge, S. K. Doorn, and J. Kono, Unique origin of colors of armchair carbon nanotubes, *J. Am. Chem. Soc.* **134**, 4461 (2012).

[160] E. H. Hároz, J. G. Duque, X. Tu, M. Zheng, A. R. Hight Walker, R. H. Hauge, S. K. Doorn, and J. Kono, Fundamental optical processes in armchair carbon nanotubes, *Nanoscale* **5**, 1411 (2013).

[161] Y. Ichinose, A. Yoshida, K. Horiuchi, K. Fukuhara, N. Komatsu, W. Gao, Y. Yomogida, M. Matsubara, T. Yamamoto, J. Kono, and K. Yanagi, Solving the Thermoelectric Trade-Off Problem with Metallic Carbon Nanotubes, *Nano Letters* **19**, 7370 (2019).

[162] M. Ogata and H. Fukuyama, Range of Validity of Sommerfeld–Bethe Relation Associated with Seebeck Coefficient and Phonon Drag Contribution, *Journal of the Physical Society of Japan* **88**, 074703 (2019).

[163] H. Dumlich, M. Gegg, F. Hennrich, and S. Reich, Bundle and chirality influences on properties of carbon nanotubes studied with van der Waals density functional theory, *physica status solidi b* **248**, 2589 (2011).

[164] A. Sakai, S. Minami, T. Koretsune, T. Chen, T. Higo, Y. Wang, T. Nomoto, M. Hirayama, S. Miwa, D. Nishio-Hamane, F. Ishii, R. Arita, and S. Nakatsuji, Iron-based binary ferromagnets for transverse thermoelectric conversion, *Nature* **581**, 53 (2020).

[165] N. Komatsu, Y. Ichinose, O. S. Dewey, L. W. Taylor, M. A. Trafford, Y. Yomogida, G. Wehmeyer, M. Pasquali, K. Yanagi, and J. Kono, Macroscopic weavable fibers of carbon nanotubes with giant thermoelectric power factor, *Nature Communications* **12**, 4931 (2021).

[166] A. B. Kaiser, Thermoelectric power and conductivity of heterogeneous conducting polymers, *Physical Review B* **40**, 2806 (1989).

[167] O. Bubnova and X. Crispin, Towards polymer-based organic thermoelectric generators, *Energy & Environmental Science* **5**, 9345 (2012).

[168] H. Tanaka, K. Kanahashi, N. Takekoshi, H. Mada, H. Ito, Y. Shimoi, H. Ohta, and T. Takenobu, Thermoelectric properties of a semicrystalline polymer doped beyond the insulator-to-metal transition by electrolyte gating, *Science Advances* **6**, eaay8065 (2020).

[169] H. Ito, H. Mada, K. Watanabe, H. Tanaka, and T. Takenobu, Charge transport and thermoelectric conversion in solution-processed semicrystalline polymer films under electrochemical doping, *Communications Physics* **4**, 8 (2021).

[170] S. D. Kang and G. J. Snyder, Charge-transport model for conducting polymers, *Nature Materials* **16**, 252 (2017).

[171] S. A. Gregory, R. Hanus, A. Atassi, J. M. Rinehart, J. P. Wooding, A. K. Menon, M. D. Losego, G. J. Snyder, and S. K. Yee, Quantifying charge carrier localization in chemically doped semiconducting polymers, *Nature Materials* **20**, 1414 (2021).

[172] P. Koskinen and V. Mäkinen, Density-functional tight-binding for beginners, *Comput. Mater. Sci.* **47**, 237 (2009).

[173] https://github.com/pekkosk/hotbit.

[174] K. Stokbro, D. E. Petersen, S. Smidstrup, A. Blom, M. Ipsen, and K. Kaasbjerg, Semiempirical model for nanoscale device simulations, *Physical Review B* **82**, 075420 (2010).

[175] R. Kubo, Statistical-Mechanical Theory of Irreversible Processes. I. General Theory and Simple Applications to Magnetic and Conduction Problems, *Journal of the Physical Society of Japan* **12**, 570 (1957).

[176] J. M. Luttinger, Theory of Thermal Transport Coefficients, *Physical Review* **135**, A1505 (1964).

List of publications and presentations

1 Scientific publications

1.1 Yohei Yomogida, Kanako Horiuchi, Ryotaro Okada, Hideki Kawai, **Yota Ichinose**, Hiroyuki Nishidome, Kan Ueji, Natsumi Komatsu, Weilu Gao, Junichiro Kono, and Kazuhiro Yanagi, "Hall effect in gated single-wall carbon nanotube films," *Scientific Reports* **12**, 101 (2021).

1.2 Natsumi Komatsu, **Yota Ichinose**, Oliver Dewey, Lauren Taylor, Mitchell Trafford, Yohei Yomogida, Geoff Wehmeyer, Matteo Pasquali, Kazuhiro Yanagi, and Junichiro Kono, "Macroscopic Weavable Fibers of Carbon Nanotubes with Giant Thermoelectric Power Factor," *Nature Communications* **12**, 4931 (2021).

1.3 **Yota Ichinose**, Manaho Matsubara, Yohei Yomogida, Akari Yoshida, Kan Ueji, Kaito Kanahashi, Jiang Pu, Taishi Takenobu, Takahiro Yamamoto, and Kazuhiro Yanagi, "One-Dimensionality of the Thermoelectric Properties of Semiconducting Nanomaterials," *Physical Review Materials* **5**(2), 025404 (2021).

1.4 Kan Ueji, Yuya Matsuoka, Takashi Yagi, Yohei Yomogida, **Yota Ichinose**, Akari Yoshida, and Kazuhiro Yanagi, "In situ time-domain thermoreflectance measurements using Au as the transducer during electrolyte gating," *Applied Physics Letters* **117**(13), 133104 (2020).

1.5 Hiroyuki Nishidome, Kohei Nagai, Kento Uchida, **Yota Ichinose**, Yohei Yomogida, Yasumitsu Miyata, Koichiro Tanaka, and Kazuhiro Yanagi, "Control of High-Harmonic Generation by Tuning the Electronic Structure and Carrier Injection," *Nano Letters* **20**(8), 6215–6221 (2020).

1.6 **Yota Ichinose**, Akari Yoshida, Kanako Horiuchi, Kengo Fukuhara, Natsumi Komatsu, Weilu Gao, Yohei Yomogida, Manaho Matsubara, Takahiro Yamamoto, Junichiro Kono, and Kazuhiro Yanagi, "Solving the Thermoelectric Trade-Off Problem with Metallic Carbon Nanotubes," *Nano Letters* **19**(10), 7370-7376 (2019).

1.7 Fumiya Katsutani, Weilu Gao, Xinwei Li, **Yota Ichinose**, Yohei Yomogida,

Kazuhiro Yanagi, and Junichiro Kono, “Direct observation of cross-polarized excitons in aligned single-chirality single-wall carbon nanotubes,” *Physical Review B* **99**(3), 035426 (2019).

1.8 Kengo Fukuhara, **Yota Ichinose**, Hiroyuki Nishidome, Yohei Yomogida, Fumiya Katsutani, Natsumi Komatsu, Weilu Gao, Junichiro Kono, and Kazuhiro Yanagi, “Isotropic Seebeck Coefficient of Aligned Single-wall Carbon Nanotube Films,” *Applied Physics Letters* **113**(24), 243105 (2018).

1.9 Yohei Yomogida, Zheng Liu, **Yota Ichinose**, and Kazuhiro Yanagi, “Sorting Transition-Metal Dichalcogenide Nanotubes by Centrifugation,” *ACS Omega* **3**(8), 8932-8936 (2018).

1.10 Kazuhiro Yanagi, Ryotaro Okada, **Yota Ichinose**, Yohei Yomogida, Fumiya Katsutani, Weilu Gao, and Junichiro Kono. “Intersubband Plasmons in the quantum limit in gated and aligned carbon nanotubes,” *Nature communications* **9**(1), 1121 (2018).

1.11 **Yota Ichinose**, Junko Eda, Yohei Yomogida, Zheng Liu, and Kazuhiro Yanagi, “Extraction of High-Purity Single-Chirality Single-Walled Carbon Nanotubes Through Precise pH Control Using Carbon Dioxide Bubbling,” *Journal of Physical Chemistry C* **121**(24), 13391–13395 (2017).

2 Presentations in international conferences

2.1 **Yota Ichinose**, Akari Yoshida, Manaho Matsubara, Shigeki Saito, Kan Ueji, Yohei Yomogida, Yakahiro Yamamoto, and Kazuhiro Yanagi, “Temperature Dependence of the Thermoelectric Conductivity L_{12} in Semiconducting SWCNTs with Controlled Chemical Potential,” The 61st Fullerenes-Nanotubes-Graphene General Symposium, Online, Poster (2021/09)

2.2 **Yota Ichinose**, Manaho Matsubara, Yohei Yomogida, Akari Yoshida, Kan Ueji, Kaito Kanahashi, Jiang Pu, Taishi Takenobu, Takahiro Yamamoto, and Kazuhiro Yanagi, “One-dimensionality of Thermoelectric Properties of Semiconducting Single-Walled Carbon Nanotubes,” International Conference on the Science and Application of Nanotubes and Low-Dimensional Materials (NT21), Online, Poster

(2021/06)

2.3 **Yota Ichinose**, Rikuto Abe, Kan Ueji, Yohei Yomogida, and Kazuhiro Yanagi, "Thermoelectric properties of morphology-controlled single-walled carbon nanotube alloys," The 60th Fullerenes-Nanotubes-Graphene General Symposium, Online, Poster (2021/03)

2.4 **Yota Ichinose**, Manaho Matsubara, Yohei Yomogida, Akari Yoshida, Kan Ueji, Kaito Kanahashi, Jiang Pu, Taishi Takenobu, Takahiro Yamamoto, and Kazuhiro Yanagi, "Dimensionality of Thermoelectric Properties in Low Dimensional Semiconducting Materials," 33rd International Microprocesses and Nanotechnology Conference (MNC 2020), Online, Oral (2020/11)

2.5 **Yota Ichinose**, Manaho Matsubara, Yohei Yomogida, Akari Yoshida, Kan Ueji, Kaito Kanahashi, Jiang Pu, Taishi Takenobu, Takahiro Yamamoto, and Kazuhiro Yanagi, "One dimensionality of the thermoelectric properties in semiconducting single walled carbon nanotubes," The 59th Fullerenes-Nanotubes-Graphene General Symposium, Online, Poster (2020/09)

2.6 **Yota Ichinose**, Akari Yoshida, Kanako Horiuchi, Kengo Fukuhara, Natsumi Komatsu, Weilu Gao, Yohei Yomogida, Manaho Matsubara, Takahiro Yamamoto, Junichiro Kono, and Kazuhiro Yanagi, "Higher thermoelectric performance in Metallic nanotubes than semiconducting nanotubes," 32nd International Microprocesses and Nanotechnology Conference (MNC 2019), Hiroshima, Oral (2019/10)

2.7 **Yota Ichinose**, Akari Yoshida, Kanako Horiuchi, Kengo Fukuhara, Natsumi Komatsu, Weilu Gao, Yohei Yomogida, Manaho Matsubara, Takahiro Yamamoto, Junichiro Kono, and Kazuhiro Yanagi, "Solving the Thermoelectric Trade-Off Problem with Metallic Carbon Nanotubes," The 57th Fullerenes-Nanotubes-Graphene General Symposium, Nagoya, Poster (2019/09)

2.8 **Yota Ichinose**, Akari Yoshida, Kanako Horiuchi, Kengo Fukuhara, Natsumi Komatsu, Weilu Gao, Yohei Yomogida, Manaho Matsubara, Takahiro Yamamoto, Junichiro Kono, and Kazuhiro Yanagi, "One-Dimensional Thermoelectric Properties of High-Purity Single-Chirality Single-Wall Carbon Nanotube Films," The

20th Nanotube conference (NT19), Würzburg, Germany, Poster (2019/07)

2.9 **Yota Ichinose**, Akari Yoshida, Kengo Fukuhara, Eda Junko, Hitomi Okubo, Yohei Yomogida, and Kazuhiro Yanagi, "Tuning of the Thermoelectric Properties of High-Purity Single-Chirality Single-Walled Carbon Nanotubes by Electrolyte Gating," 31st International Microprocesses and Nanotechnology Conference (MNC 2018), Sapporo, Oral (2018/11)

2.10 **Yota Ichinose**, Akari Yoshida, Kengo Fukuhara, Kanna Ikoma, Eda Junko, Hitomi Okubo, Yohei Yomogida, and Kazuhiro Yanagi, "Influence of Purity on Thermoelectric Properties of Semiconducting SWCNTs Thin Films," Thermal and Charge Transport across Flexible Nano-Interface 2018, Tokyo, Poster (2018/11)

2.11 **Yota Ichinose**, Akari Yoshida, Kengo Fukuhara, Kanna Ikoma, Eda Junko, Hitomi Okubo, Yohei Yomogida, and Kazuhiro Yanagi, "Influence of Purity on Thermoelectric Properties of Semiconducting SWCNTs Thin Films," The 55th Fullerenes-Nanotubes-Graphene General Symposium, Miyagi, Poster (2018/09)

2.12 **Yota Ichinose**, Kengo Fukuhara, Junko Eda, Weilu Gao, Junichiro Kono, Yohei Yomogida, and Kazuhiro Yanagi, "Tuning of the Thermoelectric Properties of High-Purity Single-Chirality (6,5) Single-Walled Carbon Nanotubes by Electrolyte Gating," The 19th Nanotube conference (NT18), Beijing, China, Poster (2018/07)

2.13 **Yota Ichinose**, Kengo Fukuhara, Junko Eda, Yohei Yomogida, and Kazuhiro Yanagi, "Tuning of the Thermoelectric Properties of High-Purity Single-Chirality (6,5) Single-Walled Carbon Nanotubes by Electrolyte Gating," The 54th Fullerenes-Nanotubes-Graphene General Symposium, Tokyo, Poster (2018/03)

2.14 **Yota Ichinose**, Junko Eda, Yutaka Maniwa, Yohei Yomogida, and Kazuhiro Yanagi, "Extraction of High-Purity Single-Chirality Single-Walled Carbon Nanotubes by Precise Tuning of pH using CO2 Bubbling," The 52nd Fullerenes-Nanotubes-Graphene General Symposium, Tokyo, Poster (2017/03)

3 Presentations in domestic meetings [in Japanese]

3.1 **Yota Ichinose**, Manaho Matsubara, Yohei Yomogida, Akari Yoshida, Kan Ueji,

Kaito Kanahashi, Jiang Pu, Taishi Takenobu, Takahiro Yamamoto, and Kazuhiro Yanagi, “One-Dimensionality of the Thermoelectric Properties of Semiconducting Nanomaterials,” JPS 2021 Annual (76th) Meeting, Online, Poster (2021/03)

3.2 **Yota Ichinose**, Akari Yoshida, Kanako Horiuchi, Kengo Fukuhara, Natsumi Komatsu, Weilu Gao, Yohei Yomogida, Manaho Matsubara, Takahiro Yamamoto, Junichiro Kono, and Kazuhiro Yanagi, “One-dimensional thermoelectric properties of single wall carbon nanotubes,” JPS 2020 Annual (75th) Meeting, Aichi, Poster (2020/03)

3.3 **Yota Ichinose**, Akari Yoshida, Kanako Horiuchi, Kengo Fukuhara, Natsumi Komatsu, Weilu Gao, Yohei Yomogida, Manaho Matsubara, Takahiro Yamamoto, Junichiro Kono, and Kazuhiro Yanagi, “High thermoelectric performance in Fermi-level tuned metallic single-wall carbon nanotubes,” The 80th JSAP Autumn Meeting 2019, Hokkaido, Poster (2019/09)

3.4 **Yota Ichinose**, Akari Yoshida, Kengo Fukuhara, Kanna Ikoma, Junko Eda, Hitomi Okubo, Yohei Yomogida, and Kazuhiro Yanagi, “Tuning of Thermoelectric Properties of High-Purity Single-Chirality Single-Walled Carbon Nanotubes by Electrolyte Gating,” The 15th Annual Meeting of the Thermoelectrics Society of Japan, Miyagi, Poster (2018/09)

3.5 **Yota Ichinose**, Akari Yoshida, Kengo Fukuhara, Junko Eda, Hitomi Okubo, Yohei Yomogida, and Kazuhiro Yanagi, “Tuning of Thermoelectric properties of High-Purity Single-Chirality Single-Walled Carbon Nanotubes by Electrolyte Gating,” JPS Autumn Meeting 2018, Kyoto, Oral (2018/09)

3.6 一ノ瀬遥太, 吉田朱里, 生駒栞奈, 福原健吾, 枝淳子, 大久保瞳, 蓬田陽平, 柳和宏, “単一カイラリティ単層カーボンナノチューブ薄膜の熱電特性,” ナノカーボンワークショップ 2018, 東京, ポスター (2018/08)

3.7 **Yota Ichinose**, Kengo Fukuhara, Junko Eda, Yohei Yomogida, and Kazuhiro Yanagi, “Tuning of the Thermoelectric Properties of High-Purity Single-Chirality (6,5) Single-Walled Carbon Nanotubes by Electrolyte Gating,” JPS 2018 Annual (73th) Meeting, Chiba, Oral (2018/03)

3.8 **Yota Ichinose**, Masatoshi Nakamura, Hideki Kawai, Yutaka Maniwa, Yohei

Yomogida, and Kazuhiro Yanagi, “Photo-thermoelectric effect in Metallic and Semiconducting SWCNT thin films with controlled Seebeck coefficients,” JPS Autumn Meeting 2016, Ishikawa, Oral (2016/09)

4 Award

4.1 Student Presentation Award of the Physical Society of Japan, 2021 Annual (76th) meeting of the Physical Society of Japan, March 15, 2021

4.2 Most Impressive Presentation at MNC 2020, 33rd International Microprocesses and Nanotechnology Conference (MNC 2020), March 10, 2021

4.3 Poster Award, The 15th Annual Meeting of the Thermoelectrics Society of Japan, September 14, 2018

4.4 ナノカーボンワークショップ 2018 優秀講演賞（2018）

4.5 Journal of Materials Chemistry A, The 54th Fullerenes-Nanotubes-Graphene General Symposium, April 9, 2018

4.6 Young Scientists Award, The 54th Fullerenes-Nanotubes-Graphene General Symposium, April 9, 2018